

NORTHWESTERN UNIVERSITY

**Nanomechanics and the Viscoelastic Behavior of  
Carbon Nanotube-Reinforced Polymers**

A DISSERTATION

SUBMITTED TO THE GRADUATE SCHOOL  
IN PARTIAL FULFILLMENT OF THE REQUIREMENTS

for the degree

DOCTOR OF PHILOSOPHY

Field of Mechanical Engineering

By

Frank Thomas Fisher

EVANSTON, ILLINOIS

December 2002

□ Copyright by Frank Thomas Fisher 2002

All rights reserved.

# **ABSTRACT**

## **Nanomechanics and the Viscoelastic Behavior of Carbon Nanotube-Reinforced Polymers**

**Frank Thomas Fisher**

Recent experimental results demonstrate that substantial improvements in the mechanical behavior of polymers can be attained using small amounts of carbon nanotubes as a reinforcing phase. While this suggests the potential use of carbon nanotube-reinforced polymers (NRPs) for structural applications, the development of predictive models describing NRP effective behavior will be critical in the development and ultimate employment of such materials. To date many researchers have simply studied the nanoscale behavior of NRPs using techniques developed for traditional composite materials. While such studies can be useful, this dissertation seeks to extend these traditional theories to more accurately model the nanoscale interaction of the NRP constituent phases.

Motivated by micrographs showing that embedded nanotubes often exhibit significant curvature within the polymer, in the first section of this dissertation a hybrid finite element-micromechanical model is developed to incorporate nanotube

waviness into micromechanical predictions of NRP effective modulus. While also suitable for other types of wavy inclusions, results from this model indicate that moderate nanotube waviness can dramatically decrease the effective modulus of these materials.

The second portion of this dissertation investigates the impact of the nanotubes on the overall NRP viscoelastic behavior. Because the nanotubes are on the size scale of the individual polymer chains, nanotubes may alter the viscoelastic response of the NRP in comparison to that of the pure polymer; this behavior is distinctly different from that seen in traditional polymer matrix composites. Dynamic mechanical analysis (DMA) results for each of three modes of viscoelastic behavior (glass transition temperature, relaxation spectrum, and physical aging) are consistent with the hypothesis of a reduced mobility, non-bulk polymer phase in the vicinity of the embedded nanotubes.

These models represent initial efforts to incorporate nanoscale phenomena into predictive models of NRP mechanical behavior. As these results may identify areas where more detailed atomic-scale computational models (such as *ab initio* or molecular dynamics) are warranted, they will be beneficial in the modeling and development of these materials. These models will also aid the interpretation of NRP experimental data.

*For my parents, Frank and Betsy*

*Their constant support and encouragement made this possible.*

*In loving memory of my grandmother, Jane Fisher (1924-2002)*

## ACKNOWLEDGMENTS

This dissertation would not have been possible without the help and support of a great number of people. Perhaps the individual to whom I am most indebted is Cate Brinson, who has been my advisor, mentor and a source of support throughout my years of graduate study. Her patience and willingness as a teacher to develop my understanding and comprehension of the topics of my graduate study is greatly appreciated. Even more important was her encouragement and support as I pursued interests outside of my technical research but that nonetheless have been instrumental in my professional and personal development. Quite simply, had I worked with another advisor I do not think that I would have completed this degree. It has been an honor to work with Professor Brinson, and I will always be grateful for her help.

In addition to Professor Brinson there have been a number of people at Northwestern whose assistance has been valued. The members of my committee, Professors Daniel, Shull (Materials Science) and Ruoff are to be thanked for their contributions to this work; Professor Ruoff in particular was instrumental in providing initial guidance into my work with nanotubes and related materials, and was always willing to share his expertise in the new field of nanomechanics. I would also like to thank Professor Daniel for access to his DMA machine, which was used to perform the experimental testing presented in this dissertation, and Dr. Asma Yasmin for

helpful discussions in this area. I am grateful for the financial support and interaction with researchers at NASA Langley, particularly project monitor Tom Gates. Finally, I would like to thank Brad Files (NASA Johnson Space Center), Rodney Andrews (University of Kentucky), and Linda Schadler and Ami Eitan (RPI) for providing experimental data and samples used in this work.

During my time at Northwestern various members of the Brinson research group (Dr. Roger Bradshaw, Dr. Xiujie Gao, Tao Bai, Dr. Miin-shiou Huang, Wensheng Lin, Sarah Thelan, Debbie Burton, Dr. Ramanathan Thillaiyan, Dr. Nagendra Akshantala, Dr. Alex Bekker, Francois Barthelat, Huanlong Li, and Zhu He) have contributed to this work. The contributions of Dr. Roger Bradshaw, a mentor in my initial years at NU whose return as a post-doc resulted in vast contributions to the wavy nanotube model presented here, are greatly appreciated. Special thanks are reserved for Pat Dyess and Charlotte Gill of the Mechanical Engineering Department.

I am also grateful for the opportunity that I had during my time here at Northwestern to participate in the Learning Sciences program in the School of Education and Social Policy. In particular I appreciate the financial support while in the program of the Graduate School (Dean Richard Morimoto) and the Biomedical Engineering Department at Northwestern (Professor Robert Linsenmeier, chair). I would also like to thank Dr. Andrew Ortony, who was instrumental in making my

participation in the program possible, and Dean Penelope Peterson and Dr. David Kanter for their invaluable assistance with my project work on adaptive expertise.

I'd also like to thank my various roommates and friends at Northwestern who during the years have provided an often needed respite from this work. The rather long list of roommates, who have put up with my newspapers being sprawled over the apartment with little resistance, includes Jay Terry, Caroline Lee, Brad Kinsey, Roger Chen, John Dolbow, and Andrew Savage. I would of course be remiss not to mention the Crafty Veterans, who have given me a chance to showcase my fading athletic skills as we dominated the intramural sports world at NU, the likes of which will undoubtedly never be surpassed. Finally I would like to thank Souyeon Woo for her support and encouragement during my last years at Northwestern.

There are of course many other people who I knew prior to Northwestern who at some time cultivated my dream of a PhD degree, and with whom I have been lucky enough to maintain a cherished friendship: Chris Foust, Dr. Tom Webster, Colleen Kingston, Sophie Hoerr, and Laurie Henderson (from the University of Pittsburgh); and childhood friends Pat Gallagher, Chuck Monastra, Steve Murphy, Shannon Buffler, and Greg Luberecki. To quote Yeats, "Think where man's glory most begins and ends / And say my glory was I had such friends."

I would also like to especially thank my parents Frank and Betsy, and my brothers Mike and Sean, for their unconditional support as I pursued this goal.

# TABLE OF CONTENTS

ABSTRACT .....	iii
ACKNOWLEDGMENTS.....	vi
TABLE OF CONTENTS.....	ix
LIST OF FIGURES .....	xiii
LIST OF TABLES.....	xix
CHAPTER 1: INTRODUCTION.....	1
CHAPTER 2: BACKGROUND.....	8
Structure of Carbon Nanotubes.....	11
Methods of Nanotube Fabrication.....	17
Mechanical Properties of Carbon Nanotubes .....	22
Modulus .....	22
Strength.....	24
Carbon Nanotube-Reinforced Polymers.....	28
Issues related to the fabrication of NRPs.....	28
Nanotube dispersion with the polymer .....	29
Nanotube orientation.....	29
Load transfer across the nanotube-polymer interface.....	31
Mechanical Properties of Carbon Nanotube-Reinforced Polymers .....	35
Elastic behavior .....	35
Viscoelastic behavior.....	41
Other properties .....	46

CHAPTER 3: NANOTUBE WAVINESS AND THE EFFECTIVE MODULUS OF NANOTUBE-REINFORCED POLYMERS .....	50
Introduction.....	50
The Model.....	53
Analytical solution for an isolated wavy nanotube .....	56
Finite element model for the effective reinforcing modulus .....	62
Analytical solution for $E_{\text{cell}}$ .....	65
Convergence of $E_{\text{ERM}}$ for a sufficiently large matrix.....	66
Reduction of $E_{\text{ERM}}$ parameters for the finite element analysis .....	68
Micromechanical Modeling and the Mori-Tanaka Method .....	70
Mori-Tanaka method for unidirectionally-aligned inclusions .....	71
Mori-Tanaka method for randomly aligned inclusions .....	76
Euler angles and tensor transformations.....	78
A note on symmetry.....	83
An alternate model for randomly orientated inclusions.....	86
Simplification for a two-phase system.....	89
Determination of the effective engineering constants .....	90
Discretization of nanotubes based on waviness.....	93
Results .....	97
Effective reinforcing modulus $E_{\text{ERM}}$ .....	98
Analytic expressions for $E_{\text{ERM}}$ for large wavelength ratios .....	104
Micromechanical effective modulus predictions using $E_{\text{ERM}}$ .....	107
An Alternative Model to Incorporate Nanotube Waviness into Effective Moduli Predictions .....	113
Summary.....	118

CHAPTER 4: VISCOELASTIC BEHAVIOR OF CARBON NANOTUBE- REINFORCED POLYMERS.....	123
Introduction to Viscoelasticity.....	128
Molecular theory of polymers and viscoelasticity .....	130
Glass transition temperature .....	132
Physical aging .....	136
Time- and frequency- domain response .....	142
Time-temperature superposition.....	144
Relaxation spectrum .....	147
An interphase region in nanotube-reinforced polymers .....	149
Experimental Procedures.....	155
Glass Transition Temperature for Nanotube-reinforced Polycarbonate .....	160
Frequency- and Time-Domain Response of Nanotube-reinforced Polycarbonate.....	164
Analysis of frequency-domain data.....	165
Experimental time and frequency domain response.....	168
Micromechanical modeling of NRP frequency domain behavior.....	172
Physical Aging of Nanotube-reinforced Polycarbonate.....	179
Summary.....	186
CHAPTER 5: CONCLUSIONS AND FUTURE WORK.....	188
Summary.....	188
Aligned Carbon Nanotube Array Composites.....	192
REFERENCES .....	199
APPENDIX .....	211
Summary of the nanotube-reinforced polymer literature .....	211

Tensor representation using contracted notation .....	215
Components of the Eshelby $S_{ijkl}$ tensor .....	218
Inter-relations between elastic constants .....	223
VITA .....	224

## LIST OF FIGURES

Figure 1. Nanomechanics and other modeling length scales. ....	11
Figure 2. Unit cell and chiral vector for a (4,2) carbon nanotube. ....	13
Figure 3. Examples of nanotubes with different chirality. ....	13
Figure 4. High resolution TEM image of a MWNT .....	16
Figure 5. High resolution TEM image of a SWNT bundle .....	17
Figure 6. SEM image of SWNT bundles formed via the arc discharge method .....	21
Figure 7. SEM images of aligned MWNTs grown via microwave plasma enhanced chemical vapor deposition. ....	21
Figure 8. SEM image of a MWNT loaded in tension between two AFM tips in a nanostressing stage. ....	26
Figure 9. Alignment of nanotubes in PHAE via microtoming .....	31
Figure 10. TEM image showing evidence of PPV wetting the nanotubes. ....	33
Figure 11. TEM images of MWNTs in PHAE. ....	34
Figure 12. TEM observation of crack propagation and nanotube crack bridging in an epoxy-MWNT sample. ....	40
Figure 13. Comparison of experimental data for MWNTs in polystyrene with Rule of Mixtures and Mori-Tanaka predictions. ....	41

Figure 14. Storage modulus and loss tangent results via dynamic mechanical analysis for different epoxy samples. ....	43
Figure 15. Dynamical mechanical analysis of PVOH with different loadings of CVD grown nanotubes.....	45
Figure 16. Electrical conductivity of CVD grown NTs in an epoxy.....	47
Figure 17. Electrical conductivity of PmPV/nanotube composites. ....	48
Figure 18. Micrographs showing the waviness of nanotubes embedded in polymers. ....	51
Figure 19. Schematic of the analytical solution for a free-standing wavy fiber.....	57
Figure 20. Comparison of finite element and analytical solutions for the effective modulus of a free-standing wavy rod. ....	61
Figure 21. Finite element cell model of an embedded wavy nanotube. ....	63
Figure 22. Schematic of Mori-Tanaka method. ....	71
Figure 23. Relationship between the local and global coordinate systems.....	79
Figure 24. Models to account for randomness of inclusion orientation.....	88
Figure 25. Illustrative example of nanotube waviness. ....	96
Figure 26. Model of an NRP using a multiphase composite analysis with a known waviness distribution function. ....	96
Figure 27. $E_{ERM}$ as a function of nanotube waviness ratio ( $a/\lambda$ ) for different ratios of phase moduli with wavelength ratio $\lambda/d=100$ .....	99

Figure 28. $E_{ERM}$ as a function of nanotube wavelength ratio ( $\lambda/d$ ) for different values of nanotube waviness. ....	100
Figure 29. Normalized $E_{ERM}$ (with respect to $E_{NT}$ ) as a function of $E_{ratio}$ for $\lambda/d=100$ . .	102
Figure 30. Effect of Poisson ratio on the $E_{ERM}$ values calculated from the FEM simulations. ....	103
Figure 31. Plot of $\log E_{ERM}$ versus waviness for $\lambda/d=1000$ . ....	105
Figure 32. Plot of $\log E_{ERM}$ versus waviness for $\lambda/d=100$ . ....	107
Figure 33. Experimental data for MWNTs in polystyrene and micromechanical predictions of NRP effective moduli assuming a 3D random orientation of straight and wavy nanotubes. ....	108
Figure 34. Experimental data for MWNTs in polystyrene and micromechanical predictions of NRP effective moduli assuming a 2D random orientation of straight and wavy nanotubes. ....	111
Figure 35. Experimental data for 5 wt% MWNTs in epoxy and micromechanical predictions of NRP effective moduli assuming straight and wavy nanotubes with different NT orientations.....	112
Figure 36. Effective composite modulus $E_{11}$ with increasing waviness ratio ( $a/\lambda$ ) for the ERM and NSCT models. ....	114
Figure 37. Effective composite modulus $E_{22}$ with increasing waviness ratio ( $a/\lambda$ ) for the ERM and NSCT models. ....	115

Figure 38. Effective composite modulus $E_{33}$ with increasing waviness ratio ( $a/l$ ) for the ERM and NSCT models.....	116
Figure 39. Young's modulus predictions for an NRP with 3D randomly oriented wavy NTs using the ERM and the NSCT models.....	117
Figure 40. Storage moduli of PVOH reinforced with MWNTs .....	120
Figure 41. SEM images of silicon nanostructures. ....	121
Figure 42. Three phase model of nanotube-reinforced polymer. ....	126
Figure 43. The glass transition temperature and physical aging. ....	133
Figure 44. Temperature dependence of the modulus of an epoxy sample.....	135
Figure 45. Isothermal physical aging test method of Struik.....	137
Figure 46. Short-term momentary compliance curves for different aging times (pure PC sample, rejuvenated at 165 °C for nominal 15 minutes).....	139
Figure 47. Shifting of momentary compliance curves to form a reference curve (pure PC sample, rejuvenated at 165 °C for nominal 15 minutes).....	140
Figure 48. Shift factors and the shift rate $\mu$ describing physical aging. (Data for pure PC sample, rejuvenated at 165 °C for nominal 15 minutes).....	142
Figure 49. Time-temperature superposition for the creep compliance of an epoxy. ....	147
Figure 50. Equilibrium structure of a (6,6) SWNT/PmPV/LaRC-SI composite system based on molecular dynamics simulations .....	151

Figure 51. Interphase volume fraction ( $V_i$ ) (left) and ratio of the interphase (non-bulk) to matrix (bulk) volume fraction ( $V_m$ ) (right) as a function of fiber volume fraction $V_f$ .....	153
Figure 52. Time-dependent modulus as a function of the mobility parameter $\lambda$ . .....	155
Figure 53. TA Instruments DMA 2980 with film tension clamp. ....	156
Figure 54. Storage moduli as a function of temperature for PC samples. ....	160
Figure 55. Loss moduli as a function of temperature for PC samples. ....	161
Figure 56. Loss tangent as a function of temperature for PC samples. ....	161
Figure 57. Time-temperature shifted frequency-domain experimental data for a pure polycarbonate sample. ....	167
Figure 58. Prony series representation of the frequency domain data. ....	168
Figure 59. Frequency domain storage modulus for PC samples .....	169
Figure 60. Frequency domain loss modulus for PC samples. ....	170
Figure 61. Time domain response for PC samples. ....	170
Figure 62. Relaxation spectra for PC samples. ....	172
Figure 63. Comparison of Mori-Tanaka and finite element solutions for the transverse modulus of a three phase unidirectional composite with viscoelastic interphase and matrix phases. ....	174

Figure 64. Mori-Tanaka prediction for 2% MWNT sample loss modulus, assuming $f_{int}=10\%$ and $\nu=1000$ .....	175
Figure 65. Mori-Tanaka prediction for 2% MWNT sample storage modulus, assuming $f_{int}=10\%$ and $\nu=1000$ .....	176
Figure 66. Mori-Tanaka prediction for 2% MWNT sample loss modulus, assuming $f_{int}=10\%$ and $\nu=100$ .....	177
Figure 67. Mori-Tanaka prediction for 1% MWNT sample loss modulus, assuming $f_{int}=10\%$ and $\nu=1000$ .....	179
Figure 68. Momentary compliance curves for 2% MWNT-PC sample rejuvenated at 165 °C for 15 minutes.....	181
Figure 69. Shifting of momentary compliance curves for 2% MWNT-PC sample rejuvenated at 165 °C for 15 minutes. ....	182
Figure 70. Shift rate $\mu$ for 160 °C rejuvenation for 10 minutes. ....	182
Figure 71. Shift rate $\mu$ for 165 °C rejuvenation for 15 minutes. ....	183
Figure 72. Schematic of the porous anodic alumina (PAA) fabrication method .....	194
Figure 73. Schematic illustration of the geometry of the PAA films. ....	194
Figure 74. Fabrication of ordered carbon nanotube arrays. ....	195
Figure 75. Proposed experiments on the aligned carbon nanotube array composites. ....	197

## LIST OF TABLES

Table 1. Common methods of carbon nanotube production. ....	19
Table 2. Experimental values for the Young's modulus of carbon nanotubes. ....	25
Table 3. Filler materials for structural reinforcement. ....	27
Table 4. Tensile and compressive moduli for 5% MWNTs in epoxy ....	37
Table 5. Tensile strength for PMMA-based NRP with treated and untreated MWNTs...	38
Table 6. Comparison of Huang and Weng models for effective moduli of multiphase composites with randomly orientated inclusions. ....	89
Table 7. Effective reinforcing moduli and hypothetical NT waviness distributions in the micromechanics analysis.....	110
Table 8. Modes of viscoelastic characterization.....	127
Table 9. Comparison of storage moduli and glass transition temperatures for polycarbonate-based samples.....	162
Table 10. Shift rates of blank and NT-reinforced polycarbonate samples.....	183
Table 11. Inter-relations among the elastic constants.....	223

## **CHAPTER 1: INTRODUCTION**

Since their discovery in the early 1990s (Iijima 1991), carbon nanotubes have excited scientists and engineers with their wide range of unusual physical properties. These outstanding physical properties are a direct result of the near-perfect microstructure of the nanotubes (NTs), which at the atomic scale can be thought of as a hexagonal sheet of carbon atoms rolled into a seamless, quasi-one-dimensional cylindrical shape. Besides their extremely small size, it has been suggested that carbon nanotubes are half as dense as aluminum, have tensile strengths twenty times that of high strength steel alloys, have current carrying capacities 1000 times that of copper, and transmit heat twice as well as pure diamond (Collins and Avouris 2000). To take advantage of this unique combination of size and properties, a wide variety of applications have been proposed for carbon nanotubes, including: chemical and genetic probes, field emission tips, mechanical memory, supersensitive sensors, hydrogen and ion storage, scanning probe microscope tips, and structural materials (Collins and Avouris 2000). It has been suggested that nanotechnology, largely fueled by the remarkable properties of carbon nanotubes, may ultimately transform technology to a greater extent than the advances of the silicon revolution (Jamieson 2000).

While the outstanding properties of carbon nanotubes have led to a wide range of hypothesized applications, in this thesis we limit our analysis to the use of carbon nanotubes as a filler phase for structural reinforcement in a host polymer, a material we will refer to as a *nanotube reinforced polymer (NRP)*. A great deal of interest in NRPs for structural applications exists due to a number of potential benefits that are predicted with such materials. A number of these benefits are highlighted below (and discussed in more detail in Chapter 2):

- *High stiffness of carbon nanotubes.* Numerical simulations predict tensile moduli on the order of 1 TPa, making nanotubes perhaps the ultimate high-stiffness filler material. Recent experimental work typically confirms these predictions.
- *High elastic strains of the nanotube.* Numerical simulations predict elastic (recoverable) strains in the nanotube as large as 5%, suggesting an order of magnitude increase in NRP tensile strength compared to traditional composites.
- *Extremely high strength- and stiffness-to-weight ratios.* Given the exceptional strength and stiffness of the NT filler material, it may be possible match

traditional composite properties with much smaller amounts of nanotubes. Alternatively, it may be possible to fabricate high volume fractions NRPs, resulting in strength and stiffness weight ratios unachievable with traditional composite materials. Both scenarios suggest the possibility of substantial weight savings for weight-critical applications.<sup>1</sup>

- *Multifunctionality.* In addition to their outstanding mechanical properties, NTs have also been shown to have exceptional electrical and heat-related properties, suggesting materials that may be designed to meet mechanical as well as secondary material property specifications.
- *Increase in the working/use temperature range.* In some cases large increases in the glass transition temperature of NRPs, in comparison with the blank polymer material, have been reported. Such increases could extend the range of temperatures over which the material will exhibit glassy behavior, increasing the working temperature range of the polymer in structural applications.

---

<sup>1</sup> NASA predicts that SWNT composites will reduce spacecraft weight by 50% or more. (<http://mmptdpublic.jsc.nasa.gov/jscnano/>)

Despite these potential benefits, a number of critical issues must be overcome before the full benefit of such materials can be realized. Such issues include:

- *The high-cost and availability of the raw nanotube material.* As of October 2002, two grams of high quality, low defect, purified SWNTs were available from Carbon Nanotechnologies Incorporated (<http://www.cnanotech.com/>) for \$750/gram. At the same time another supplier, CarboLex (<http://carbolex.com/>), offers as-prepared, unprocessed SWNTs for \$100/gram, and touts that their production output is up to 250 grams per week. These prices are several orders of magnitude higher than the cost of high strength carbon fibers used in composites applications. Methods to develop a continuous, cost-efficient method of producing low-defect carbon nanotubes are under development.
- *Bonding between the nanotube and the polymer.* Proper bonding between the nanotubes and the polymer is critical for sufficient load transfer between the phases. Several examples of excellent load transfer between nanotubes and a polymer have been demonstrated, but more research in this area is needed. Functionalization of the nanotubes is also being investigated by several groups

as a way to increase the chemical reactivity of the nanotubes and thus improve the bonding between the NTs and the polymer.

- *Dispersion of the nanotubes within the polymer.* Due to van der Waals attractive forces nanotubes are notoriously difficult to disperse in a polymer. Proper dispersion will be necessary for optimal, and more importantly uniform, material properties.
- *Orientation and geometry of the nanotubes within the polymer.* To tailor the properties of NRPs it is desirable to be able to control the orientation of the nanotubes within the polymer. While methods have been developed to orient free-standing and as-grown NTs, methods to orient nanotubes in bulk polymers have yet to be developed. In addition, electron microscopy images of nanotube-reinforced polymers also show that the NTs typically remain curved (wavy) when embedded within a polymer. The impact of this waviness on the effective modulus of the NRP is modeled in Chapter 3 of this work.
- *Differences between nanotubes forms.* The properties of nanotubes are known to be dependent on the method of production and the form of the nanotube (single-walled nanotube, multi-walled nanotube, or nanotube bundle). The

relationship between these variables and mechanical properties needs to be further elucidated.

- *Accurate models of NRP behavior.* Accurate models of NRP behavior are necessary to aid in the interpretation of experimental results and, in the long term, to allow aggressive design strategies that fully leverage the benefits of such materials. In particular, the viscoelastic behavior of nanotube-reinforced polymers is often substantially different than that of the pure (blank) polymer; this behavior is modeled in terms of a reduced mobility non-bulk interphase region (in the vicinity of the nanotubes) in Chapter 4 of this dissertation.

Over the last several decades research in the area of composite materials, and in particular polymer matrix composites, has become quite mature. However, in many cases it will be necessary to extend these theories, which have been developed for macroscale composites, to account for phenomena that are particular to the use of nanoscale reinforcement. The work presented in this thesis represents two examples of such model extensions:

- The incorporation of nanotube waviness, which is typically observed in high magnification electron microscopy images of nanotube-reinforced polymers, into micromechanical predictions of the elastic stiffness of these materials.
- The impact of the nanotubes on the mobility of the polymer chains and the resulting effective viscoelastic behavior of the NRP.

This dissertation has been organized in the following format. To firmly ground the reader in the current state of the art, an in-depth discussion of the theoretical and experimental properties of nanotubes and nanotube-reinforced polymers is provided in Chapter 2. In Chapter 3 a hybrid finite element – micromechanical model developed to incorporate the waviness of the embedded nanotubes into micromechanics prediction of effective elastic moduli of NRPs is presented. In Chapter 4 the impact of the nanotubes on the overall viscoelastic behavior of the NRP is discussed. While Chapters 3 and 4 are both related to the effective mechanical properties of nanotube-reinforced polymers, each chapter has been written as a self-contained unit and may be read independent of the other. Chapter 5 summarizes this work and highlights future directions of research that will facilitate the development of accurate models of nanotube-reinforced polymer behavior.

## **CHAPTER 2: BACKGROUND**

The extremely small size and outstanding physical properties of carbon nanotubes have interested researchers in a wide variety of fields, including chemistry, physics, materials science, and engineering. This interest is from both the standpoint of fundamental research into material behavior, as well as the use of carbon nanotubes in a variety of applications (as discussed in Chapter 1), where the characteristics of the nanotubes can be exploited to gain a design advantage. With the explosion of research in the area of nanotechnology, the potential application of nanotubes (and other nanostructures) is quite large, and several excellent books broadly discuss the early work in this field (Drexler 1992; Dresselhaus, Dresselhaus et al. 1996; Harris 1999).

In this dissertation we will primarily focus on the use of carbon nanotubes as the reinforcing phase in a bulk polymer material, with a focus on the effective mechanical response of the material to low levels of stress. While this narrow focus will neglect a wide variety of interesting topics, such as the electrical, thermal, and fracture behavior of nanotube-reinforced polymers, we believe that the results presented in this dissertation will provide a strong foundation for future characterization and development of NRP systems.

From the standpoint of modeling, nanotubes and their use in polymers are challenging because of the range of length scales that must be modeled for such materials. Modeling at atomistic scales using the principles of quantum mechanics and molecular dynamics has been developed to model clusters of atoms, but are computationally prohibitive and to date have been limited to looking at the behavior of individual nanotubes. For larger length scales, the fields of micromechanics and continuum mechanics are well established but not well-suited to model details at the atomistic level that are likely to be important for nanostructured materials. The area of nanomechanics is proposed as a means to bridge these length scales in order to develop accurate models of nanotubes and related materials. The development of nanomechanics into a well-grounded area of study will require contributions from these other length scales as shown in Figure 1. Additional information provided by experimental techniques, at both the micro- and nano-scale, will further the development of these models.

The work described in this dissertation is an initial thrust in this direction; these efforts can be characterized as extending traditional micromechanics and viscoelastic models for the study of nanotube-reinforced polymers. This work is motivated by theoretical predictions and preliminary experimental results that suggest that small amounts of carbon nanotubes can significantly enhance the overall mechanical behavior of the polymer (Schadler, Giannaris et al. 1998; Shaffer and

Windle 1999; Gong, Liu et al. 2000; Qian, Dickey et al. 2000; Andrews, Jacques et al. 2002). Other types of nanoscale inclusions, including boron nitride (BN) nanotubes (Bengu and Marks 2001; Demczyk, Cumings et al. 2001), graphite nanoplatelets, nanoclays, and nanowires, while not directly addressed here, have also been proposed as candidate filler materials. NRPs hold vast potential as structural materials due to the extremely high strength- and modulus-to-weight ratios that are likely to be achieved with such materials. Other potential advantages of NRPs include multifunctionality, increased energy absorbance, higher toughness, and ease of manufacturing (particularly if the NRPs can be processed using traditional polymer techniques). Despite the challenges which these materials present in terms of modeling, processing, and most notably the availability and cost of the raw nanotube material, the preliminary results and inherent potential suggest that further study of NRPs is warranted.

In the remainder of this chapter we will introduce the reader to pertinent topics regarding both carbon nanotubes and their use as a reinforcing phase in polymeric materials. This background information will serve as a foundation for later chapters, where we will present models and experimental methodology that have been developed to study the mechanical response of nanotube-reinforced polymers.

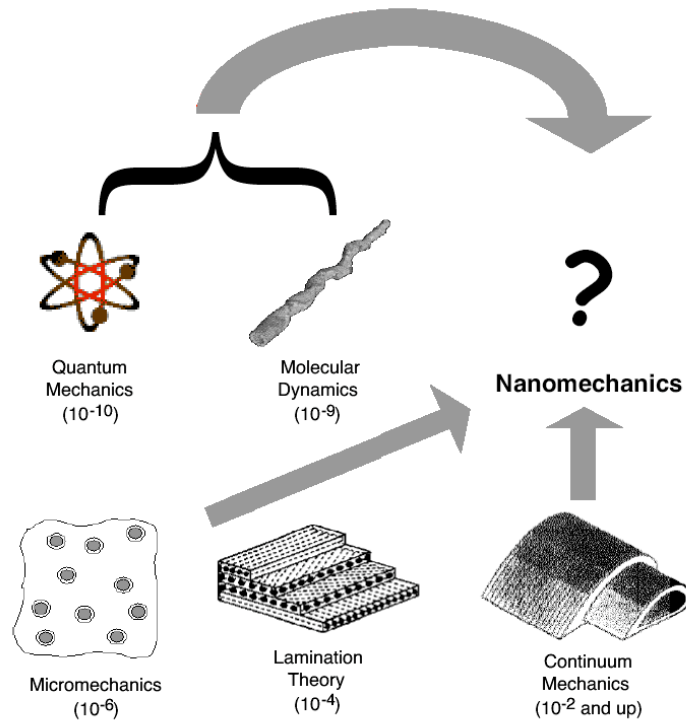


**Figure 1. Nanomechanics and other modeling length scales.**

## Structure of Carbon Nanotubes

Due to the inherent strength of the carbon-carbon bond and the potential of a defect-free structure, it has been suggested that nanotubes may approach the theoretical limits for many important mechanical properties, including axial stiffness and tensile strength. Large increases in fracture strain and toughness, and superior electrical/thermal properties, are other potential benefits of using NTs as the filler material in a polymer-based composite.

The outstanding properties that are predicted (and in some cases verified experimentally) for carbon nanotubes are the result of their structure, which can be pictured as being formed by rolling a graphene sheet into a cylinder. Because the graphene hexagonal lattice can be rolled at different angles, the geometry of a particular nanotube is best described in terms of the unit cell of the carbon nanotube, as shown in Figure 2. The atomic arrangement of the carbon nanotube is described by the chiral vector, which is defined by  $C_h = n\hat{a}_1 + m\hat{a}_2$ , where  $\hat{a}_1$  and  $\hat{a}_2$  are unit vectors on the hexagonal lattice and  $n$  and  $m$  are integers. Using this description the chiral angle ( $\theta$  in Figure 2) and diameter of the nanotube are given as

$$\theta = \tan^{-1} \left( \frac{3n}{2m+n} \right), \quad (1)$$

$$d_t = \frac{3}{\sqrt{3}} a_{C-C} \sqrt{m^2 + mn + n^2}, \quad (2)$$

where  $a_{C-C}$  is the distance between neighboring carbon atoms in a flat graphene sheet (approximately 0.142 nm). As shown in Figure 3, nanotubes with different chiral vectors  $(n,m)$  will have different atomic configurations.

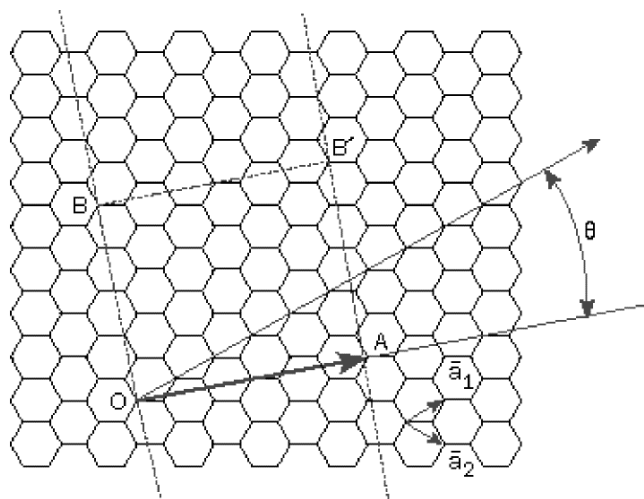


**Figure 2. Unit cell and chiral vector for a (4,2) carbon nanotube.**

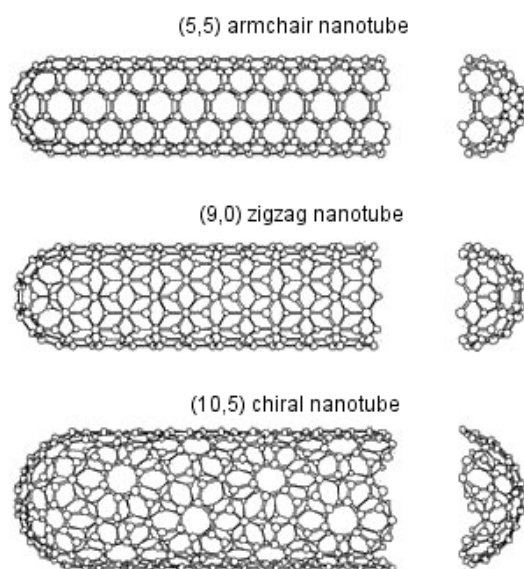


**Figure 3. Examples of nanotubes with different chirality.**

Certain nanotube properties have been found to be strongly dependent on the chirality of the nanotube, including electrical resistivity and fracture behavior. For example, a carbon nanotube will be metallic when the chiral vector satisfies the relationship  $n - m = 3q$ , where  $q$  is an integer, while all other nanotubes will be semiconductive. It has been estimated that 1/3 of all nanotubes are metallic. However, other properties, and in particular the stiffness, have been found to be relatively independent of the chirality. For our modeling work presented later in this dissertation we assume that chirality effects are negligible.

Carbon nanotubes can be further classified into three broad categories: single-walled nanotubes (SWNT), multi-walled nanotubes (MWNT), and nanotube bundles or ropes. SWNTs consist of a single layer of carbon atoms wrapped into a cylindrical shape, which may or may not be capped on each end by one half of a fullerene molecule (see Figure 3). Typical diameters for SWNTs are on the order of 1 nm, while lengths are often on the order of  $\mu\text{m}$ . This results in very large aspect ratios, which in traditional composites theory are desirable from the perspective of load transfer. Both the diameter and the length of the SWNTs are typically dependent on the particular technique used to create the nanotubes.

MWNTs consist of several concentric layers (or shells) of individual carbon nanotubes that are weakly coupled to each other through van der Waals forces. A high resolution transmission electron microscope (TEM) image of a MWNT is shown in

Figure 4 (Harris 1999). The spacing between these individual shells is on the order of 0.34 nm, which is slightly larger than the interlayer spacing in a graphene sheet. The diameter and number of shells comprising a MWNT is again dependent on the fabrication process, although diameters on the order of 30 nm may be considered as a ballpark estimate (Pan, Xie et al. 1999; Qian, Dickey et al. 2000).

Typically, nanotubes are found to have self-organized into crystalline bundles (Thess, Lee et al. 1996; López, Rubio et al. 2001), consisting of several to hundreds of SWNTs or MWNTs arranged in a closest-packed two-dimensional lattice. Within these bundles the nanotubes normally display a monodisperse range of diameters, with adjacent tubes weakly coupled via van der Waals interactions. A high resolution TEM image of a SWNT bundle is shown in Figure 5 (Journet, Maser et al. 1997), where the bundle is seen to consist of approximately 20 SWNTs of almost uniform diameter packed in a triangular lattice. The average tube diameter in the bundle is 1.4 nm, and the average spacing between the tubes was reported as 1.7 nm.

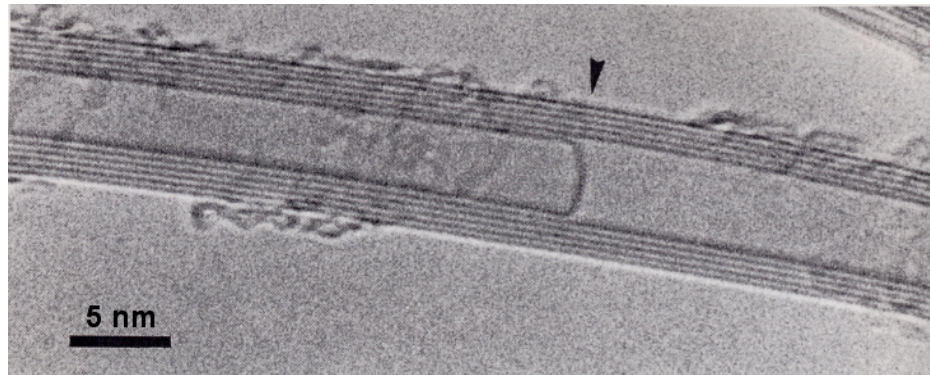


**Figure 4. High resolution TEM image of a MWNT with an internal cap highlighted by the arrow. (Harris 1999)**

While not modeled in the continuum approaches presented later in this work, explicit differences in the structural behavior of these various NT forms will need to ultimately be included in future models of nanotube-related materials. From the perspective of structural reinforcement, optimal behavior will be dependent on the proper transfer of load from the matrix to the inclusion (and among the shells or tubes in the case of MWNTs or NT bundles, respectively). While SWNTs are more susceptible to bending due to their extremely small cross-sections, for MWNTs and NT bundles interlayer sliding (so-called “sword and sheath” slippage (Yu, Yakobson et al. 2000)) and weak intertube coupling, respectively, could hinder load transfer between the phases. Such differences are not included in the models presented in this dissertation and will be the subject of future work.

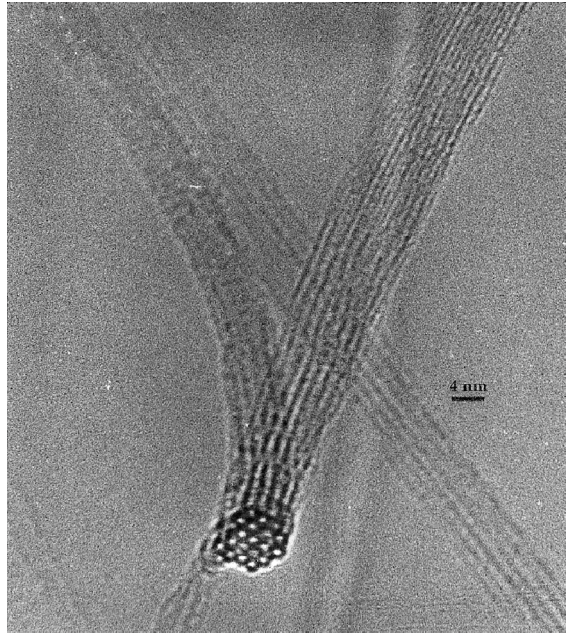


**Figure 5. High resolution TEM image of a SWNT bundle. (Journet, Maser et al. 1997)**

## **Methods of Nanotube Fabrication**

The properties of carbon nanotubes are closely related to their method of production. While an in-depth discussion of nanotube fabrication techniques is well beyond the scope of this dissertation, a summary of production techniques is included below for completeness. The reader is referred to the literature for a fuller description of work in this area.

A summary of some standard nanotube fabrication techniques is given in Table 1. A newer processing technique, flame synthesis, is also currently being developed

(Vander Wal and Tichich 2001). In early work the arc discharge and laser vaporizations processes were the most common forms of nanotube production, typically resulting in nanotubes with low structural defects and thus excellent physical properties. In these techniques SWNTs are typically formed in the presence of a metal catalyst, which seems to preclude the formation of MWNTs. One difficulty associated with these techniques is the need to process the end-product, which are typically found to be quite entangled (see Figure 6); in many cases amorphous carbon and other contaminants on the surface of the nanotubes need to be removed via various purifying techniques. An additional problem with these techniques is that production yields from these methods are rather limited, and do not seem suited to satisfy the long-term goal of ton-quantity production.

In the interest of developing a process that can be scaled for industrial production, a great deal of work has been devoted to techniques that may be classified as chemical vapor deposition (CVD) (Che, Lakshmi et al. 1998; Cassell, Raymakers et al. 1999). While CVD processes have been used to create a wide variety of carbon structures (Endo 1988), the major drawback of these methods is the reduced structural integrity of the nanotubes. For example, experimental work has suggested that the tensile moduli of CVD nanotubes may be more than an order of magnitude lower than those measured for nanotubes created via other methods (and hence with fewer structural defects) (Salvetat, Kulik et al. 1999). However, promising CVD techniques

that seem to produce nanotubes with fewer defects (and hence better physical properties) are currently under development (Cassell, Raymakers et al. 1999).

<b>Method</b>	<b>Arc discharge (carbon arc) (Ebbesen and Ajayan 1992)</b>	<b>Chemical vapor deposition (CVD) (Endo 1988)</b>	<b>Laser ablation (vaporization) (Thess, Lee et al. 1996)</b>	<b>High-pressure CO conversion (HiPCO) (Bronikowski, Willis et al. 2001)</b>
<b>Summary</b>	Graphite evaporated by a plasma via high currents	Decomposition of a carbon-based gas	Graphite blasted with intense laser pulses	Metal catalysts nucleate SWNTs at high pressure and temperature
<b>Yield</b>	30%	20 to ~100 %	Up to 70%	95% purity, 10 g/day
<b>Strength</b>	SWNT and MWNTs with few structural defects	Easiest to scale to industrial production	Produces SWNTs; diameter control via reaction temperature	Excellent structural integrity for a CVD process
<b>Weakness</b>	Tubes tend to be short and highly entangled	Typically MWNTs with a high density of defects	More expensive than the other methods	Production rates still relatively low

**Table 1. Common methods of carbon nanotube production.**

One of the benefits of the CVD method is that the growth and alignment of the nanotubes can be controlled by the patterning of the catalyst (typically metal) particles, such that very regular nanotube arrays as shown in Figure 7 can be formed. Here the nanotubes are seen to align perpendicular to the surface on which the catalyst has been deposited; results suggest that the nanotubes can be patterned on any suitable

substrate (independent of the geometry) given sufficient conditions (Bower, Zhou et al. 2000). Using techniques such as these it may be possible to create nanotube-reinforced polymers where the arrangement of the nanotubes is ordered and well-controlled. Such control of the orientation, alignment, and dispersion of nanotubes *within* a polymer matrix will be necessary to optimize the material performance of these systems.

A great deal of recent research has focused on limiting the defects within the nanotubes (which are particularly detrimental from a mechanical property perspective), and increasing the production yields from nanotube processing techniques. At the moment this work is quite challenging because detailed models of nanotube growth are not well developed. However, as interest from scientific community continues to expand it is expected that nanotube fabrication techniques will continue to develop. While at the moment the rather limited availability and large expense of nanotubes are hindrances to research in this area, future advances are likely to relax these restrictions.

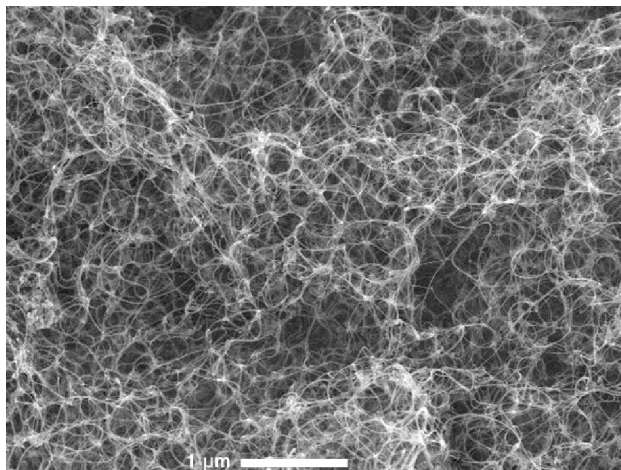


**Figure 6. SEM image of SWNT bundles formed via the arc discharge method.  
(Journet, Maser et al. 1997)**

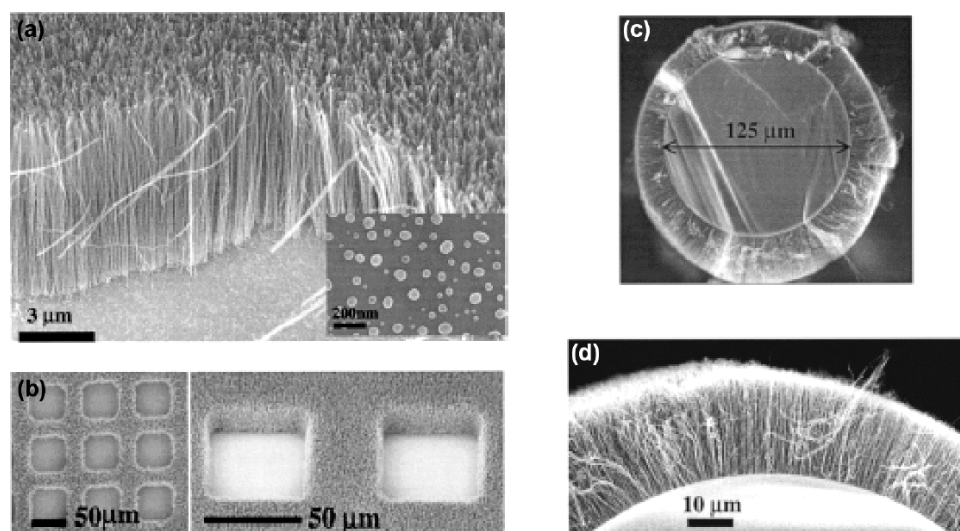


**Figure 7. SEM images of aligned MWNTs grown via microwave plasma enhanced chemical vapor deposition. (Bower, Zhou et al. 2000)**

## **Mechanical Properties of Carbon Nanotubes**

Because we are interested in the use of carbon nanotubes as a reinforcing phase within a polymer material, we will primarily focus on the mechanical properties of carbon nanotubes, a topic of intense research over the last few years. In this section we will review the initial theoretical and computation work in this area. We will also present recent experimental evidence that, despite the obvious complications associated with manipulating objects of such small size, has nonetheless tended to validate these predictions.

### ***Modulus***

Much of the initial work studying the mechanical properties of nanotubes has consisted of computational methods such as molecular dynamics and *ab initio* models. These models are primarily used to study SWNTs because of the increase in computational resources necessary to model systems comprised of a larger number of atoms. Typically these computational studies have found nominal values for the axial Young's modulus on the order of 1000 GPa (assuming a shell thickness of 0.34 nm), with values for the Poisson ratio approximately 0.20 to 0.30 (Gao, Çagin et al. 1998; Hernández, Goze et al. 1998; Che, Çagin et al. 1999; Sánchez-Portal, Artacho et al. 1999). Using an empirical force-constant method, elastic moduli of approximately 1

TPa were calculated for SWNTs and MWNTs, while values for SWNT bundles were between 0.4 and 0.8 TPa and found to be very dependent on the diameter of the individual tubes (Lu 1997). *Ab initio* calculations have found that the mechanical properties of nanotubes are similar to those of graphite down to small nanotube radii (on the order of 3 nm), at which point the properties increase due to the enhanced curvature of the tubes (Sánchez-Portal, Artacho et al. 1999)<sup>1</sup>. Most of these models assume defect-free nanotubes; nanotubes with a significant number of defects (such as those produced via CVD methods) are expected to have much lower moduli values (Salvetat, Kulik et al. 1999; Xie, Li et al. 2000).

More recently, a great deal of progress has been realized in the manipulating and testing of individual nanotubes and nanotube bundles (Treacy, Ebbesen et al. 1996; Falvo, Clary et al. 1997; Krishnan, Dujardin et al. 1998; Salvétat, Bonard et al. 1999; Salvétat, Briggs et al. 1999; Li, Cheng et al. 2000; Yu, Files et al. 2000; Yu, Kowalewski et al. 2000; Yu, Lourie et al. 2000). In general, the experimental results have validated the computational predictions. A summary of these experimental results is given in Table 2 (the reader is referred to the original sources for a more complete description of these methods). While a method of producing large quantities

---

<sup>1</sup> It should be noted that other researchers have suggested that, in order to properly model the bending behavior of the nanotubes, more appropriate values for the Young's modulus and the shell thickness would be on the order of 5 TPa and 0.067 nm, respectively (Yakobson, Campbell et al. 1997; Xin, Jianjun et al. 2000).

of nanotubes with uniform geometric and physical properties has yet to be developed, the high modulus of carbon nanotubes makes them an attractive candidate filler for composite materials.

### ***Strength***

Because strength is closely related to the presence of defects within a material, it has been hypothesized that nanotubes (particularly low defect NTs formed via carbon arc and laser vaporization methods) may approach theoretical limits in terms of strength. In a recent molecular mechanics simulation, NT fracture strains between 10 and 15% were reported, with corresponding tensile stresses on the order of 65 to 93 GPa (compare to the values for other common filler materials listed in Table 3) (Belytschko, Xiao et al. 2002).

Type of NT	Method	Modulus Values	Comments
Laser ablated SWNTs (Krishnan, Dujardin et al. 1998)	Amplitude of thermal vibration within a TEM	1.3 -0.4/+0.6 TPa	Weighted average value of 1.25 TPa
Laser ablated SWNT bundles (Yu, Files et al. 2000)	Nanostressing stage within a SEM	320 to 1470 GPa, mean of 1002 GPa	Load carried by SWNTs on rope perimeter
Carbon arc SWNT bundles (bundle diameters 3-20 nm) (Salvetat, Briggs et al. 1999)	Beam-bending via AFM	~ 1 TPa for 3 nm diameter, decreasing to < 0.1 GPa for larger diameter	Estimated shear moduli of SWNT bundle on the order of 1 GPa
Carbon arc MWNTs (Poncharal, Wang et al. 1999)	Electromechanical deflection and resonance within a TEM	~ 1 TPa for small diameter (<10 nm) to 0.1 TPa for large diameter (>30 nm)	Modulus a strong function of diameter
Carbon arc MWNTs (Yu, Lourie et al. 2000)	Nanostressing stage within a SEM	Modulus of outer shell from ~270 to ~950 GPa	Failure via "sword-in-sheath" mechanism
CVD and carbon arc MWNTs (Salvetat, Kulik et al. 1999)	Beam-bending via AFM	CVD: ~ 10-50 GPa Arc: 810 -160/+410 GPa	Order of magnitude increase after annealing CVD NTs at 2500°C
CVD MWNTs (Pan, Xie et al. 1999; Xie, Li et al. 2000)	Miniature stress-strain tests on 2 mm NT ropes	Young's modulus ~ 0.45 TPa Tensile strength ~ 1.5-3.6 GPa	Lower values attributed to defects in CVD tubes

**Table 2. Experimental values for the Young's modulus of carbon nanotubes.**

Novel experimental work looking at the fracture behavior of nanotubes has recently been carried out using a nanostressing stage located within an SEM (see Figure 8). For SWNT bundles the maximum tensile strain was estimated to be 5.3%, with the tensile strength of the individual SWNTs estimated to be 13 to 52 GPa (Yu, Files et al. 2000). Related tests on MWNTs found that failure occurred via a “sword-in-sheath” mechanism at tensile strains up to 12%, with the tensile strength of the outer shell of the MWNT estimated to be between 11 and 63 GPa (Yu, Lourie et al. 2000). The tensile strength of NTs has been estimated to be 3.6 GPa for CVD-grown MWNTs using a miniature stress-strain puller to test long (2mm) NT ropes, with the order of magnitude decrease in strength attributed to an increase in defects (Pan, Xie et al. 1999; Xie, Li et al. 2000).

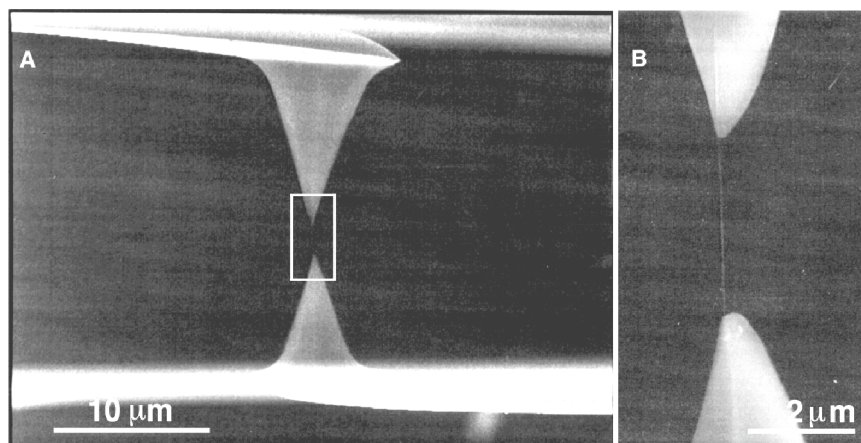


**Figure 8. SEM image of a MWNT loaded in tension between two AFM tips in a nanostressing stage. (Yu, Lourie et al. 2000)**

To place the nanotube moduli and strength predictions into proper perspective, representative values for common types of filler materials for structural reinforcement are given in Table 3. While the predicted properties of carbon nanotubes compare quite favorably to those materials listed in this table, a greater understanding of the nanotubes themselves, and issues related to their use within a polymer matrix, must be developed in order to fully utilize the properties of the nanotubes in structural composites. These issues will be discussed in the next section.

<b>Fiber</b>	<b>Diameter (<math>\mu\text{m}</math>)</b>	<b>Density (<math>\text{g}/\text{cm}^3</math>)</b>	<b>Tensile strength (GPa)</b>	<b>Modulus (GPa)</b>
Carbon	7	1.66	2.4-3.1	120-170
S-glass	7	2.50	3.4-4.6	90
Aramid	12	1.44	2.8	70-170
Boron	100-140	2.50	3.5	400
Quartz	9	2.2	3.4	70
SiC fibers	10-20	2.3	2.8	190
SiC whiskers	0.002	2.3	6.9	-
Carbon NTs	0.001-0.1	$\sim 1.33$	Up to $\sim 50$	Up to $\sim 1000$

**Table 3. Filler materials for structural reinforcement. (Matienzo, Wang et al. 1994)**

## **Carbon Nanotube-Reinforced Polymers**

Given the moduli and strength values that have been predicted (and measured) for carbon nanotubes, they are potentially an ideal filler material for high performance (polymer) composite materials with outstanding modulus-to-weight and strength-to-weight ratios. However, to fully and efficiently utilize the exceptional properties of carbon nanotubes in NRPs for structural reinforcement, several issues related to the fabrication of the NRPs will need to be addressed. These issues are discussed in detail below. We will then present a review of some initial experimental results on NRPs that show promising mechanical property enhancements with the addition of relatively small amounts of carbon NTs. A summary of selected published work regarding carbon nanotube-reinforced polymers is given in the Appendix.

### ***Issues related to the fabrication of NRPs***

Although the fabrication of nanotube-reinforced polymers must be optimized in order to achieve ultimate effective properties, at the moment there are several critical issues that are not well understood in this area. While individual research groups have made significant processing advances for particular nanotube-polymer systems, universal guidelines regarding the fabrication of NRPs do not exist. This is in part due to the complexity of the polymer chemistry, the lack of detailed models

describing the processing conditions, and the large list of parameters (specific to the polymer and type of nanotube under consideration) that can influence the polymer-nanotube interaction and impact the effective NRP properties. Three of these issues are discussed in detail below.

### **Nanotube dispersion with the polymer**

One issue of practical importance for NRPs is the separation and dispersion of the nanotubes within the matrix, which is critical as the nanotubes tend to assemble into ropes or bundles due to van der Waals interactions between the individual tubes. While some researchers have been able to separate individual nanotubes from the bundles via ultrasound and polar solvents, maintaining separated nanotubes during the processing of NRPs is still the subject of ongoing work. Some results suggest that the use of a surfactant as a coupling agent may overcome van der Waals attractive force and allow good dispersion of the nanotubes within the polymer (Gong, Liu et al. 2000). However, it is unclear whether such processing agents can be employed to promote nanotube dispersion without compromising the nanotube-polymer interface.

### **Nanotube orientation**

Optimal material properties will only be achieved if the orientation of the nanotubes within the polymer can be controlled, and several techniques have been

proposed to address this issue. One group found that cutting thin slices (on the order of 100 nm) of a nanotube-reinforced epoxy film introduced preferential orientation via shear flow (Ajayan, Stephan et al. 1994). This flow orientation method has also been used to orient small amounts of NTs (0.1% wt) in a urethane acrylate polymer to thicknesses up to 150  $\mu\text{m}$  (Zhao and Weng 1996; Wood, Zhao et al. 2001). An alternative method that may be more suitable for larger samples is tensile loading of the NRP at temperatures above the glass transition temperature of the polymer (Jin, Bower et al. 1998; Bower, Rosen et al. 1999). A combination of solvent casting and melt mixing was also found to produce a high degree of nanotube alignment (Haggenmueller, Gommans et al. 2000). While individual SWNTs and SWNT ropes have been aligned in the presence of electric (Chen, Saito et al. 2001) and magnetic (Smith, Benes et al. 2000) fields, to our knowledge this method has yet to be extended to nanotube-reinforced polymers.

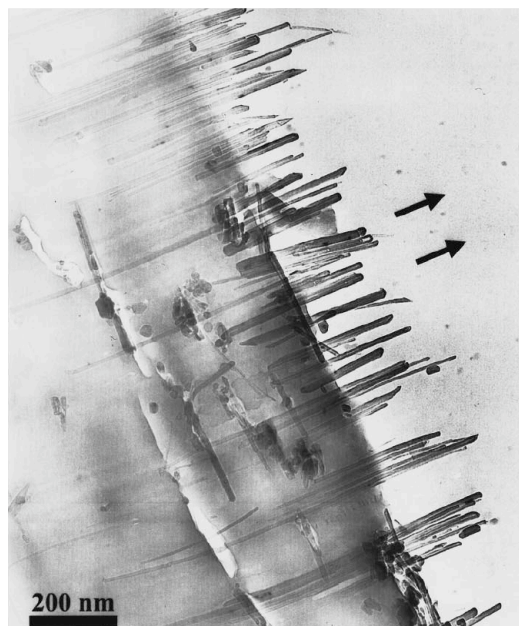


**Figure 9. Alignment of nanotubes in PHAE via microtoming . The sample thickness is 90 nm. (Jin, Bower et al. 1998)**

### **Load transfer across the nanotube-polymer interface**

Another topic of critical importance is the NT-polymer interface and load transfer between the polymer and the nanotubes (Schadler, Giannaris et al. 1998; Bower, Rosen et al. 1999; Jia, Wang et al. 1999; Shaffer and Windle 1999; Ajayan, Schadler et al. 2000; Lordi and Yao 2000; Qian, Dickey et al. 2000; Lozano and Barrera 2001). Poor load transfer for MWNTs and SWNT ropes embedded in a polymer has been attributed to the relative slipping of individual tubes within the MWNT (Schadler, Giannaris et al. 1998) and the rope (Ajayan, Schadler et al. 2000), respectively. However, other researchers have found evidence of promising nanotube-

polymer interactions in composite materials. For example, a strong interface between MWNTs and polystyrene (PS) (Qian, Dickey et al. 2000) and polyhydroxyaminoether (PHAE) (Jin, Bower et al. 1998) has been reported. Analysis of SWNT bundles-PMMA thin films found that PMMA was able to intercalate within the bundles, which would likely enhance the interface between the nanotube and polymer phases (Stéphan, Nguyen et al. 2000). Significant wetting and interfacial adhesion for SWNT bundles embedded in an epoxy resin has also been reported (Lourie and Wagner 1998b). Functionalization of the NTs to increase their chemical reactivity has also been proposed as means to further promote nanotube-polymer interaction (Srivastava, Brenner et al. 1999).

A recent molecular dynamics study suggests that polymer morphology, and specifically the helical wrapping of the polymer around the nanotubes, is a key factor influencing the strength of the interface (Lordi and Yao 2000). Using molecular mechanics to study the interfacial characteristics of a polystyrene-nanotube composite, the interfacial shear stress was estimated to be 160 MPa (Liao and Li 2001). This is comparable to the value of 500 MPa obtained from fragmentation experiments on a polyurethane-NT system, which is an order of magnitude larger than typically measured in conventional fiber-based composites (Wagner, Lourie et al. 1998). Finally, due to their demonstrated adhesion within a urethane matrix, researchers are currently interested in using NTs as nanoscale strain sensing devices. Here low

fractions of nanotubes (0.1% wt) make the host polymer Raman-active, allowing changes in the Raman spectrum to be related to strain within the material (Wood, Zhao et al. 2001; Zhao, Wood et al. 2001). While promising, a much better understanding of the factors that influence the nanotube-polymer interface is required.

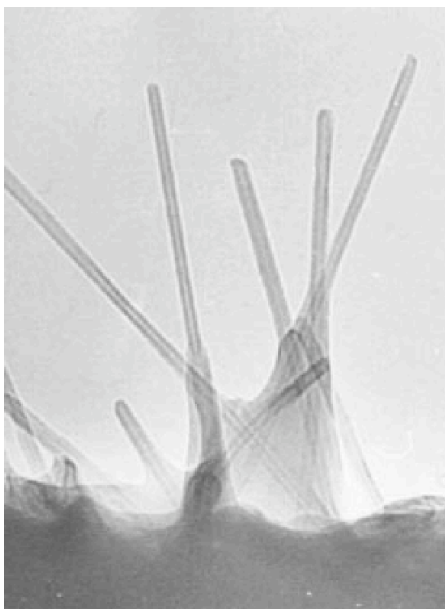


**Figure 10. TEM image showing evidence of PPV wetting the nanotubes. (Curran, Ajayan et al. 1998)**

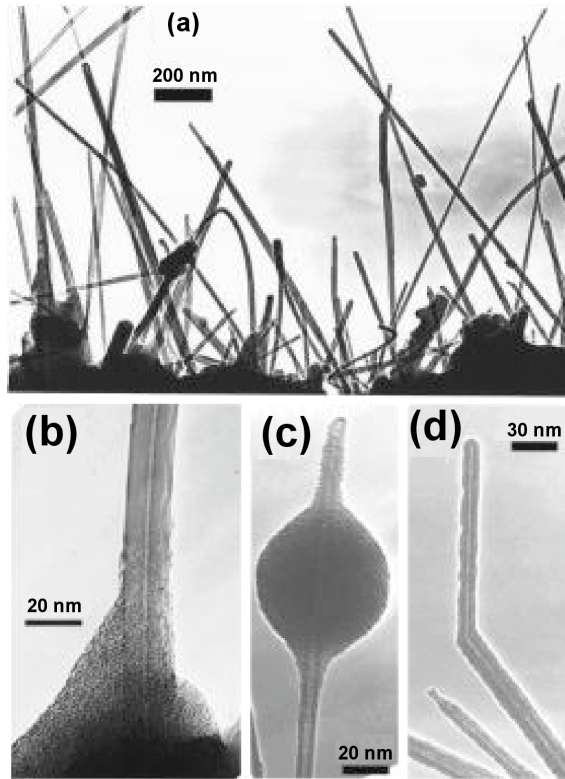


**Figure 11. TEM images of MWNTs in PHAE. (a) Fracture surface. (b,c) Evidence of good adherence between the polymer and the MWNT. (d) Plastically deformed MWNT at fracture surface. (Bower, Rosen et al. 1999)**

The three issues identified above will influence our ability to design and model materials that fully exploit the potential of nanoscale reinforcement. One issue which has not typically been associated with the modeling of NRPs, but which seems critical based on micrograph images of these materials, is the characteristic waviness or curvature of embedded nanotubes. To address how this embedded waviness influences the effective properties of these materials, we have developed a hybrid finite element-micromechanics model that integrates NT waviness into micromechanical predictions

of the NRP effective modulus. Presented in Chapter 3, this model suggests that moderate waviness, while potentially beneficial for other applications (i.e. strength), can drastically reduce the effective stiffness of the NRP when compared to straight nanotube inclusions.

### ***Mechanical Properties of Carbon Nanotube-Reinforced Polymers***

Recently a great deal of experimental work has been presented in the literature looking at the effective properties of polymers reinforced with carbon nanotubes. It is difficult to generalize across these studies because of the large number of parameters that can influence the effective properties, including the method of NT fabrication, size and form of the NT, NRP processing conditions, NT-polymer interaction, and the specifics of the polymer chemistry. However, one constant throughout much of the experimental work is that significant improvements in the properties of the NRP, with respect to that of the un-reinforced polymer, are obtained. In the following sections we highlight some of the relevant work in the literature. A more extensive listing of related work is summarized in the Appendix.

#### **Elastic behavior**

Initial experimental work looking at the effective elastic properties of carbon nanotube-reinforced polymers has suggested that significant property enhancement

can be achieved with the addition of relatively small amounts of carbon nanotubes. In perhaps the first published work in this area, 5 wt% MWNTs were mixed in an epoxy and formed into macroscale (millimeter) samples; the tensile and compression moduli measured in these experiments are given in Table 4 (Schadler, Giannaris et al. 1998).<sup>2</sup> Simultaneous Raman spectroscopy measurements were used to qualitatively measure the strain in the nanotubes as the samples were loaded, and it was reported that the Raman peak position only shifted significantly in compression. It has been suggested that this is evidence that only the outer layer of the MWNT was loaded in tension, whereas all layers of the MWNT are loaded in compression. While poor load transfer between adjacent shells in a MWNT is likely, as they only interact via van der Waals interactions, it is worth noting the both the average tensile and compression moduli in this study increased by approximately 20% in comparison to the response of the pure polymer.

Work with PMMA-based NRPs found that pre-processing CVD-grown MWNTs using a ball mill (treated NTs) resulted in an increase in tensile strength as shown in Table 5 (Jia, Wang et al. 1999). The strength enhancement seen with the NT treatment was attributed to the ball milling operation separating the individual nanotubes (in comparison to the entangled untreated NTs). They also reported that

---

<sup>2</sup> The authors of this study also noted that SEM images show the embedded NTs remain “curved and interwoven” in the NRP, an observation that led to the model described in Chapter 3 incorporating nanotubes waviness into effective moduli predictions for an NRP.

increasing the PMMA polymerization time, prior to adding the NTs, allowed the PMMA molecules to grow larger and wrap the NT. Finally, the authors suggest that the initiator used in the polymerization process (AIBN) may interact with the nanotubes, opening  $\pi$ -bonds that are then free to form bonds with the polymer. SEM images of the fracture surfaces show that the nanotubes are wrapped with PMMA layers, which they suggest is an indication of a strong interface between the phases.

Material	Tensile Modulus (GPa)	Compression modulus (GPa)
Pure epoxy	$3.1 \pm 0.2$	$3.63 \pm 0.25$
NRP	$3.71 \pm 0.5$	$4.5 \pm 1.5$

**Table 4. Tensile and compressive moduli for 5% MWNTs in epoxy (Schadler, Giannaris et al. 1998).**

NT wt%	Tensile strength (MPa)	
	Untreated NTs	Treated NTs
0	54.90	54.90
1	~21	58.70
3	~20	66.80
5	NA	71.66
7	NA	71.65
10	NA	47.15

**Table 5. Tensile strength for PMMA-based NRP with treated and untreated MWNTs. (Jia, Wang et al. 1999)**

Researchers at the University of Kentucky have published experimental work measuring the tensile moduli and strength of 1 wt% MWNTs in polystyrene. A homogeneous distribution (on the  $\mu\text{m}$  scale) of MWNTs was achieved by an ultrasound-assisted solution-evaporation method. They found a 25% increase in the tensile strength and an approximately 40% increase in the tensile modulus, with both values being relatively independent of nanotube length. TEM images suggest that cracks propagate in regions of relatively low NT density, and that the MWNTs tend to align and bridge the crack prior to failure (see Figure 12). Eventual failure of the NRP was due to either NT fracture or pull-out from the matrix. Because NTs aligned parallel to the direction of crack propagation tended to break between the crack faces

(rather than pull-out from the matrix), the authors concluded that a relatively strong interface exists between the two phases.

More recent work from the same Kentucky group has looked at the effective NRP modulus for variable loadings of MWNTs in polystyrene (Andrews, Jacques et al. 2002). The CVD grown MWNTs have an average diameter of about 25 nm and are approximately 40  $\mu\text{m}$  long prior to NRP processing. As a means to develop a processing method that would be compatible with industry capabilities, the samples were prepared by shear mixing in a Haake Polylab bowl mixer using roller rotors. Such a procedure has been reported to yield excellent dispersion (Andrews 2001). One drawback of this fabrication method is that it may shorten the length of the nanotubes. Those researchers, however, believe that mild enough conditions were used such that this shortening was negligible.

The tensile moduli values obtained in this study are shown in Figure 13 and compared with the standard Rule of Mixtures upper and lower bounds and a micromechanics (Mori-Tanaka) model assuming a 3D random orientation of nanotubes with a nanotube modulus of 450 GPa (Fisher, Bradshaw et al. 2002b).<sup>3</sup> Within the NRP the nanotubes are likely to randomly orientated in three-dimensional space, which reduces the optimal effective modulus by approximately a factor of four

---

<sup>3</sup> The nanotube modulus of 450 GPa used here is an estimate based on experimental measurements made on similarly grown CVD MWNTs (Pan, Xie et al. 1999; Andrews 2001).

(when compared to the case of aligned nanotubes, which is closely modeled by the Rule of Mixtures upper bound). The experimental modulus enhancements shown here are not as substantial as reported in other works, which is attributed to insufficient bonding between the nanotubes and the matrix as verified in TEM images showing significant nanotube pullout from the polymer (Andrews 2001). Improvements in the interfacial characteristics of this particular system may result in even larger improvements in effective properties.

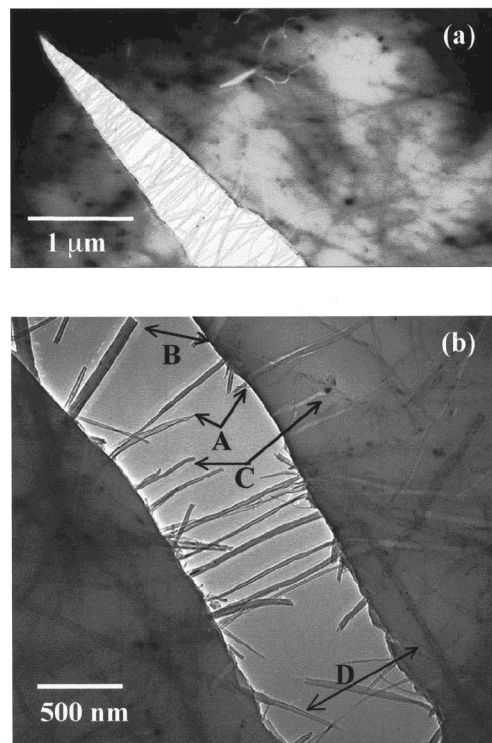


**Figure 12. TEM observation of crack propagation and nanotube crack bridging in an epoxy-MWNT sample. (Qian, Dickey et al. 2000)**

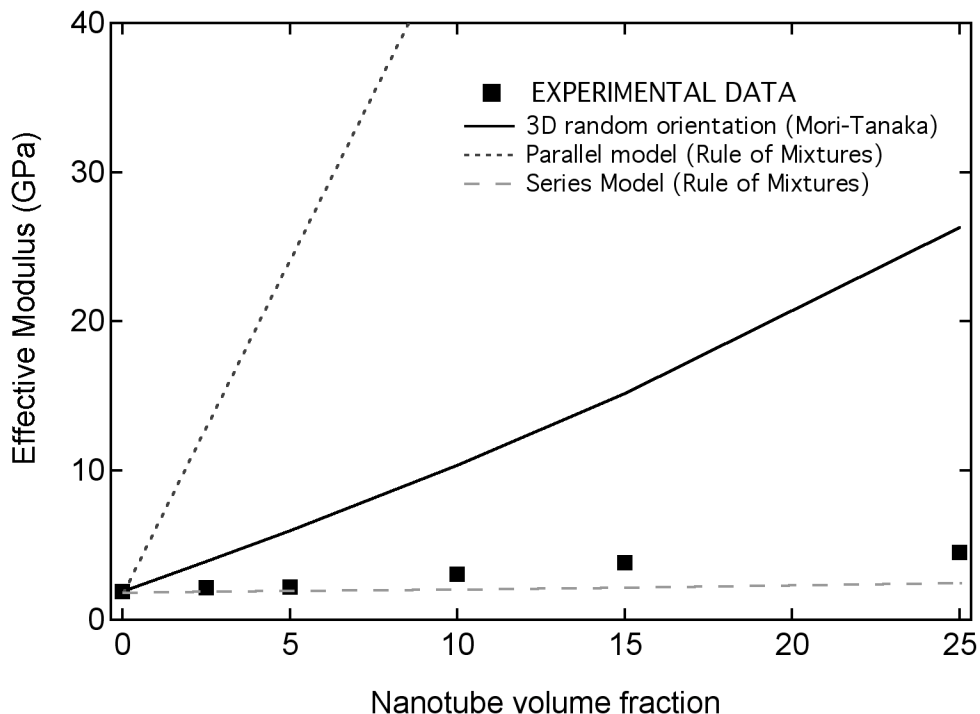


**Figure 13. Comparison of experimental data for MWNTs in polystyrene (Andrews, Jacques et al. 2002) with Rule of Mixtures and Mori-Tanaka predictions.**

### Viscoelastic behavior

In addition to the work discussed above, a limited amount of experimental research has looked at the effective viscoelastic (time- and temperature-dependent) behavior of nanotube-reinforced polymers. Because the nanotubes are on the same size scale as the polymer chains, they are expected to alter the mobility of the polymer chains and thus change the viscoelastic response of the NRP with respect to the un-

reinforced polymer. Probing the mechanical response of the NRP as a function of temperature typically shows four characteristic changes in the material response as shown Figure 14 and Figure 15:

1. Increases in the low temperature (below the polymer glass transition temperature  $T_g$ ) storage modulus, similar to the elastic behavior discussed previously,
2. Significant increases in the high temperature (above  $T_g$ ) response of the material,
3. Shifting of the effective glass transition temperature of the material, usually to temperatures greater than the  $T_g$  of the polymer,
4. Broadening of the loss moduli and loss tangent peaks, suggesting the presence of polymer regions exhibiting non-bulk polymer properties.

Examples of the temperature-dependent response of nanotube-reinforced polymers are shown in Figure 14 and Figure 15 for MWNTs in epoxy (with and without surfactant) and PVOH, respectively. In Figure 14, comparing the response of the pure epoxy (curve 1) to that of the epoxy-1% MWNTs-surfactant sample (curve 4) shows a 25 °C shift in the glass transition temperature (from 63 to 88 °C), as measured by the peak of the loss tangent curve. A smaller shift in  $T_g$  was also seen when the NRP was processed without surfactant (see curve 3). Storage moduli results for these

samples show increases of over 30% for the NRP processed with surfactant. The greater property improvements observed with the use of surfactant were attributed to better nanotube dispersion within these samples.

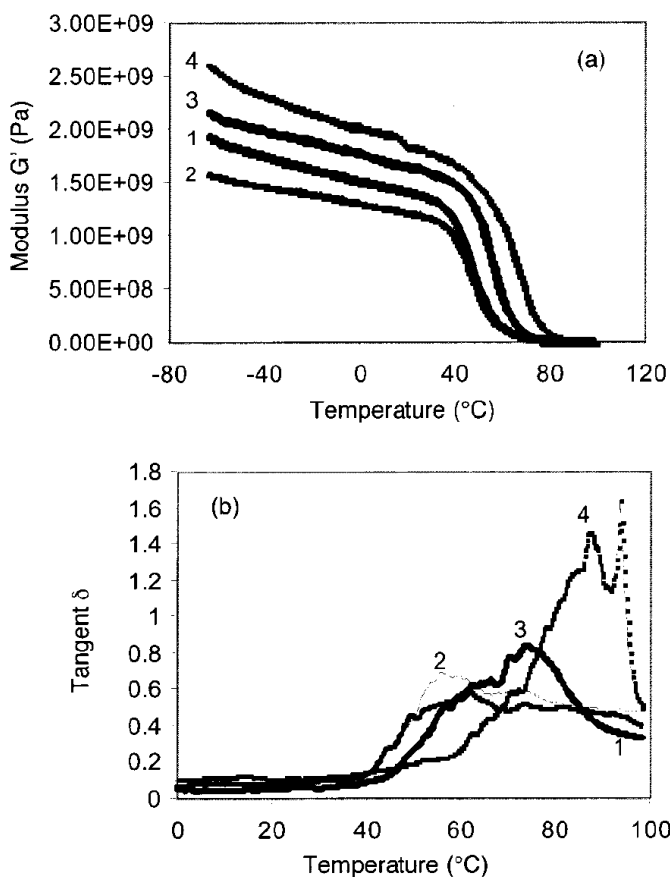


**Figure 14. Storage modulus and loss tangent results via dynamic mechanical analysis for different epoxy samples. Curves are labeled as: (1) pure epoxy, (2) epoxy plus  $\text{C}_{12}\text{EO}_8$  surfactant, (3) epoxy plus 1% wt MWNTs, and (4) epoxy plus surfactant plus 1% wt MWNTs. (Gong, Liu et al. 2000).**

Similar changes in viscoelastic behavior have been seen with MWNTs incorporated into poly(vinyl alcohol) (PVOH) as shown in Figure 15. Composite films were made by a solution casting process, followed by controlled evaporation to produce thin films with thicknesses on the order of 50  $\mu\text{m}$ .<sup>4</sup> While the peak of the loss tangent curve does not appear to shift with the addition of the nanotubes (for all samples the  $T_g$  was found to be between 75 and 80  $^{\circ}\text{C}$ ), the high-temperature portion of the peak broadens as the fraction of nanotubes increases. This was attributed to a reduction of polymer chain mobility in the reinforced samples. Polymers reinforced with vapor-grown carbon nanofibers (diameters of 20-200 nm) (Lozano and Barrera 2001), nano-sized cellulose whiskers (Brechet, Cavaille et al. 2001), and various nanoclays (Liu and Wu 2002; Wu, Liu et al. 2002; Xiao, Sun et al. 2002) have also been found to have a viscoelastic response significantly different than that of the bulk polymer.

Based on these findings, we have conducted dynamic mechanical testing of MWNTs embedded in polycarbonate to study different viscoelastic characteristics (glass transition temperature, relaxation spectra, and physical aging) of the material. Our results for each mode of viscoelastic response are consistent with the hypothesis

---

<sup>4</sup> Based on other work in the literature it seems surprising that NRP samples with up to 60 wt% MWNTs have been successfully fabricated. While the property enhancements with larger amounts of nanotubes are still significant, it is likely that the dispersion of the nanotubes within these samples was quite poor.

that within the NRP there are regions of polymer in the vicinity of the nanotubes with reduced mobility; we model this as an interphase region with viscoelastic properties different from that of the bulk polymer. This work is discussed in much greater detail in Chapter 4 of this dissertation.

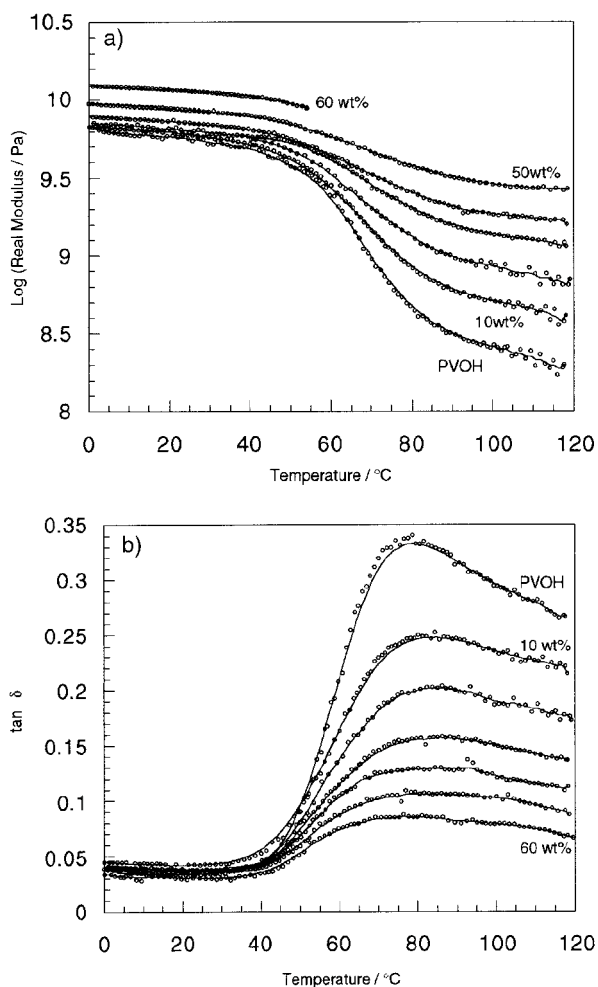


**Figure 15. Dynamical mechanical analysis of PVOH with different loadings of CVD grown nanotubes. (Shaffer and Windle 1999)**

## Other properties

While the work in this dissertation focuses on the mechanical behavior of NRPs, other researchers are looking to leverage the extraordinary electrical and thermal conductivities of the nanotubes to create multifunctional materials with improved electrical and thermal properties. For example, the addition of low volume fractions of NTs is being pursued as a means to increase the conductivity of insulating polymers from  $\sim 10^{-9}$  S/m to  $10^{-6}$  S/m, the level required to provide electrostatic discharge and electromagnetic-radio frequency interference protection (Sandler, Shaffer et al. 1999; Shaffer and Windle 1999). Often in such cases, any improvements in mechanical properties are viewed as an additional benefit; what is more critical is that the optical properties and finish of the sample remain unchanged.

The impact of the nanotubes on the effective electrical conductivity of NRPs are shown in Figure 16 and Figure 17 for CVD nanotubes in epoxy and arc grown MWNTs in poly(*m*-phenylenevinylene-*co*-2,5-dioctoxy-*p*-phenyleneviylene) (PmPV), respectively. In each case substantial increases in conductivity have been attributed to a percolation-type process, which is achievable for relatively low volume (weight) fractions of the nanotubes due to their high aspect ratio and outstanding conducting properties. As shown in Figure 16, the nanotubes are much more efficient than the carbon black filler which is currently added to improve polymer conductivity. Similar

increases in thermal conductivity using small amounts of nanotubes have also been reported (Biercuk, Llaguno et al. 2002).

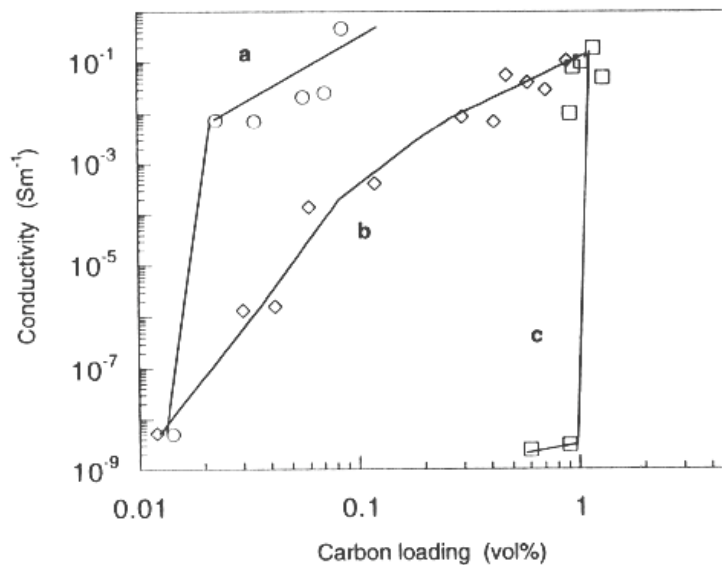


**Figure 16. Electrical conductivity of CVD grown NTs in an epoxy. (a) CVD grown NTs. (b) carbon black with copper-chloride. (c) carbon black only. (Sandler, Shaffer et al. 1999)**

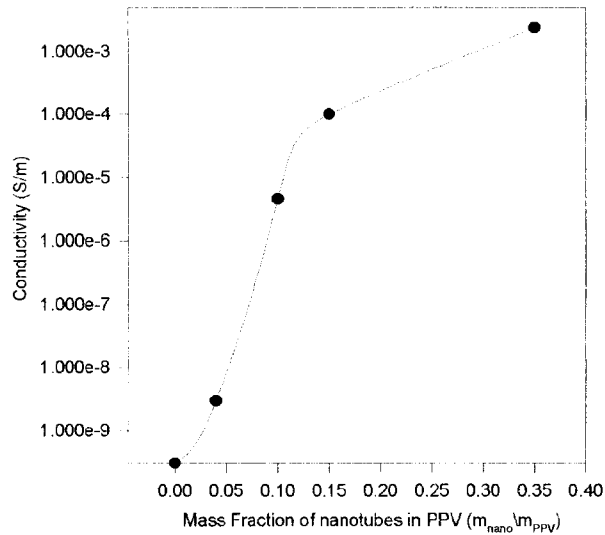


**Figure 17. Electrical conductivity of PmPV/nanotube composites. (Curran, Ajayan et al. 1998)**

For purposes of this dissertation we will limit our discussion to the mechanical behavior of polymers reinforced with small volume fractions of carbon nanotubes. Our focus is on the extension of traditional micromechanics and viscoelastic models for the study of nanotube-reinforced polymers, so that from these models we can start to better understand the impact of the nanotubes on the mechanical response of the material. Two models have been developed in this regard, and will be presented in the next two chapters:

- In Chapter 3, we present a hybrid finite element – micromechanics model that incorporates the typically observed waviness of embedded nanotubes into micromechanics predictions of the effective elastic modulus of an NRP.

- In Chapter 4, we present experimental evidence of a reduced mobility, non-bulk polymer region, which we attribute to the interaction between the nanotubes and the polymer chains. The effect of this interaction is modeled as a shift in the relaxation times of the non-bulk polymer properties and results in a change in the effective viscoelastic properties of the NRP.

The results presented in this chapter demonstrate the complexity of modeling the effective behavior of NRPs. The models presented in the next chapters represent initial efforts to extend existing constitutive models in order to meet this challenge.

# **CHAPTER 3: NANOTUBE WAVINESS AND THE EFFECTIVE MODULUS OF NANOTUBE-REINFORCED POLYMERS**

## **Introduction**

In order to increase our understanding of the mechanical behavior of nanotube-reinforced polymers, it is useful to develop models of the effective properties of these materials, enabling detailed study of the material system. One means to accomplish this is the extension of traditional micromechanics and composite models to address specific features characteristic of these materials. As an example, consider the high-magnification electron microscopy images of nanotubes embedded in a polymer matrix shown in Figure 18. In the images the nanotubes appear to be wavy (not straight), a feature not typically associated with traditional fiber reinforced composites. Note that this waviness is inherently distinct from the uniform and controlled waviness of the yarns in traditional textile composites. While one might expect that this waviness will reduce the effectiveness of these inclusions for purposes of modulus enhancement, modeling of this reduction will lead to more accurate quantitative models of the mechanical behavior of these materials.

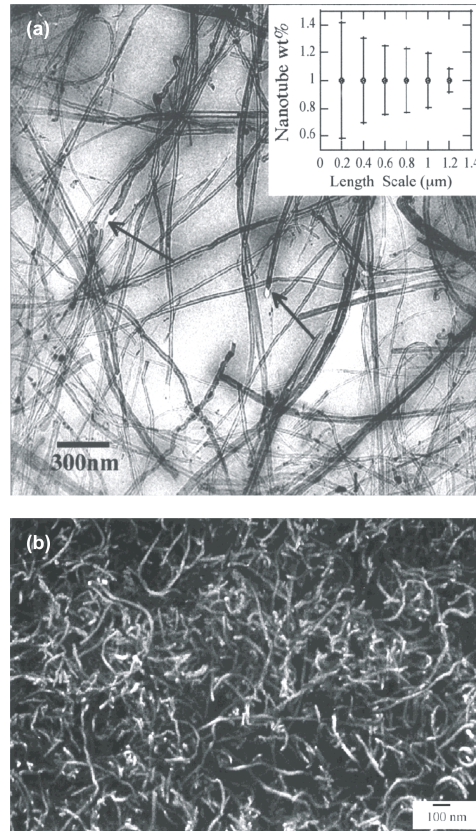


**Figure 18. Micrographs showing the waviness of nanotubes embedded in polymers. (a) TEM image of 1 wt% MWNTs in polystyrene (Qian, Dickey et al. 2000). (b) SEM image of 50 wt% MWNTs in poly(vinyl alcohol). (Shaffer and Windle 1999)**

Motivated by such observations, the model presented in this chapter has been developed to analyze how this waviness impacts the effective moduli of NRPs. This is accomplished via a hybrid finite element-micromechanical model that determines the *effective reinforcing modulus* (ERM) of a wavy embedded nanotube. As demonstrated later in this chapter, the effective reinforcing modulus is then used within a multiphase

micromechanics model to predict the effective modulus of a polymer reinforced with a distribution of wavy nanotubes. We found that even slight nanotube curvature significantly reduces the effective reinforcement in comparison to models assuming straight nanotubes. Using experimental data, we demonstrate that nanotube waviness can significantly limit the property enhancement of the NRP. Thus nanotube waviness may be one reason why the modulus enhancements for NRP systems measured to date, while significant, have been much less than would be anticipated using standard micromechanics models.

At the moment it is impossible to differentiate the impact of nanotube waviness from competing reinforcement-limiting mechanisms such as a weak NT-polymer interface, poor dispersion, and NT degradation in experimental data. Nevertheless, our results provide a clear picture of how moderate waviness can hinder the effectiveness of NTs as structural reinforcement. While the work reported here is an application of a micromechanics method to a nanostructured material, the integration of atomic scale modeling could readily be adapted into such an analysis. In the future a fusion of true nanoscale and microscale modeling will provide even more insight, and quantitatively accurate predictions, of this material behavior.

Next we will describe the models that were developed to determine the effective reinforcing moduli of an embedded wavy nanotube. We will then show how the results of this finite element modeling can be incorporated into micromechanics

techniques to determine the effective modulus of an NRP with randomly orientated, wavy nanotubes. We will then present results that demonstrate how the waviness of the nanotube limits the effective reinforcement that the inclusion provides the host polymer material. This reduced reinforcement results in effective moduli predictions that are significantly lower than those derived assuming straight nanotube inclusions. In all cases these reduced moduli values are in closer agreement with experimental data published in the literature, although currently it is impossible to separate the effects of NT waviness from other reinforcement-limiting mechanisms influencing the effective material behavior. We will also briefly describe an alternative (albeit related) model that has been developed and addresses the impact of NT waviness via the numerical calculation of the dilute strain concentration tensor (Bradshaw, Fisher et al. 2002). At the end of the chapter we will summarize the results of these models and discuss how these results may influence future developments in the area of nanotube-reinforced polymers.

## **The Model**

Based on the discussion of the last section, we are interested in using micromechanical techniques to study the effective elastic moduli of nanotube-reinforced polymers. The basis of the current model is to determine the *effective*

reinforcing modulus (ERM) of the wavy embedded nanotube; that is, a *representative* value denoted  $E_{ERM}$  that accounts for the reduction in reinforcement provided by the wavy nanotube in comparison to the reinforcement provided by a straight NT (of modulus  $E_{NT}$ ).<sup>1</sup> Thus while the nanotube modulus  $E_{NT}$  is a material property, the effective reinforcing modulus  $E_{ERM}$  ( $E_{ERM} \leq E_{NT}$ ) is a material parameter that is a function of the geometry of the wavy nanotube and other variables (as discussed later in this chapter). This effective modulus is then available for use in standard micromechanical models in lieu of the true (actual) nanotube modulus. While such a procedure can be applied in general to any class of curved and wavy inclusions, embedded nanotubes and NRPs are the focus of the present discussion.

In this regard, we note the results of several researchers who found that continuum models provide useful insight into nanotube behavior, despite the discrete nature of their atomic structure (Ruoff and Lorents 1995; Yakobson and Smalley 1997).<sup>2</sup> To simplify the geometry we will treat the nanotube as a solid element of circular cross-sectional area, which implicitly introduces two simplifications into the analysis. First, treating the inclusion as a solid cylinder neglects the hollow nature of

---

<sup>1</sup> This effective reinforcing modulus  $E_{ERM}$  is identical to what we have called the wavy nanotube modulus ( $E_{wavy}$ ) in previous work (Fisher, Bradshaw et al. 2002a).

<sup>2</sup> Others have found a large number of atomic layers was necessary to justify the treatment of the nanotube as a continuum (Govindjee and Sackman 1999). However, for the purposes of moduli predictions we believe that a continuum assumption is an acceptable simplification. Other mechanical behavior, such as crack propagation and fracture, will undoubtedly be more dependent on atomic structure and may be especially ill-suited for such an assumption.

the nanotubes.<sup>3</sup> Second, by modeling the nanotube as a continuum we are disregarding the specific form of the nanotube (SWNT, MWNT, or bundle) and neglecting any possible relative motion between individual shells or tubes in a MWNT and an NT bundle, respectively. Each of these assumptions suggests that  $E_{ERM}$  as calculated here is an “upper bound” for the given model, in that accounting for the hollow nature of the NTs or modeling relative sliding of the tubes or shells would further reduce the effective stiffness of a wavy nanotube. Thus nanotube waviness may be even more significant than the results presented in this work would indicate. While this approach will highlight the impact of nanotube waviness on the effective modulus of an NRP, a more rigorous analysis that accounts for the discrete nature of the nanotube and the atomic interaction between the nanotube and polymer is warranted and will be the subject of future work.

In addition to the continuum assumption, several other simplifications are invoked throughout this work to aid in the interpretation of the results. The individual phase materials are modeled as linear elastic and isotropic, and perfect bonding between the phases is assumed. The waviness of a nanotube of diameter  $d$  will be introduced by prescribing an embedded NT shape of the form  $y = a \cos(2\pi z / \lambda)$ , where  $\lambda$  is the sinusoidal wavelength and  $z$  is the fiber axial direction (see Figure 21

---

<sup>3</sup> It is also well established that in many cases the cross-section of the nanotubes is not circular but is typically distorted due to van der Waals interactions between the shells (or tubes). However, for our current investigation the effect of this slight distortion in cross-sectional shape is negligible.

on page 63). Unless otherwise noted, Poisson ratios of 0.30 were assumed for all phases in the simulations; this value is representative of a wide range of polymer materials, and is consistent with the range of values estimated for carbon nanotubes. This assumption will be discussed in more detail later in this chapter.

We will first present our initial efforts to develop an analytical model describing the extension of a wavy NT in response to an applied axial load. While it was useful to consider such an initial model, we found that its utility was greatly limited due to the inability to accurately capture the influence of the surrounding matrix on the response of the wavy nanotube. This led us to study the problem via the finite element analysis, where the constraint of the surrounding matrix can now be considered. Following this, the formulation of the Mori-Tanaka method for a multiphase composite with randomly aligned cylindrical inclusions in two- and three-dimensional space will be presented. Finally, we will present a multiphase composite approach where the nanotubes are modeled as a finite number of discrete inclusion phases with distinct effective moduli based on their embedded waviness.

### ***Analytical solution for an isolated wavy nanotube***

A critical component of the problem at hand is to model the mechanical response of an *embedded* wavy nanotube, due to an applied axial load  $P$ , as a function of waviness. As a first approximation it is insightful to consider the analytical solution

for the effective stiffness of a *free-standing* wavy rod subject to axial load. We will later show that such a model is only useful when the modulus of the *straight* nanotube  $E_{NT}$  is much larger than the modulus of the matrix  $E_{matrix}$ . When this criterion is not satisfied (i.e.  $E_{NT}/E_{matrix} < 1000$ ), a finite element analysis is necessary to account for the lateral constraint that the surrounding matrix provides the embedded nanotube. For completeness, we briefly describe the analytical solution for a free-standing wavy rod below.

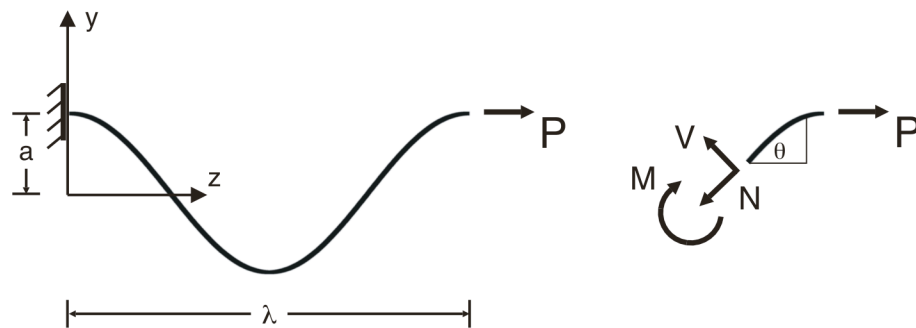


**Figure 19. Schematic of the analytical solution for a free-standing wavy fiber.**

Consider the sinusoidal wavy rod of solid cross-section shown in Figure 19. Assuming linear elastic material behavior and small displacements, Castigliano's theorem states that the displacements due to an applied load  $P$ , in the direction of  $P$ , are given by  $\Delta_P = \partial U / \partial P$ , where  $U$  is the total elastic strain energy of the system (Boresi, Schmidt et al. 1993). Given the sinusoidal geometry of the free-standing

nanotube, one can determine the internal axial ( $N$ ) and shear ( $V$ ) forces and the internal moment ( $M$ ) within the rod as a function of  $z$ :

$$\begin{aligned}
 N(z) &= P \cos(\varphi) = \frac{P}{\sqrt{1 + \frac{4a^2}{\varphi^2} \sin^2 \left( \frac{2\varphi z}{\varphi} \right)}}, \\
 V(z) &= P \sin(\varphi) = \frac{\frac{2a}{\varphi} P \sin \left( \frac{2\varphi z}{\varphi} \right)}{\sqrt{1 + \frac{4a^2}{\varphi^2} \sin^2 \left( \frac{2\varphi z}{\varphi} \right)}}, \\
 M(z) &= P[a \varphi y(z)] = Pa \frac{\varphi}{\varphi} \cos \left( \frac{2\varphi z}{\varphi} \right).
 \end{aligned} \tag{3}$$

The total end displacement  $\varphi_P$  of the rod is then the sum of the components due to each of these terms, integrated over one wavelength  $\varphi$  of the sinusoidal rod,

$$\varphi_P = \varphi_N + \varphi_V + \varphi_M = \varphi \left[ \frac{N}{EA} \frac{\partial N}{\partial P} ds + \frac{kV}{GA} \frac{\partial V}{\partial P} ds + \frac{M}{EI} \frac{\partial M}{\partial P} ds \right], \tag{4}$$

where  $\varphi_N$ ,  $\varphi_V$ , and  $\varphi_M$  are the contributions due to the internal axial and shear forces, and the internal moment, respectively, and  $ds$  is an increment of arc length. In this expression  $k$  is the correction factor for the shear strain energy (equal to 1.33 for a solid circular cross section (Boresi, Schmidt et al. 1993)),  $G$  is the shear modulus, and

$A$  and  $I$  are the cross sectional area and the moment of inertia for a circular cross section. By substituting (3) into (4) and with further simplification, the components of the axial displacement of the free-standing wavy rod are

$$\Delta_N = \frac{P}{AE} \int_0^L \frac{1}{\sqrt{1 + \frac{4a^2}{L^2} \sin^2 \frac{2\pi z}{L}}} dz, \quad (5)$$

$$\Delta_V = \frac{4a^2 \pi^2 kP}{AG \pi^2} \int_0^L \frac{\sin^2 \frac{2\pi z}{L}}{\sqrt{1 + \frac{4a^2}{L^2} \sin^2 \frac{2\pi z}{L}}} dz, \quad (6)$$

$$\Delta_M = \frac{a^2 P}{IE} \int_0^L \cos \frac{2\pi z}{L} \sqrt{1 + \frac{4a^2}{L^2} \sin^2 \frac{2\pi z}{L}} dz. \quad (7)$$

Given these displacement components, the total displacement of the end of the rod is given via (4). Note that in the limit of a straight rod ( $a=0$ ), the above expression yields the standard expression for the extension of straight rod under uniaxial tension,

$$\Delta = \frac{PL}{AE}.$$

We now define the *effective* reinforcing modulus of the free-standing wavy rod as the ratio of the applied stress to the resulting strain, such that

$$E_{\text{free}} = \frac{\sigma}{\epsilon} = \frac{P/A}{\epsilon_p/L} = \frac{PL}{A\epsilon_p}. \quad (8)$$

This expression, normalized with respect to the true modulus, is plotted versus waviness  $w$  (defined as the ratio of sinusoidal amplitude to wavelength  $a/\lambda$ ) in Figure 20 for  $\lambda/d=100$ . Also shown in Figure 20 are the results of an analogous finite element model (described later in the chapter), which indicate excellent agreement between the two solutions. The slight difference between the solutions is attributed to the imposed displacement boundary conditions in the finite element model, which prevent vertical displacement of the rod at  $z=0$ . As expected, the effective modulus quickly falls off with increasing waviness, such that for even very minimal values of waviness the effective stiffness is negligible (i.e. for  $w=a/\lambda=0.01$ , the effective stiffness is less than 5% of the true modulus).

We found that this analytical solution is limited in the present analysis because it does not reflect the physical nature of the constraint imposed by the surrounding matrix. Specifically, comparison of this analytical solution with our finite element results for an embedded wavy nanotube (described later) show that the free-standing solution severely underestimates the effective stiffness of embedded wavy inclusions. As demonstrated in Figure 20, if one were to use the analytical model in (8), it would be possible for the effective reinforcing modulus of a stiff inclusion to be less than the

matrix modulus. As such the wavy nanotube would *decrease* the effective modulus of the NRP, a result that is clearly not realistic.

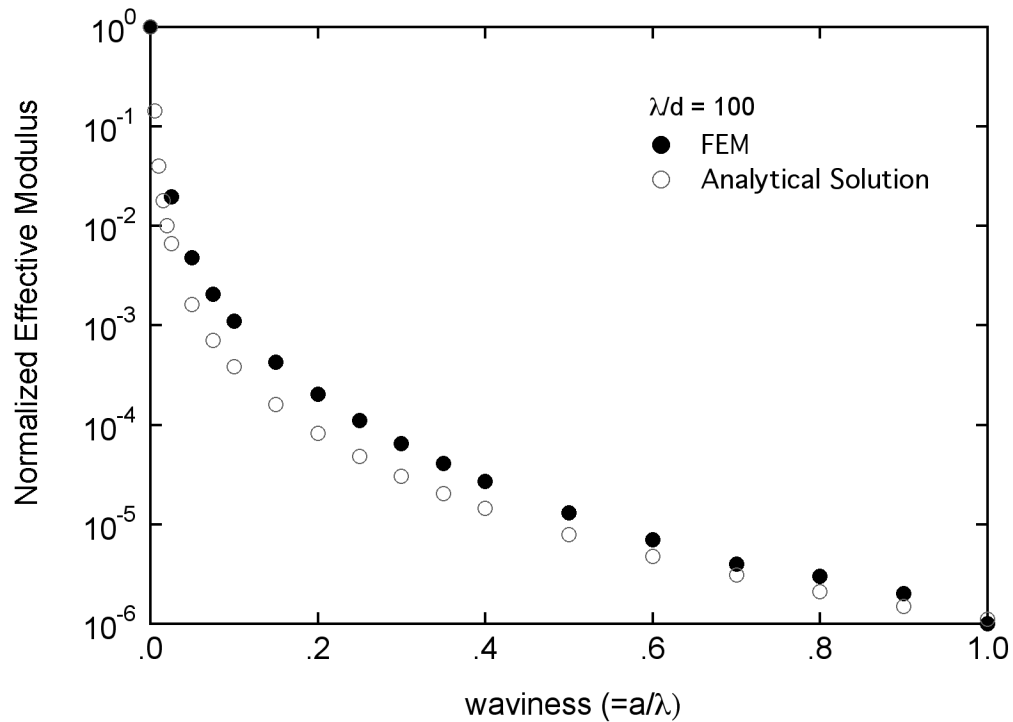


**Figure 20. Comparison of finite element and analytical solutions for the effective modulus of a free-standing wavy rod.**

Attempts to adapt this analytical solution for the case of the embedded wavy inclusions were not successful, primarily because of the difficulty in accounting for the additional constraint of the surrounding matrix. For example, the Rule of Mixtures approximation is ill-suited for this analysis because the volume fraction of the free-standing nanotube is not well defined. This difficulty is eliminated in our finite

element model of the effective reinforcing modulus, which is discussed in the next section and will be the focus of the remainder of this chapter.

### ***Finite element model for the effective reinforcing modulus***

To determine the effective reinforcing moduli  $E_{ERM}$  of an embedded wavy nanotube, ANSYS<sup>TM</sup> was used to create and analyze a three dimensional finite element model of a single, infinitely long wavy nanotube of diameter  $d$  perfectly bonded within a matrix material. For axial loading the problem is symmetric about the  $x=0$  and  $z=n\pi/2$  (where  $n$  is an integer) planes; thus the quarter-symmetric unit cell shown in Figure 21 is used for the analysis. The size of the cell was chosen such that the effective cell response is independent of additional matrix material (this proof is provided later in this chapter). A more complete description of the finite element modeling used here has been described in the literature (Bradshaw, Fisher et al. 2002).

For the finite element simulations symmetry conditions  $u_x=0$  and  $u_z=0$  were prescribed on the  $x=0$  and  $z=0$  planes, respectively. The model was constrained in the  $y$  direction at a single point to prevent free body translation, and an infinitesimally small axial displacement,  $\Delta$ , prescribed to all nodes on the plane  $z=\pi/2$ . The effective modulus of the finite element cell is defined as

$$E_{cell}^{FEA} = \frac{F_{tot} \Delta}{2 A \Delta}, \quad (9)$$

where  $F_{tot}$  is the sum of all nodal resultant forces on the displaced plane and  $A$  is the cross-sectional area of the cell.

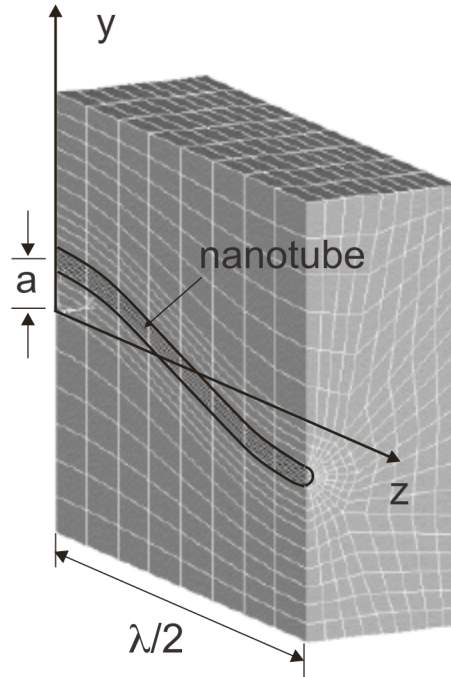


**Figure 21. Finite element cell model of an embedded wavy nanotube. For the model shown,  $w=a/\lambda=0.1$  and  $\lambda/d=35$ .**

In order to extract the effective reinforcing moduli of the *embedded* wavy inclusion (as it exists in the matrix) from (9), we propose a parallel model of the effective cell response, independent of the previous analysis,

$$E_{cell}^{parallel} = c_{NT} E_{ERM} + (1 - c_{NT}) E_{matrix}, \quad (10)$$

where  $c_{NT}$  is the nanotube volume fraction within the finite element cell and  $E_{matrix}$  is the matrix modulus. From (9) and (10),  $E_{ERM}$  of the embedded inclusion can be calculated as

$$E_{ERM} = \frac{E_{cell}^{FEA} (1 - c_{NT}) E_{matrix}}{c_{NT}}. \quad (11)$$

Thus  $E_{ERM}$  represents the modulus of a straight inclusion that, under identical loading conditions, would yield the same effective finite element cell response as that obtained with the wavy inclusion.

This finite element solution is a powerful tool to model the effective response of embedded wavy inclusions. While at first glance the number of parameters affecting  $E_{cell}^{FEA}$  (and hence  $E_{ERM}$ ) appears quite large, we will show later in this chapter that for the model described above, and an additional assumption that the Poisson ratios of the phases are equal,  $E_{ERM}$  will only be dependent on three parameters: the waviness ratio ( $w=a/\lambda$ ) and wavelength ratio ( $\lambda/d$ ) of the nanotube and the ratio of the phase moduli ( $E_{ratio}=E_{NT}/E_{matrix}$ ). A systematic analysis of the impact of these parameters on  $E_{ERM}$  was undertaken and the key results will be presented later in this chapter. The benefit of such an analysis is that it allows inclusion waviness to be integrated into traditional micromechanics techniques by simply modeling the wavy

inclusions as straight inclusions with a reduced reinforcing modulus  $E_{ERM}$  determined via finite element modeling.

### Analytical solution for $E_{cell}$

After the development of the finite element model presented above, it was brought to our attention that in certain circumstances the value for  $E_{cell}$  can be approximated using analytical expressions developed for the analysis of flexible fiber composites (Chou and Takahashi 1987; Kuo, Takahashi et al. 1988). Specifically, the effective Young's modulus for a composite with isophase sinusoidal fibers can be written as

$$E_x^* = \frac{(1+c)^{3/2}}{\frac{1}{E_f} + \frac{c}{2} S_{11} + \frac{3}{2} c \frac{1}{E_f} (1+c)^{3/2} S_{22} + \frac{c}{2} (2S_{12} + S_{66})} \quad (12)$$

where  $c = (2a/\lambda)^2$  and  $S_{ij}$  are the elastic compliance terms which relate longitudinal (L) and transverse (T) stresses and strains of the *unidirectional* straight fiber composite via

$$\begin{bmatrix} \epsilon_L \\ \epsilon_T \\ \epsilon_{LT} \end{bmatrix} = \begin{bmatrix} S_{11} & S_{12} & 0 \\ S_{12} & S_{22} & 0 \\ 0 & 0 & S_{66} \end{bmatrix} \begin{bmatrix} \sigma_L \\ \sigma_T \\ \sigma_{LT} \end{bmatrix} \quad (13)$$

The key aspect of the analysis is that a sufficiently small volume fraction of straight inclusion must be assumed in (13), such that the resulting elastic compliance terms approximate the dilute solution response modeled in the finite element analysis. Similar to the analysis using the finite element method, these terms will converge for a sufficiently small volume fraction of inclusions, which we found to be on the order of 0.01%.

Similar to the Analytical Long Wavelength (ALW) model presented later in this chapter, the analytical expressions above can be used to approximate  $E_{\text{cell}}$  from the finite element analysis when the wavelength ratio  $\lambda/d$  is sufficiently large for the case of a given waviness ratio  $a/\lambda$ . When  $a/\lambda$  is too large for a given wavelength ratio, the analytical solution underestimates the value of  $E_{\text{cell}}$  determined from the finite element analysis. For consistency, in the current work the values for  $E_{\text{cell}}$  were taken directly from the finite element simulations.

### **Convergence of $E_{\text{ERM}}$ for a sufficiently large matrix**

In order to eliminate the size of the finite element model as a parameter in the analysis, it is necessary to show that  $E_{\text{ERM}}$  converges for a sufficiently large matrix. To accomplish this we consider a finite element cell of an embedded wavy nanotube (see Figure 21), where for simplicity we redefine the length of the cell as  $L$  (to eliminate carrying a factor of two in our analysis below). We assume that the matrix

boundary at the top and bottom of the cells is sufficiently far from the nanotube such that fields at these boundaries are undisturbed by the presence of the nanotube, and denote the volumes of the NT, matrix, and total cell as  $V_{NT}$ ,  $V_{matrix}$ , and  $V$ , respectively. Note that a respective area is given as  $A=V/L$ . We apply an infinitesimally small uniform strain  $\epsilon_z$  in the fiber axial direction and measure the total resultant force  $F_{tot}$  necessary to cause this strain. From (10) and (11) we can write the effective reinforcing modulus for this particular finite element cell as

$$E_{ERM_1} = \frac{\frac{F_{tot} L}{V \epsilon_z} \left[ \frac{V_{mat}}{V} E_{mat} \right]}{\frac{V_{NT}}{V}} = \frac{F_{tot} L}{V_{NT} \epsilon_z} \left[ \frac{V_{mat}}{V_{NT}} E_{mat} \right]. \quad (14)$$

Now consider a second finite element geometry, identical to the previous cell except that additional matrix material, with a volume  $V_{matrix2}$ , has been evenly divided and added to the top and bottom of the first cell. Because of the size of the first cell, this additional matrix material is also unaffected by the presence of the wavy nanotube, thus the force necessary to produce a uniform strain  $\epsilon_z$  in this additional matrix material is simply  $F_2 = \frac{E_{mat} V_{mat2} \epsilon_z}{L}$ . The effective reinforcing modulus for the second finite element cell can be written as

$$E_{ERM_2} = \frac{\frac{(F_{tot} + F_2)L}{(V + V_{mat_2})} \square_z \frac{V_{mat} + V_{mat_2}}{V + V_{mat_2}} E_{mat}}{\frac{V_{NT}}{V + V_{mat_2}}} = \frac{(F_{tot} + F_2)L}{V_{NT} \square_z} \square \frac{V_{mat} + V_{mat_2}}{V_{NT}} E_{mat} \quad (15)$$

Substituting the expression for  $F_2$  into (15) yields  $E_{ERM1}=E_{ERM2}$ , and thus for a sufficiently large matrix the value of  $E_{ERM}$  is independent of the size of the finite element cell. For all simulations the finite element cell was created large enough such that this condition was satisfied; typically the nanotube volume fraction in the finite element cell was less than 0.05%.

### **Reduction of $E_{ERM}$ parameters for the finite element analysis**

Because we have shown that  $E_{ERM}$  converges given a sufficiently large finite element cell, it is sufficient to consider the model parameters that influence  $E_{cell}$  in the present analysis. Assuming isotropic behavior of the phase materials, the model at first appears to be dependent on seven parameters: the moduli ( $E_{NT}$  and  $E_{matrix}$ ) and Poisson ratios ( $\square_{NT}$  and  $\square_{matrix}$ ) of the phase materials, the wavelength and diameter of the NT ( $\square$  and  $d$ ), and the sinusoidal amplitude  $a$  such that

$$E_{cell} = f(E_{NT}, E_{matrix}, \square_{NT}, \square_{matrix}, a, d, \square). \quad (16)$$

To first simplify the analysis we assume that the Poisson ratios of the phases are identical and equal to 0.30, an assumption which we will discuss in further detail later in the text. Thus one can write (16) in a mathematically equivalent form as

$$g(E_{\text{cell}}, E_{\text{NT}}, E_{\text{matrix}}, a, d, \Pi) = 0, \quad (17)$$

where  $g$  is dependent on these six parameters but of an unknown functional form. Using the Buckingham Pi theorem (Fox and McDonald 1992), we can further rewrite (17) as

$$\Pi_1 = G_1(\Pi_2, \Pi_3, \Pi_4), \quad (18)$$

where  $\Pi_i$  are the dimensionless ratios

$$\begin{aligned} \Pi_1 &= E_{\text{NT}}^a \Pi^b E_{\text{cell}}, & \Pi_2 &= E_{\text{NT}}^c \Pi^d E_{\text{mat}} \\ \Pi_3 &= E_{\text{NT}}^e \Pi^f a, & \Pi_4 &= E_{\text{NT}}^g \Pi^h d \end{aligned} \quad (19)$$

The unknown superscript parameters  $a-h$  in (19) can be determined through dimensional analysis and substituted into (18) to yield

$$\frac{E_{\text{cell}}}{E_{\text{NT}}} = G_1 \left( \frac{E_{\text{NT}}}{E_{\text{mat}}}, \frac{a}{\Pi}, \frac{\Pi}{d} \right), \quad (20)$$

where  $G_1$  is a function of these parameters (only) and will be determined through our finite element study.

## **Micromechanical Modeling and the Mori-Tanaka Method**

We will illustrate how inclusion waviness can be incorporated into traditional micromechanical techniques by using the Mori-Tanaka method, a popular tool for the analysis of multi-phase materials (Mori and Tanaka 1973; Benveniste 1987; Weng 1990). The Mori-Tanaka method has been used by a wide range of researchers to model the effective behavior of composites, and allows the average stress fields and overall effective stiffness of a composite with a non-dilute concentration of inclusions to be determined. It has been used to study the effect of inclusion shape on composite moduli (Zhao and Weng 1990; Qui and Weng 1991) and the viscoelastic behavior of polymer-matrix composites (Brinson and Lin 1998; Fisher and Brinson 2001). Further, the Mori-Tanaka method has been extended to cover composites with multiple inclusion phases (Benveniste 1987; Weng 1990) and random orientations of inclusions (Tandon and Weng 1986; Weng 1990).

Specifically we are interested in the Mori-Tanaka solution for an  $N$  phase composite, where each inclusion phase is randomly orientated in two or three dimensional space. For the following derivation we first consider the case where the inclusions are unidirectionally aligned within the matrix. Once the necessary parameters have been determined for this case, appropriate tensor transformations and

volume averaging procedures will be introduced to account for the different inclusion orientations. This technique is described in more detail below.

### ***Mori-Tanaka method for unidirectionally-aligned inclusions***

We assume that the composite is comprised of  $N$  phases; the matrix will be denoted as phase  $0$  with a corresponding stiffness  $C_0$  and volume fraction  $f_0$ , while an arbitrary  $r$ th inclusion phase (where  $r=1$  to  $N-1$ ) has a stiffness of  $C_r$  and a volume fraction  $f_r$ . Each phase is assumed to be linearly elastic and isotropic, and perfect bonding between the inclusions and the matrix is assumed. The inclusions are further assumed to be ellipsoidal with a circular cross-section ( $a_1=a_2$ ), an aspect ratio  $\square_r$  (ratio of length to diameter), and aligned along the 3-axis (as shown in Figure 22).

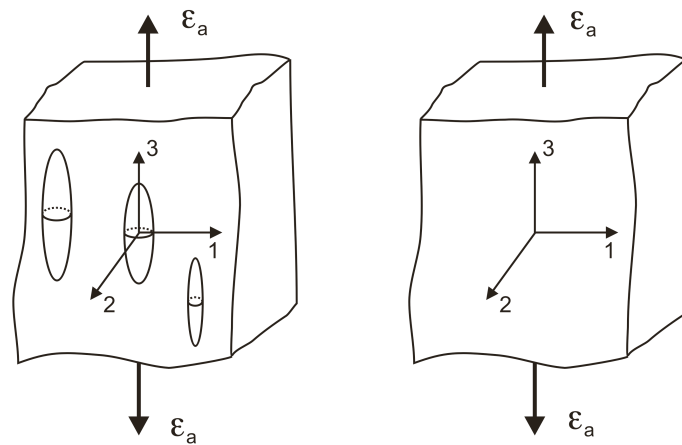


**Figure 22. Schematic of Mori-Tanaka method. (left) Multiphase composite material. (right) Comparison material.**

Consider the two models shown in Figure 22, representing the composite model and a “comparison material” with properties identical to those of the matrix. Unless required, explicit tensor notation will be omitted for clarity. Displacements are now prescribed on the boundary of each material to give rise to a uniform strain  $\epsilon_a$  in each material. The stresses required to produced this uniform strain in each material are

$$\bar{\sigma} = C\epsilon_a, \quad \bar{\sigma}_0 = C_0\epsilon_a \quad (21)$$

where  $\bar{\sigma}$  and  $\bar{\sigma}_0$  are the average stress of the composite and comparison materials, respectively.

The strain field within the matrix material of the composite will not be uniform due the presence of the inclusions (and hence the average matrix strain  $\bar{\epsilon}_b$  will not equal  $\epsilon_a$ ), but rather will be perturbed by an amount  $\bar{\epsilon}_b^{pt}$  such that

$$\bar{\epsilon}_b = \epsilon_a + \bar{\epsilon}_b^{pt}, \quad (22)$$

where an overscore represents the volume average of the stated quantity. The average strain in the  $r$ th inclusion is further perturbed from that of the matrix,

$$\bar{\epsilon}_r = \bar{\epsilon}_b + \bar{\epsilon}_r^{pt}. \quad (23)$$

Given that the average stress in each phase is given as  $\bar{\sigma}_r = C_r \bar{\epsilon}_r$ , using the equivalent inclusion method one can show that the average stress in the  $r$ th inclusion can be written in terms of the matrix stiffness,

$$\bar{\sigma}_r = C_r \bar{\epsilon}_r = C_0 \left( \bar{\epsilon}_r + \bar{\epsilon}_r^* \right), \quad (24)$$

where  $\bar{\epsilon}_r^*$  is the fictitious eigenstrain of the  $r$ th inclusion. For a single ellipsoidal inclusion in an infinite matrix, Eshelby showed that the eigenstrain and perturbed strain of the  $r$ th inclusion can be related via

$$\bar{\epsilon}_r^{pt} = S_r \bar{\epsilon}_r^*, \quad (25)$$

where  $S_r$  is the Eshelby tensor. General forms of the Eshelby tensor are provided in the Appendix.

Solving for  $\bar{\epsilon}_r^*$  in (24) and then substituting into (23) using (25), one can find the dilute strain-concentration factor of the  $r$ th phase,  $A_r^{dil}$ , which relates the average strain in the  $r$ th inclusion to the average strain in the matrix, such that

$$\bar{\epsilon}_r = A_r^{dil} \bar{\epsilon}_0, \quad (26)$$

where

$$A_r^{\text{dil}} = \left[ \mathbf{I} + S_r C_0^{-1} (C_r - C_0) \right]^{-1} \quad (27)$$

and  $\mathbf{I}$  is the fourth order identity tensor. We further require that the volume-weighted average phase strains must equal the far-field applied strain, such that

$$f_0 \bar{\boldsymbol{\epsilon}} + \sum_{r=1}^{N_{\text{I}}} f_r \boldsymbol{\epsilon}_r = \bar{\boldsymbol{\epsilon}}. \quad (28)$$

Given (28), we can now define the strain-concentration factor  $A_0$ , which accounts for inclusion interaction by relating the average matrix strain in the composite to the uniform applied strain,

$$\bar{\boldsymbol{\epsilon}} = A_0 \bar{\boldsymbol{\epsilon}}, \quad (29)$$

where

$$A_0 = f_0 \mathbf{I} + \sum_{r=1}^{N_{\text{I}}} f_r A_r^{\text{dil}}. \quad (30)$$

The key assumption of the Mori-Tanaka method is that the far-field strain that each inclusion “feels” is the unknown average matrix strain. This can be expressed as

$$\boldsymbol{\epsilon}_r = A_r^{\text{dil}} \bar{\boldsymbol{\epsilon}}, \quad (31)$$

which in conjunction with (29) gives the strain-concentration factor  $A_r$  for the  $r$ th inclusion phase in the *non-dilute composite* as

$$A_r = A_r^{\text{dil}} A_0. \quad (32)$$

To find the effective stiffness  $C$  for a unidirectionally aligned composite, we require that the average stress  $\bar{\sigma}$  of the composite be equal to the sum of the weighted average stresses in each phase,

$$\bar{\sigma} = f_0 \sigma_0 + \sum_{r=1}^{N-1} f_r \sigma_r = C \bar{\epsilon}. \quad (33)$$

Through straightforward substitution and manipulation, the effective stiffness of the unidirectionally aligned composite is found to be

$$C = f_0 C_0 A_0 + \sum_{r=1}^{N-1} f_r C_r A_r. \quad (34)$$

For purposes of the next section it will be useful to express (34) in a slightly different form. Recalling (28) and (33), we can write

$$C = \begin{bmatrix} \sigma \\ \tau \end{bmatrix} = f_0 \begin{bmatrix} C_0 \\ \tau_0 \end{bmatrix} + \sum_{r=1}^{N-1} f_r \begin{bmatrix} C_r \\ \tau_r \end{bmatrix} A_r^{\text{dil}} = \begin{bmatrix} \sigma \\ \tau \end{bmatrix} = f_0 \begin{bmatrix} C_0 \\ \tau_0 \end{bmatrix} I + \sum_{r=1}^{N-1} f_r \begin{bmatrix} C_r \\ \tau_r \end{bmatrix} A_r^{\text{dil}}, \quad (35)$$

which is a form prevalent in the literature (see (Weng 1990)).<sup>4</sup> Both (34) and (35) thus provide the effective stiffness of a multiphase composite with aligned inclusions. However, in order to account for random orientations of the inclusion phases, the analysis must be extended as discussed below.

### ***Mori-Tanaka method for randomly aligned inclusions***

When the inclusion phases are randomly orientated in the matrix, determination of the effective composite stiffness can be accomplished by taking the orientational averages of appropriate quantities (Weng 1990). In this case the strain consistency condition in (28) can be written as

$$\begin{bmatrix} \sigma \\ \tau \end{bmatrix} = f_0 \mathbf{I} + \sum_{r=1}^{N-1} f_r \left\{ A_r^{\text{dil}} \right\} \begin{bmatrix} \sigma \\ \tau \end{bmatrix} = \langle \sigma_a \rangle \quad (36)$$

where brackets  $\{ \}$  represent the average of a quantity over all possible orientations.<sup>5</sup> Due to this averaging process, the average strain in the matrix will be different from that in the unidirectional composite due to the random alignment of inclusions.

---

<sup>4</sup> Weng further simplifies this expression using the relationship that  $A_0^{\text{dil}} = \mathbf{I}$ . Such an expression is sensible given that by definition  $A_0$  relates the average strain in the matrix to the uniform applied strain. In the dilute sense these strains will be equal.

<sup>5</sup> Note that the derivation for unidirectional inclusions presented in the last section is a subset of the more general derivation presented here.

Similarly one can rewrite (33) for the case of randomly orientated inclusions (with the understanding that the matrix stress and strain are orientation-independent due to the isotropy of the matrix) as

$$\bar{\epsilon} = f_0 \epsilon_0 + \sum_{r=1}^{N-1} f_r \{\epsilon_r\} = C \epsilon_h. \quad (37)$$

This expression can be simplified using the relationships established in the preceding section. Briefly,

$$\begin{aligned} \bar{\epsilon} &= f_0 C_0 \epsilon_b + \sum_{r=1}^{N-1} f_r \{C_r \epsilon_r\} \\ &= f_0 C_0 \epsilon_b + \sum_{r=1}^{N-1} f_r \{C_r A_r^{dil}\} \epsilon_b \\ &= \begin{bmatrix} \epsilon_b \\ \epsilon_b \\ \epsilon_b \end{bmatrix} f_0 C_0 + \sum_{r=1}^{N-1} f_r \{C_r A_r^{dil}\} \begin{bmatrix} \epsilon_b \\ \epsilon_b \\ \epsilon_b \end{bmatrix} = C \epsilon_h \end{aligned} \quad (38)$$

From (36) and (38), the effective stiffness of a composite with randomly orientated inclusions can be written as

$$C = \begin{bmatrix} \epsilon_b \\ \epsilon_b \\ \epsilon_b \end{bmatrix} f_0 C_0 + \sum_{r=1}^{N-1} f_r \{C_r A_r^{dil}\} \begin{bmatrix} \epsilon_b \\ \epsilon_b \\ \epsilon_b \end{bmatrix} f_0 I + \sum_{r=1}^{N-1} f_r \{A_r^{dil}\} \begin{bmatrix} \epsilon_b \\ \epsilon_b \\ \epsilon_b \end{bmatrix}, \quad (39)$$

which is the direct analog of (35) except that appropriate averaging is used here to account for the inclusion orientation. Later in this chapter we will discuss how these orientational averages can be determined.

### **Euler angles and tensor transformations**

To determine the effective properties of a composite with randomly orientated inclusions, it will be necessary to calculate various orientational averages as outlined in the previous section. We will assume that the local axes of the fiber are denoted  $x'_1$ ,  $x'_2$ , and  $x'_3$  (where  $x'_3$  is the inclusion axis), and the global (or fixed) composite coordinates are  $X_1$ ,  $X_2$ , and  $X_3$  (see Figure 23). Our goal is to develop the transformation matrix  $a_{ij}$  which maps vector  $v'_j$  in the local coordinate system to coordinates  $v_i$  in the global coordinate system via

$$v_i = a_{ij} v'_j. \quad (40)$$

Note that in general it is necessary to specify three Euler angles to describe the inclusion orientation; however, because the inclusion is assumed to be spheroidal it is only necessary to specify  $\theta$  and  $\phi$  in Figure 23 to completely describe the orientation of the fiber.

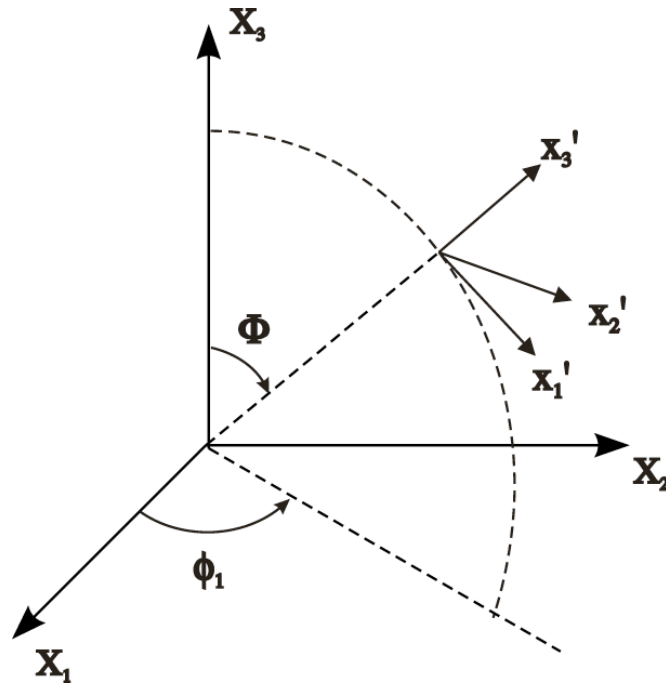


**Figure 23. Relationship between the local and global coordinate systems.**

Following Roe's specification for Euler angles (Randle 1992), the local coordinate system is obtained by a rotation of  $\phi_1$  about the  $X_3$  axis, followed by a rotation of  $\phi$  about the resulting  $x_2'$  axis. These rotations can be described using the appropriate coordinate transformations that map *local* vectors to *global* vectors (i.e. where  $X_i = R_{ij} x_j'$ )

$$R(\phi_1) = \begin{bmatrix} \cos(\phi_1) & \sin(\phi_1) & 0 \\ \sin(\phi_1) & \cos(\phi_1) & 0 \\ 0 & 0 & 1 \end{bmatrix}, \quad R(\phi) = \begin{bmatrix} \cos(\phi) & 0 & \sin(\phi) \\ 0 & 1 & 0 \\ \sin(\phi) & 0 & \cos(\phi) \end{bmatrix}. \quad (41)$$

Consecutive rotations of  $\alpha_1$  and  $\alpha$  thus result in the following transformation between local and global coordinates:

$$\begin{bmatrix} X_1 \\ X_2 \\ X_3 \end{bmatrix} = R(\alpha_1)R(\alpha) \begin{bmatrix} x_1 \\ x_2 \\ x_3 \end{bmatrix} = \begin{bmatrix} mp & n & mq \\ np & m & nq \\ q & 0 & p \end{bmatrix} \begin{bmatrix} x_1 \\ x_2 \\ x_3 \end{bmatrix} = a_{ij}^{3D} x_j \quad (42)$$

where  $m = \cos(\alpha_1)$ ,  $n = \sin(\alpha_1)$ ,  $p = \cos(\alpha)$ ,  $q = \sin(\alpha)$ , and  $a_{ij}^{3D}$  represents the transformation matrix describing transformations in full three-dimensional space. If the inclusions are restricted to lie in the 1-2 plane, the appropriate 2D transformation matrix  $a_{ij}^{2D}$  can be found by setting  $\alpha = \pi/2$  (see Figure 23), such that

$$a_{ij}^{2D} = \begin{bmatrix} 0 & \sin \alpha_1 & \cos \alpha_1 \\ 0 & \cos \alpha_1 & \sin \alpha_1 \\ 1 & 0 & 0 \end{bmatrix}. \quad (43)$$

Higher order tensor transformations are accomplished through the usual tensor transformation laws. Thus the transformation of a fourth-order stiffness tensor  $B_{ijkl}$  from local to global coordinates can be written as

$$B_{ijkl}(\alpha_1, \alpha) = a_{ir} a_{js} a_{kt} a_{lu} B'_{rstu}, \quad (44)$$

where the angular dependence of the  $a_{ij}$  terms is implied and the standard convention that double indices implies summation is used.<sup>6</sup> To further illustrate (44), we write out the  $B_{1111}$  terms below:

$$B_{1111}(\square_1, \square) = a_{11}^4 B'_{1111} + a_{12}^4 B'_{2222} + a_{13}^4 B'_{3333} + (2B'_{1122} + 4B'_{1212}) a_{11}^2 a_{12}^2 + (2B'_{1133} + 4B'_{1313}) a_{11}^2 a_{13}^2 + (2B'_{2233} + 4B'_{2323}) a_{12}^2 a_{13}^2, \quad (45)$$

where it is assumed that particular symmetry conditions ( $B_{rstu}=B_{turs}$  and  $B_{rstu}=B_{rsut}=B_{srut}=B_{srtu}$ ) hold in the local coordinate system. When these symmetry conditions do not hold (such as for the dilute strain concentration tensor  $A_r^{\text{dil}}$  in the previous section) the procedure is identical, although the collection of terms such as that in (45) is more tedious.

Given (44), the orientational average of a fourth tensor in random 3D space is

$$\{B_{ijkl}\} = \frac{1}{2\pi} \int_0^\pi \int_0^{2\pi} B_{ijkl}(\square_1, \square) \sin(\square) d\square d\square_1 \quad (46)$$

where the transformation matrix for three dimensional space  $a_{ij}^{3D}$  is used in (44) and the  $\sin(\square)$  term accounts for the surface area of a sphere. For a 3D random orientation

---

<sup>6</sup> We stress that the transformation in (44) is a *tensor* transformation, and as such is only applicable to tensor quantities. Quantities which are not of tensorial form, specifically tensors expressed using contracted notation, must first be converted to their appropriate tensorial components before such a transformation is valid.



$$\begin{aligned}
\{B_{11}\} = \{B_{22}\} &= \frac{1}{8} [3B_{22} + 3B_{33} + B_{23} + B_{32} + 4B_{44}] \\
\{B_{33}\} &= B_{11} \\
\{B_{12}\} = \{B_{21}\} &= \frac{1}{8} [B_{22} + B_{33} + 3B_{23} + 3B_{32} - 4B_{44}] \\
\{B_{13}\} = \{B_{23}\} &= \frac{1}{2} [B_{21} + B_{31}] \\
\{B_{31}\} = \{B_{32}\} &= \frac{1}{2} [B_{12} + B_{13}] \\
\{B_{44}\} = \{B_{55}\} &= \frac{1}{2} [B_{55} + B_{66}] \\
\{B_{66}\} &= \frac{1}{8} [B_{22} + B_{33} - B_{23} - B_{32} + 4B_{44}]
\end{aligned} \tag{49}$$

### A note on symmetry

Writing the constitutive stress-strain relationship  $\sigma_{ij} = C_{ijkl} \epsilon_{kl}$  in tensor form suggests that it would require 81 constants to characterize the stress-strain response of a material (i.e there are 81 independent  $C_{ijkl}$  tensor components). However, the condition that the stress and strain tensors are symmetric reduces the number of independent constants to 36; this allows the use of contracted notation that is commonplace in composites research (see the Appendix). The number of independent constants is further reduced based on arguments related to the work per unit volume of the system, from which one can prove that the stiffness (compliance) tensor must be symmetric, such that  $C_{ijkl} = C_{klij}$ . This condition further reduces the number of independent constants to 21. The number of independent constants can be further

reduced based on assumptions of the material behavior (i.e. it can be shown that transversely isotropic materials have 5 independent constants, and that isotropic materials have two independent constants).

One inconsistency with the implementation of the Mori-Tanaka method for multiphase materials is that it may yield non-symmetric stiffness (and compliance) tensors, thus violating the symmetry conditions required for a *real* material (Benveniste, Dvorak et al. 1991; Li 1999; Schjodt-Thomsen and Pyrz 2001). This non-symmetry is a result of the non-symmetric strain concentration tensors  $A_r^{\text{dil}}$  calculated in (27). This difficulty has been attributed to the extension of the Mori-Tanaka scheme, originally developed for two-phase materials, to multiphase composites (Li 1999).

To illustrate, we calculate the effective stiffness of a three-phase composite composed of isotropic phase materials. Here we consider cylindrical inclusions with an aspect ratio  $\square=L/d=1000$ , randomly orientated in the 1-2 plane with volume fractions  $f_0=0.50$  and  $f_1=f_2=0.25$ , phase moduli  $E_0=1$ ,  $E_1=50$ , and  $E_2=200$ , and Poisson ratios  $\square_i=0.30$ , where the matrix phase is denoted as phase  $0$ . Using the Mori-Tanaka method, the effective stiffness of the system can be calculated as

$$L_{2D} = \begin{bmatrix} 36.764 & 12.214 & 1.350 & 0 & 0 & 0 \\ 12.214 & 36.764 & 1.350 & 0 & 0 & 0 \\ 1.342 & 1.342 & 3.222 & 0 & 0 & 0 \\ 0 & 0 & 0 & 1.039 & 0 & 0 \\ 0 & 0 & 0 & 0 & 1.039 & 0 \\ 0 & 0 & 0 & 0 & 0 & 12.275 \end{bmatrix} \quad (50)$$

where the non-symmetry of stiffness tensor ( $L_{13}=L_{23} \neq L_{31}=L_{32}$ ) is evident (see also Schjodt-Thomsen and Pyrz (2001) for additional examples). Such an example is only given to illustrate the non-symmetry of the stiffness tensor; the extent of non-symmetry is closely related to the properties and geometries of the phases in a particular system. It is worth noting the following conditions, under which the Mori-Tanaka method is guaranteed to yield a symmetric stiffness (Schjodt-Thomsen and Pyrz 2001):

- Two-phase composites
- Multiphase composites with aligned inclusions
- Multiphase composites with randomly aligned spherical inclusions

In addition, in our numerical studies we have found that the Mori-Tanaka solution for a multiphase composite with similarly shaped inclusions randomly orientated in three-dimensional space has in every case yielded a symmetric (and isotropic) stiffness; however, a proof of this condition is beyond the scope of this dissertation.

One of the manners in which the symmetry of the effective stiffness can be guaranteed is by normalizing the concentration tensors (see Schjodt-Thomsen and Pyrz (2001) and references therein). However, because here we are primarily interested in the effective moduli predictions (rather than the stiffness tensor), one can show that the effect of this non-symmetry is minimal. Specifically, later in this chapter we show that the effective moduli are only dependent on the product of the  $C_{13}$  and  $C_{31}$  terms, independent of the symmetry (or lack thereof) of the stiffness tensor. Thus symmetry of the stiffness tensor was enforced *after* the Mori-Tanaka calculation by setting

$$C_{13} = C_{23} = C_{31} = C_{32} = \sqrt{C_{13} C_{31}}. \quad (51)$$

Such manipulation will have no affect on the Mori-Tanaka predictions for  $E_{11}$ ,  $E_{33}$ ,  $\nu_{12}$ , or  $\nu_{13}$ .

### **An alternate model for randomly orientated inclusions**

An alternative method has been proposed in the literature to determine the effective moduli of composites containing randomly orientated inclusions using the Mori-Tanaka method (Huang 2001). This alternative model will be referred to as the Huang model, to distinguish it from the Weng model described earlier. In the Huang model, the effective stiffness for a multiphase composite is found by taking the

orientational average of the effective modulus for the unidirectional composite case (i.e. equation (35)), rather than the orientational averaging of the individual components as outlined in (39) for the Weng model.

The Huang model is inviting because it allows explicit expressions for composites with randomly oriented inclusions to be given in terms of the unidirectional composite stiffness components. However, there is a critical difference between these models. For the Weng model, the introduction of the orientational averaging of field quantities is effectively introduced *before* the determination of the unknown average matrix strain that is fundamental to the Mori-Tanaka approach. For the Huang model, the unknown matrix strain is solely determined from the analysis of the unidirectional composite model, and thus is not dependent on the type of randomness that the inclusions might exhibit. Thus the Huang model does not properly model a multiphase composite with randomly orientated inclusions, but rather models a composite within which individual domains of aligned inclusions are present. As shown in Figure 24, for the Huang model the inclusion orientations are random in the sense that these smaller domains of aligned inclusions are of different orientations within the global material.

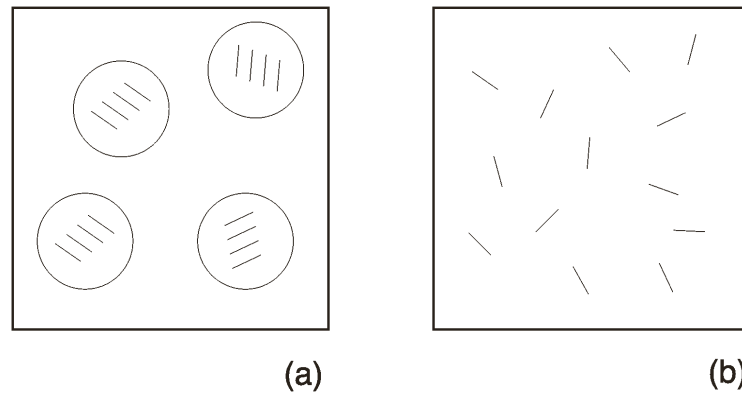


**Figure 24. Models to account for randomness of inclusion orientation. (a) Huang model. (b) Weng model.**

For small volume fractions of inclusions, and when the properties of the inclusions are not vastly different than those of the matrix, results from the two models are somewhat similar. However, this difference becomes significant as the volume fractions of inclusions increase, due to the difference between the two models in the determination of the average matrix strain of the composite. (We note that in the case of 2D random orientations the out-of-plane predictions from each model are in excellent agreement.) To illustrate the difference in moduli predictions between the two methods, the results for a three-phase composite consisting of isotropic phase constituents, with equal volume fractions of inclusion phases (i.e.  $f_1=f_2$ ), are presented in Table 6. Here we see that the effective moduli found using the Huang model are *less* than those found from the (correct) Weng Mori-Tanaka implementation, because the Huang model overestimates the average matrix strain, leading to a model of

material behavior that is too compliant. Because the Weng model correctly accounts for inclusion orientation in its determination of the effective composite stiffness, all subsequent work utilizing the Mori-Tanaka method will use the Weng model, i.e. equation (39), for the determination of the effective composite properties.

		Weng model		Huang model	
		$f_0=0.9$	$f_0=0.6$	$f_0=0.9$	$f_0=0.6$
3D random orientation	E	10.99	55.74	10.19	38.13
	$\nu$	4.37	22.19	4.06	15.23
	$\nu$	0.256	0.256	0.256	0.252
2D random orientation	$E_{11}=E_{22}$	20.44	99.80	19.18	74.15
	$E_{33}$	1.53	2.61	1.53	2.60
	$\nu_{12}$	7.68	37.62	7.21	27.85
	$\nu_{13}=\nu_{23}$	0.46	0.83	0.46	0.83
	k	15.53	74.56	14.61	55.91

**Table 6. Comparison of Huang and Weng models for effective moduli of multiphase composites with randomly orientated inclusions. ( $f_1=f_2$ ,  $E_0=1$ ,  $E_1=100$ ,  $E_2=1000$ ,  $\nu_1=\nu_2=L/d=1000$ , and  $\nu_3=0.30$ )**

### Simplification for a two-phase system

While the above formulations are concerned with the effective properties of multiphase composite materials, analytical expressions have been derived for the Mori-Tanaka solution for two-phase composites with 2D and 3D randomly orientated

inclusions (Tandon and Weng 1986). The expressions are quite unwieldy and thus not repeated here. It has been verified numerically that the Weng multiphase composite model used in this work matches the results of the analytical expressions for two-phase composites.

***Determination of the effective engineering constants***

Keeping in mind the preceding arguments that require a contracted stiffness tensor for a *real* material to be symmetric, the stress-strain relationship for a transversely isotropic material with a 1-2 plane of isotropy can be written as

$$\begin{matrix} \square_1 \\ \square_2 \\ \square_3 \\ \square_4 \\ \square_5 \\ \square_6 \end{matrix} = \begin{bmatrix} C_{11} & C_{12} & C_{13} & 0 & 0 & 0 \\ C_{12} & C_{11} & C_{13} & 0 & 0 & 0 \\ C_{31} & C_{31} & C_{33} & 0 & 0 & 0 \\ 0 & 0 & 0 & C_{44} & 0 & 0 \\ 0 & 0 & 0 & 0 & C_{44} & 0 \\ 0 & 0 & 0 & 0 & 0 & \frac{C_{11} - C_{12}}{2} \end{bmatrix} \begin{matrix} \square_1 \\ \square_2 \\ \square_3 \\ \square_4 \\ \square_5 \\ \square_6 \end{matrix} \tag{52}$$

where the tensorial shear strains  $\square$  are related to the engineering shear strains  $\square$  via  $\square_4 = \square_{23} = 2\square_{23}$ ,  $\square_5 = \square_{13} = 2\square_{13}$ , and  $\square_6 = \square_{12} = 2\square_{12}$ . For completeness, a more detailed description of contracted notation is provided in the Appendix. The contracted stiffness for a composite with inclusions aligned along the 3-axis, as well as composites with inclusions randomly orientated in the 1-2 plane, will show such a

form. For the case of inclusions randomly orientated in three-dimensional space, the stiffness will be fully isotropic such that the additional relations  $C_{11}=C_{33}$ ,  $C_{12}=C_{13}=C_{31}=C_{32}$ , and  $C_{44}=\frac{1}{2}(C_{11} - C_{12})$  in (52) will be satisfied.

The compliance tensor  $S$  (where  $\square=S\square$ ) is defined as the inverse of the stiffness tensor, and can be written in terms of the stiffness components  $C_{ij}$  as

$$S = \begin{pmatrix} \frac{C_{11}C_{33} - C_{13}C_{31}}{\square_1} & \frac{C_{12}C_{33} - C_{13}C_{31}}{\square_1} & \frac{C_{13}}{\square_2} & 0 & 0 & 0 \\ \frac{C_{12}C_{33} - C_{13}C_{31}}{\square_1} & \frac{C_{11}C_{33} - C_{13}C_{31}}{\square_1} & \frac{C_{13}}{\square_2} & 0 & 0 & 0 \\ \frac{C_{13}}{\square_2} & \frac{C_{13}}{\square_2} & \frac{C_{11} + C_{12}}{\square_2} & 0 & 0 & 0 \\ 0 & 0 & 0 & \frac{1}{C_{44}} & 0 & 0 \\ 0 & 0 & 0 & 0 & \frac{1}{C_{44}} & 0 \\ 0 & 0 & 0 & 0 & 0 & \frac{2}{C_{11} - C_{12}} \end{pmatrix} \quad (53)$$

where

$$\begin{aligned} \square_1 &= C_{33}(C_{11}^2 - C_{12}^2) - 2C_{13}C_{31}(C_{11} - C_{12}) \\ \square_2 &= C_{33}(C_{11} + C_{12}) - 2C_{13}C_{31} \end{aligned} \quad (54)$$

From (52)-(54), we see that the procedure of using the geometric mean of  $C_{13}$  and  $C_{31}$  given in (51) to enforce the symmetry of the Mori-Tanaka effective stiffness will only affect the  $S_{13}=S_{23}=S_{31}=S_{31}$  compliance components. While such changes will alter the

exact value of some of the engineering constants, for our purposes the Young's and shear moduli with which we are most interested will not be affected by such a scheme. We note that the compliance tensor will have the same level of symmetry as that of the stiffness tensor.

Once the stiffness and compliance tensors are known, the components of these tensors can be used to calculate the engineering constants of the material. For an isotropic material two independent constants are required to describe the material response, for example the Young's modulus  $E$  and the shear modulus  $\mu$ . These can be determined from the known stiffness (or compliance) terms via

$$\begin{aligned} E = E_{11} = E_{22} = E_{33} &= \frac{1}{S_{11}} = \frac{\nu_1}{C_{11}C_{33} - C_{13}C_{31}} \\ \mu = \mu_{44} = \mu_{55} = \mu_{66} &= \frac{1}{S_{44}} = C_{44} \end{aligned} \quad (55)$$

For a transversely isotropic material five independent constants are required to fully characterize the material response. For a transversely isotropic material with a 1-2 plane of isotropy, five such constants are the transverse modulus  $E_{11}=E_{22}$ , the longitudinal modulus  $E_{33}$ , the axial shear modulus  $\mu_{44}=\mu_{55}$ , the transverse shear modulus  $\mu_{66}$ , and the plane strain bulk modulus  $k$ , which can be determined from the known stiffness or compliance terms such that

$$\begin{aligned}
E_{11} = E_{22} &= \frac{1}{S_{11}} = \frac{\nu_1}{C_{11}C_{33} - C_{13}C_{31}} \\
E_{33} &= \frac{1}{S_{33}} = \frac{\nu_2}{C_{11} + C_{12}} \\
\nu_{44} = \nu_{55} &= \frac{1}{S_{44}} = C_{44} \\
\nu_{66} &= \frac{1}{S_{66}} = \frac{2}{C_{11} - C_{12}} \\
k &= \frac{C_{11} + C_{12}}{2}
\end{aligned} \tag{56}$$

Relationships to obtain alternative elastic constants are given in the Appendix.

## Discretization of nanotubes based on waviness

To model the nanotube-reinforced polymer we partition the nanotube inclusions into distinct phases, based on their embedded waviness, and treat the problem as that of a multiphase composite. Each nanotube phase is then assigned a distinct effective reinforcing modulus  $E_{ERM}$  based on the average waviness of the phase and the results of the preceding finite element analysis. In practice, such a solution could be developed by imaging a representative portion of the NRP and developing an appropriate waviness distribution function characterizing the magnitude and extent of the nanotube waviness, leading to an appropriate multiphase composite model (see Figure 25 and Figure 26). This waviness distribution, along with the spatial

orientation of the NTs, can be used within an appropriate micromechanical method to provide a refined estimate of the effective moduli of a nanotube-reinforced polymer. This procedure is demonstrated in the next section using the Mori-Tanaka method for 2D and 3D randomly orientated inclusions assuming a given distribution of nanotube waviness.

Before we begin our analysis, it is insightful to estimate the range of values that may be characteristic of the waviness and wavelength ratios associated with the wavy geometry of embedded nanotubes. For illustrative purposes, Figure 25 shows an image of an NRP with different wavy nanotubes marked by solid lines, with approximate values for  $a/\lambda$  and  $\lambda/d$  given in the inset. Several nanotubes in Figure 25 are approximately straight (and not identified in the inset), while others show kinks and bends which, while not of the sinusoidal shape assumed in the model, will similarly limit the effective reinforcement of those nanotubes. We note that waviness perpendicular to the plane of the TEM image is masked, and that NT straightening during the preparation of the TEM sample may have occurred. Thus the waviness parameters shown in Figure 25 are to be seen as *illustrative* only, and will be influenced by the NRP system and the processing conditions of a particular sample. While a more thorough procedure to determine the embedded nanotube waviness may be warranted, for the purposes of this paper a hypothetical waviness distribution is sufficient to show the effect of nanotube waviness on the effective modulus of an

NRP. As our earlier analysis indicated, even for moderate nanotube waviness the decrease in effective reinforcement can be appreciable.

A critical step in the analysis is the determination of the dilute strain-concentration tensor  $A_r^{\text{dil}}$  relating the average strain of the  $r$ th inclusion to that of the matrix. In the present analysis  $A_r^{\text{dil}}$  is found via (27), where the stiffness tensor(s) of the inclusion phase(s)  $C_r$  are assumed to be isotropic with moduli  $E_{\text{ERM}}$  (based on the finite element modeling described earlier) and the Poisson ratio of the straight inclusion. The Eshelby tensors  $S_r$  are calculated assuming infinitely long cylindrical inclusions. Thus to account for the waviness of a particular inclusion we first find  $E_{\text{ERM}}$ , based on the embedded geometry and other applicable parameters, via a finite element analysis. We then treat the wavy inclusion as a straight inclusion but with an adjusted stiffness tensor to account for the wavy geometry. In related work discussed in the next section, we show that  $A_r^{\text{dil}}$  can be computed *directly* from an appropriate finite element analysis (Bradshaw, Fisher et al. 2002); in either case once  $A_r^{\text{dil}}$  has been determined the implementation of the Mori-Tanaka solution remains unchanged.

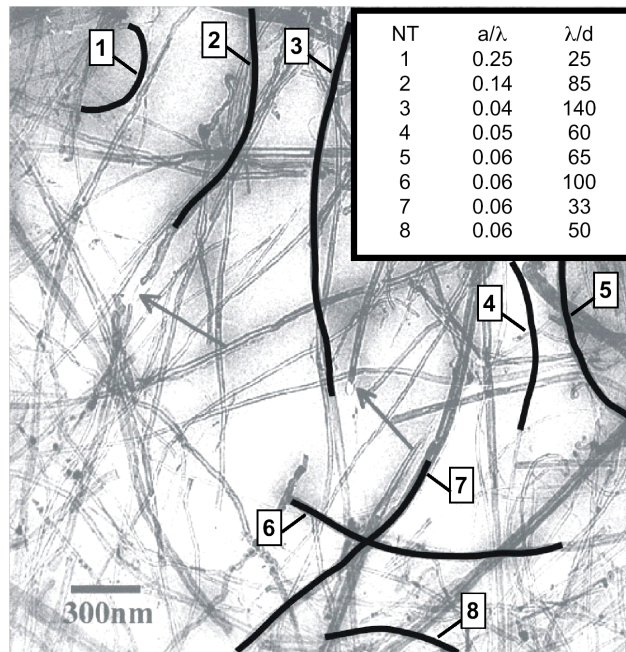


**Figure 25. Illustrative example of nanotube waviness. (Image from (Qian, Dickey et al. 2000)). (inset) Approximate values for the parameters  $w=a/\lambda$  and  $\lambda/d$  for the highlighted nanotubes.**

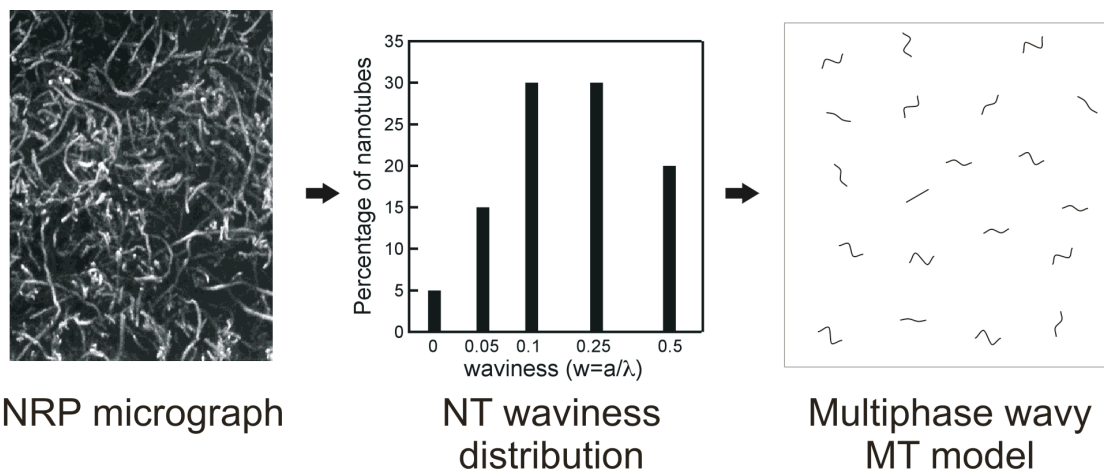


**Figure 26. Model of an NRP using a multiphase composite analysis with a known waviness distribution function.**

Our results suggest that modeling the NTs as straight inclusions (i.e. neglecting the curvature of the embedded geometry) is a simplification that will severely overestimate the reinforcement that the NTs provide the polymer. While the procedure here is demonstrated using  $E_{ERM}$  calculations based on finite element results, alternative means to evaluate  $E_{ERM}$ , such as molecular dynamics or related methods (Odegard, Gates et al. 2001a), could also be used in a similar analysis. Adaptations of the current model to include such effects as inter-layer (MWNTs) and inter-tube (NT bundles) sliding, as well as imperfect bonding between the nanotubes and the polymer, while not addressed here could also be developed.

## Results

The objective of this work is to develop a method to incorporate the typically observed waviness of embedded nanotubes into standard micromechanics techniques. Because the nanotube has been modeled as a continuum, the method is also in general applicable to other types of inclusions that may exhibit similar embedded geometries. We note that  $E_{ERM}$  will be less than (or equal to) the true NT modulus due to its waviness, and that a distribution of NT waviness within the material is likely. Thus rather than treat the NRP as a two-phase (nanotube/polymer) composite, we have developed a multiphase composite model where the NTs are partitioned into distinct

phases, with each NT phase assigned a characteristic  $E_{ERM}$  based on their embedded waviness.

With this in mind, the remainder of this section is divided into two parts. In the first part we discuss the impact of nanotube waviness and other model parameters on  $E_{ERM}$ . We will then use the results of the  $E_{ERM}$  analysis to compare the predictions of our micromechanical analysis, accounting for the embedded nanotube geometry, with results obtained assuming straight nanotube inclusions and with published experimental data for NRP effective modulus.

### ***Effective reinforcing modulus $E_{ERM}$***

As discussed previously, we have shown that the model for  $E_{ERM}$  is a function of three parameters: the waviness ( $w=a/\lambda$ ) and wavelength ratio ( $\lambda/d$ ) of the nanotube and the ratio of the phase moduli ( $E_{ratio}=E_{NT}/E_{matrix}$ ). Figure 27 shows  $E_{ERM}$  as a function of waviness for several different values of  $E_{ratio}$  and a wavelength ratio of 100. For all simulations a matrix modulus of 1 GPa was used. As expected, for zero waviness we obtain the straight nanotube results  $E_{ERM}=E_{NT}$ . We note that  $E_{ERM}$  is strongly dependent on the waviness and quickly decreases with increasing nanotube curvature. This drop in  $E_{ERM}$  is less pronounced for smaller  $E_{ratio}$  values because the mechanical constraint of the surrounding matrix material in this case is more significant.

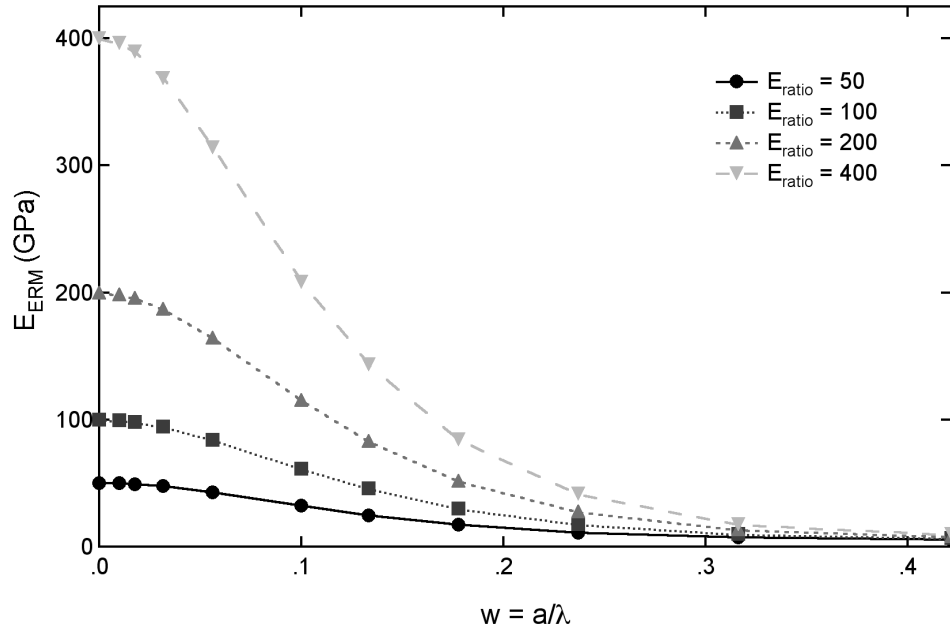


**Figure 27.  $E_{ERM}$  as a function of nanotube waviness ratio ( $a/\lambda$ ) for different ratios of phase moduli with wavelength ratio  $\lambda/d=100$ .  $E_{matrix}=1$  GPa.**

Figure 28 shows the dependence of  $E_{ERM}$  on the nanotube wavelength ratio for different values of waviness and  $E_{ratio}=200$ . We see that as the wavelength ratio increases the value of  $E_{ERM}$  converges to a constant value that is a function of the waviness. While we have shown that for longer wavelength ratios ( $\lambda/d > 1000$ ) curves of  $E_{ERM}$  versus waviness for different values of  $E_{ratio}$  can be superposed via vertical shifting (as discussed later in this section), for real NRP materials the wavelength ratio is likely to be much smaller. Unless otherwise specified, to simplify the remainder of this section we will only consider wavelength ratios of 100.

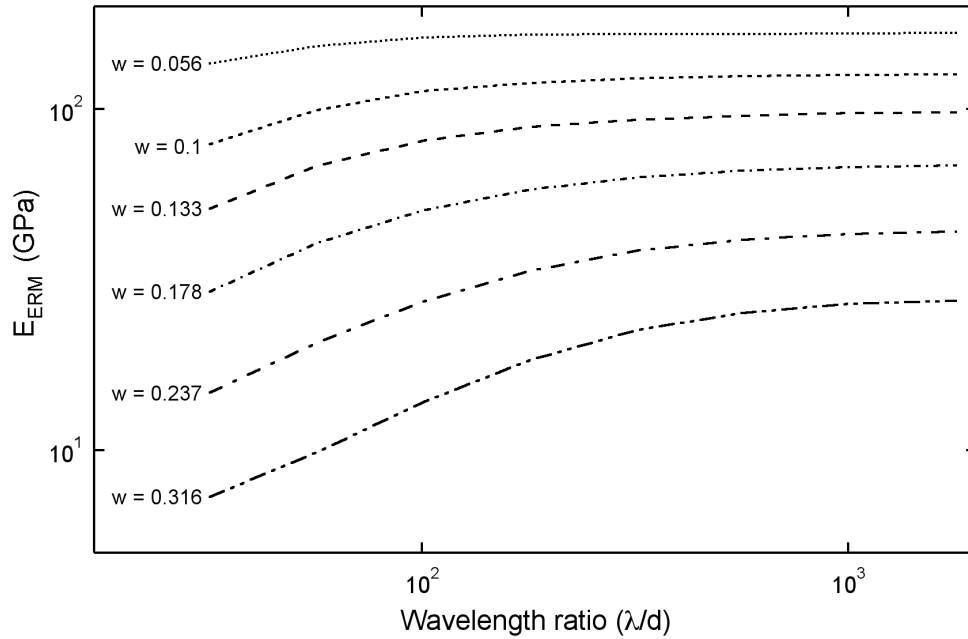


**Figure 28.  $E_{ERM}$  as a function of nanotube wavelength ratio ( $\lambda/d$ ) for different values of nanotube waviness. ( $E_{NT}=200$  GPa,  $E_{matrix}=1$  GPa).**

In Figure 29  $E_{ERM}$  (normalized with respect to  $E_{NT}$ ) is presented as a function of  $E_{ratio}$  for different values of waviness with  $\lambda/d=100$ . Note that when the phase moduli are equal ( $E_{ratio}=1$ ), the finite element cell is homogeneous and  $E_{ERM}=E_{NT}=E_{matrix}$ ; while not shown explicitly in Figure 29 all curves monotonically approach this point. With this in mind we note the strong initial decrease in  $E_{ERM}/E_{NT}$  for small values of  $E_{ratio}$ , revealing the critical role of the mechanical constraint of surrounding matrix for this case. As  $E_{ratio}$  increases the impact of the mechanical constraint diminishes, resulting in minimal changes in  $E_{ERM}/E_{NT}$  for larger values of  $E_{ratio}$  (note that in the limit as  $E_{ratio} \rightarrow \infty$  the response is that of a free-standing wavy

rod). From Figure 29 the impact of nanotube waviness on  $E_{ERM}$  is again evident; for  $w=0.056$ , the effective reinforcement provided by the wavy nanotube decreases by almost 20% for  $E_{ratio}=200$ , a modulus ratio representative of those anticipated for NRPs. For larger values of waviness the decrease in  $E_{ERM}$  is even more apparent. Note that in our simulations we are interested in the *initial* reinforcing modulus of the wavy nanotube, and do not consider the effects of nanotube straightening due to the application of an applied load.

For all previous simulations the Poisson ratios of the matrix and nanotube were assumed to be equal ( $\nu_{NT}=\nu_{matrix}=0.30$ ) to simplify the analysis. For many practical nanotube-polymer systems the difference in Poisson ratio is likely to be relatively small, with  $\nu_{NT}$  typically predicted in the range of 0.20-0.30 and  $\nu_{matrix}$  for a typical structural polymer approximately 0.25-0.40.<sup>7</sup> Simulations were conducted with constant wavy NT parameters ( $E_{ratio}=200$ ,  $\ell/d=1000$ , and  $w=0.1$ ) while varying the Poisson ratio of each phase to study the impact of the Poisson ratio mismatch on  $E_{ERM}$ . The results of this study are shown in Figure 30. We found that the value of the Poisson ratio of the nanotube is immaterial, which is not surprising considering the small volume fraction of nanotube ( $< 0.05\%$ ) modeled in the finite element cell. While the effect of  $\nu_{matrix}$  is more significant, we note that the difference in  $E_{ERM}$  is only  $\sim 5\%$

---

<sup>7</sup> The use of nanotubes as reinforcement in elastomers could potentially utilize the high elastic strains of the nanotubes (Barraza, Pompeo et al. 2002). For such polymer systems the Poisson ratios are closer to 0.5, and the Poisson ratio mismatch may be more significant.

for  $\nu_{\text{matrix}}$  between 0.25 and 0.40. Thus the results presented in this paper for  $\nu_{\text{NT}} = \nu_{\text{matrix}} = 0.30$  are in general applicable to a wide range of typical NT-polymer composite systems.

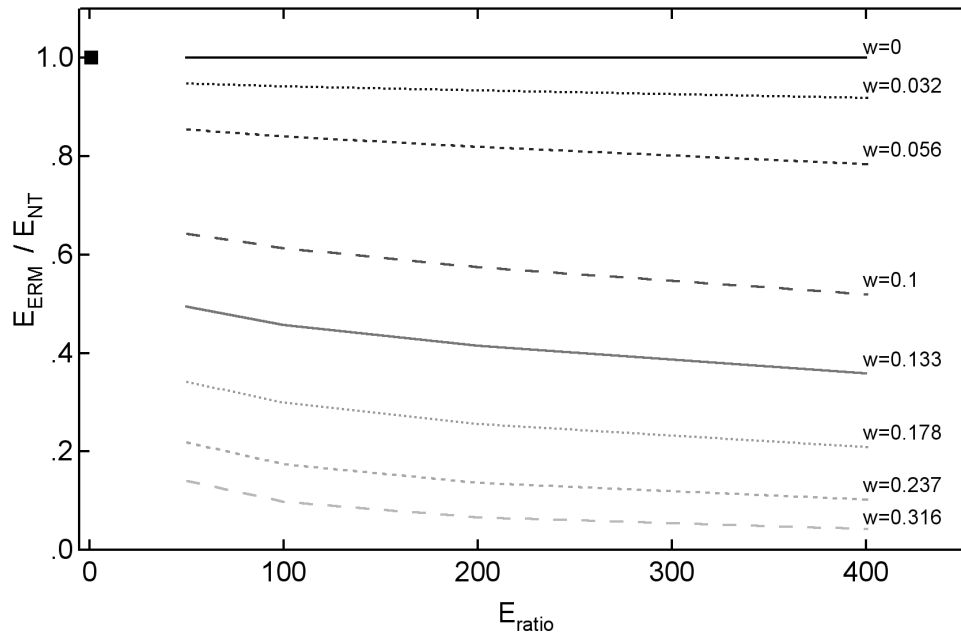


**Figure 29. Normalized  $E_{\text{ERM}}$  (with respect to  $E_{\text{NT}}$ ) as a function of  $E_{\text{ratio}}$  for  $\nu/d=100$ . For  $E_{\text{ratio}}=1$ , the material is homogeneous and  $E_{\text{ERM}}=1$  as marked; all curves monotonically approach this point (not shown for clarity).**

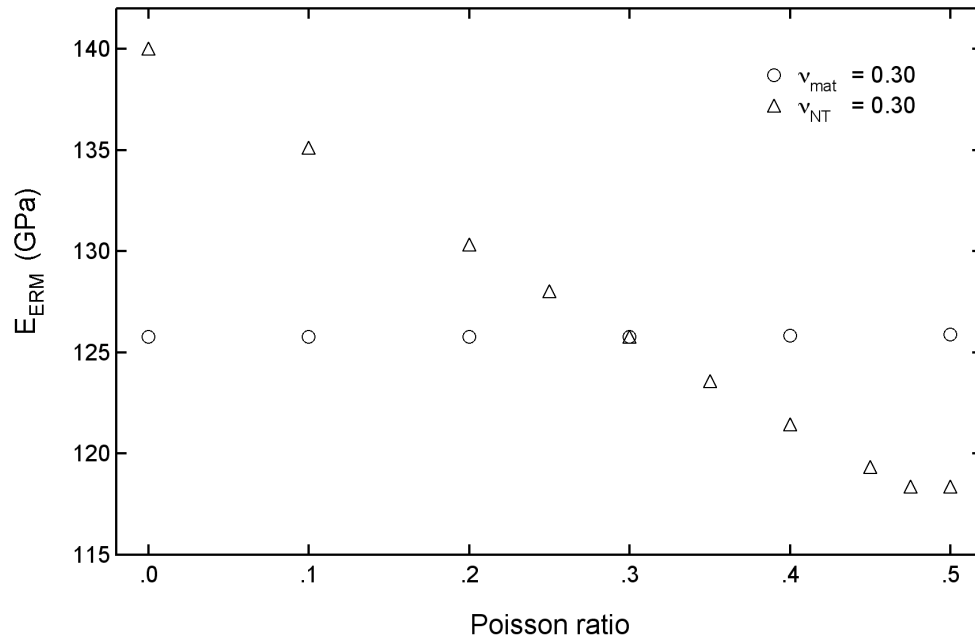


**Figure 30. Effect of Poisson ratio on the  $E_{ERM}$  values calculated from the FEM simulations. ( $\lambda/d=1000$ ,  $E_{ratio}=200$ ,  $w=0.1$ )**

In summary, we have found that the effective reinforcing modulus  $E_{ERM}$  of an embedded, wavy nanotube is strongly dependent on its geometry and the ratio of the phase moduli. As expected, the stiffening effect of the wavy nanotube decreases as the waviness of the nanotube increases, while stiffening increases as the wavelength ratio  $\lambda/d$  increases. We have also shown that  $E_{ERM}$  is a function of the ratio of the phase moduli, as the constraint of the surrounding matrix on the straightening of the wavy nanotube can be significant. Further, we have seen that for values of these parameters which are likely to be representative of wavy nanotubes embedded within a polymer

matrix, this reduction in effective modulus can be quite substantial, suggesting that the waviness of the embedded nanotubes will result in less than optimal reinforcement.

### *Analytic expressions for $E_{ERM}$ for large wavelength ratios*

From our numerical simulations we have found that for sufficiently large wavelength ratios (on the order of  $\lambda/d > 500$ , dependent on the waviness ratio), the effective reinforcing modulus  $E_{ERM}$  remains virtually constant for increasing wavelength ratios. To illustrate, Figure 31 shows how the log of  $E_{ERM}$  varies with respect to the waviness ratio for four difference ratios of phase moduli with  $\lambda/d=1000$ . Using a non-linear least squares solver we found that, for sufficiently large  $\lambda/d$ ,  $E_{ERM}$  can be approximated as

$$\log E_{ERM}(w, E_{ratio}) = \log E_{ratio} + k_1 w + k_2 w^2 + k_3 w^3. \quad (57)$$

For  $E_{ratio}=200$ , the curve fit parameters in (57) were found to be  $k_1=-0.947$ ,  $k_2=-12.90$ , and  $k_3=22.27$ . This curve fit is represented by the solid line in Figure 31, which demonstrates that the functional form of (57) well represents the data from our finite element analysis.

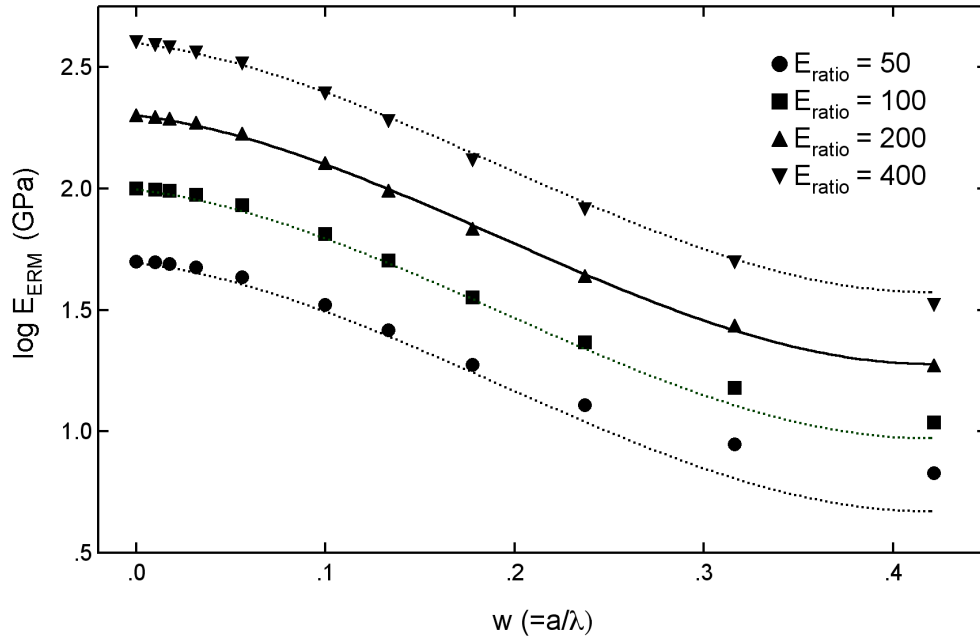


**Figure 31. Plot of  $\log E_{ERM}$  versus waviness for  $\square/d=1000$ .**

Unexpectedly, from Figure 31 it appears that the responses for different  $E_{ratio}$  seem to be related, such that the curves can be superposed (particularly for lower waviness ratios) via an appropriate vertical shifting procedure. Such a shifting procedure can be used to find the response for a particular value of  $E_{ratio}$  given the known response at a reference  $E_{ratio}$ , via

$$\log E_{ERM}(w, E_{rat}) = \log(w, E_{ERM_{ref}}) + \log\left(\frac{E_{rat}}{E_{ERM_{ref}}}\right). \quad (58)$$

This fit is demonstrated by the dashed lines in Figure 31, where the curve fit for  $E_{ratio}=200$  has been used as the reference data. This vertical shifting procedure is seen

to well describe the response for different ratios of the phase moduli, particularly for smaller waviness ratios.

We stress that the vertical shifting procedure given in (58) is only appropriate for very large values of  $\lambda/d$ , such that  $E_{ERM}$  is approximately independent of the aspect ratio. This is verified in Figure 32, which shows a plot similar to Figure 31 but for a smaller aspect ratio ( $\lambda/d=100$ ). Here it is apparent that while the general shapes of the  $E_{ERM}$  curves appear similar, the responses for different  $E_{ratio}$  cannot be related via a simple vertical shifting procedure.

While this shifting procedure is limited in that it is only applicable for larger values of the wavelength ratio  $\lambda/d$ , based on Figure 28 we note that for sufficiently small waviness ratios, the requirement of large wavelength ratio is greatly reduced. As discussed earlier, the efficiency of the nanotubes as structural reinforcement is greatly reduced for small wavelength and large waviness ratios, suggesting that NRP fabrication techniques that can control these parameters will optimize the effective modulus of nanotube-reinforced polymers. If the waviness of the embedded NTs is minimized, then the shifting procedure outlined in this section *may* be useful in analyzing  $E_{ERM}$ , and would significantly reduce the number of finite element simulations required. However, for consistency we will use  $E_{ERM}$  values calculated directly from our finite element analysis throughout the remainder of this chapter.

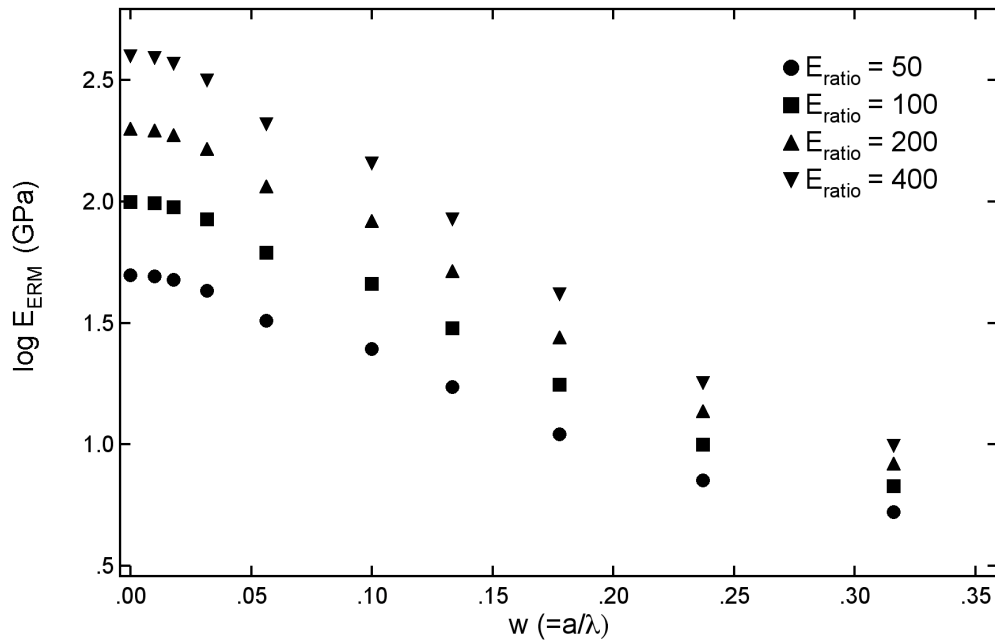
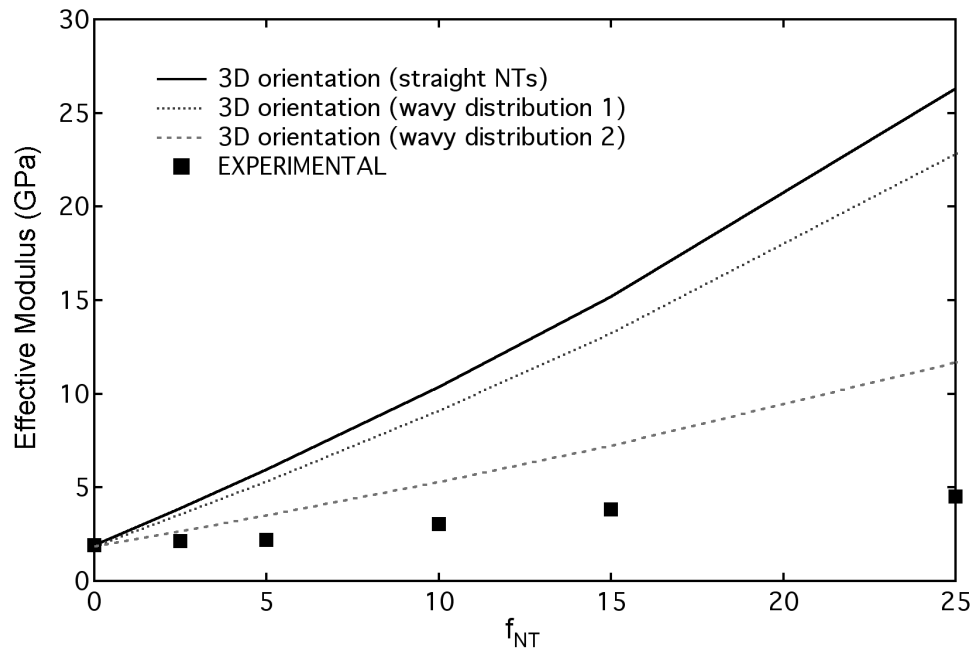


Figure 32. Plot of  $\log E_{ERM}$  versus waviness for  $l/d=100$ .

### *Micromechanical effective modulus predictions using $E_{ERM}$*

We are now in the position to use  $E_{ERM}$  within traditional micromechanics techniques in order to predict the effective modulus of NRPs. Here we highlight the procedure outlined in Figure 26 by comparing effective modulus predictions obtained using the Mori-Tanaka method with experimental tensile modulus data for various loadings of MWNTs in polystyrene (Dow 666) (Andrews, Jacques et al. 2002). The nanotubes used in this study were grown via a chemical vapor deposition process using Xylene-ferrocene (Andrews, Jacques et al. 1999) and dispersed within the polystyrene matrix via shear mixing in a Haake PolyLab bowl mixer. While the

researchers report good dispersion of the NTs within the matrix, in situ TEM straining studies have found evidence of inadequate bonding between the phases (Andrews 2001).



**Figure 33. Experimental data for MWNTs in polystyrene (Andrews, Jacques et al. 2002) and micromechanical predictions of NRP effective moduli assuming a 3D random orientation of straight and wavy nanotubes.  $E_{NT}=450$  GPa.**

In Figure 33 and Figure 34 we present the experimental data for the effective tensile modulus as a function of volume fraction of MWNTs, together with the Mori-Tanaka predictions assuming a single phase of *straight* NT inclusions randomly orientated inclusions in 3D and 2D space, respectively. Also shown are the predictions

obtained considering nanotube waviness by assuming each of the nanotube waviness distributions given in Table 7. Lacking an appropriate image of the nanostructure, these waviness distributions are loosely based on the NRP images shown in Figure 18 and represent two potential types of waviness (minimal waviness and more moderate waviness) that may be anticipated for nanotubes embedded within a polymer matrix.<sup>8</sup> For each waviness distribution  $E_{ERM}$ , for each nanotube phase was found from the finite element model described previously with  $E_{ratio}=200$  and  $\square/d=100$ . An  $E_{ratio}$  of 200 was selected to approximate a value of  $E_{NT}=450$  GPa that has been given in the literature for the modulus of NTs grown using a similar CVD method (Pan, Xie et al. 1999). These  $E_{ERM}$  values are given in Table 7. Given the waviness distribution and appropriate values of  $E_{ERM}$ , the multiphase composite analysis described in the previous section can be implemented.

---

<sup>8</sup> While it would be desirable to image a representative portion of the actual NRP sample to obtain the waviness distribution, our results nonetheless clearly demonstrate how nanotube waviness can significantly decrease the effective modulus of the NRP.

waviness ( $w=a/\lambda$ )	$E_{ERM}$ (GPa)	Volume fraction	
		NT distribution 1	NT distribution 2
0	450	0.4	0.05
0.05	383	0.4	0.15
0.1	260	0.2	0.3
0.25	57	0	0.3
0.5	10	0	0.2

**Table 7. Effective reinforcing moduli and hypothetical NT waviness distributions in the micromechanics analysis. ( $E_{ERM}$  values for  $E_{ratio}=200$  and  $\lambda/d=100$ )**

What is most striking about the results presented in Figure 33 and Figure 34 are the large discrepancies between the Mori-Tanaka predictions assuming *straight* nanotubes and the experimentally measured moduli. While the experimental modulus has been significantly enhanced with the addition of the NTs (the modulus increases by a factor of two for 15 vol% NTs), the realized improvements in modulus are significantly less than the micromechanics predictions with straight nanotubes would indicate. Integrating moderate nanotube waviness (NT distribution 2) into the effective moduli predictions is shown to drastically decrease the moduli predictions, suggesting that NT waviness may be one factor limiting the modulus enhancement of NRPs.

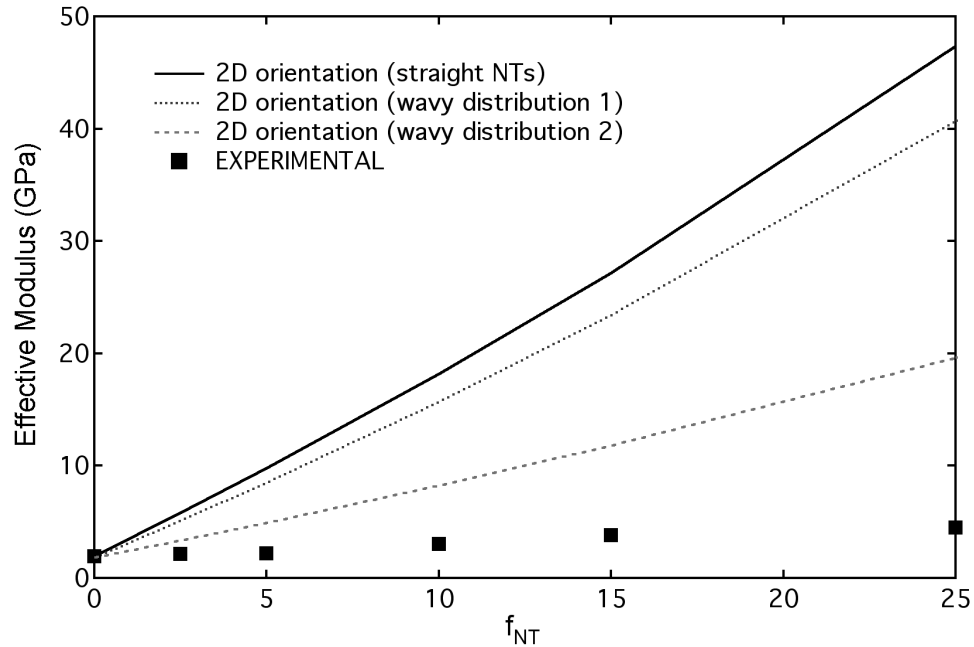


**Figure 34. Experimental data for MWNTs in polystyrene (Andrews, Jacques et al. 2002) and micromechanical predictions of NRP effective moduli assuming a 2D random orientation of straight and wavy nanotubes.  $E_{NT}=450$  GPa.**

Similar results were found for other NRP experimental data presented in the literature. Figure 35 shows the experimental modulus and micromechanics predictions obtained for 5 wt% MWNTs embedded in epoxy (Schadler, Giannaris et al. 1998), using the second waviness distribution and corresponding  $E_{ERM}$  values found in Table 7. Again the results show that the micromechanics predictions assuming straight NTs overestimate the experimental data. However, moderate NT waviness can reduce the predicted effective modulus of the NRP significantly, bringing the predictions more in line with the experimental data. The results for unidirectionally aligned NTs, also

shown in Figure 35, suggest that an order of magnitude increase in modulus may be possible for such systems.

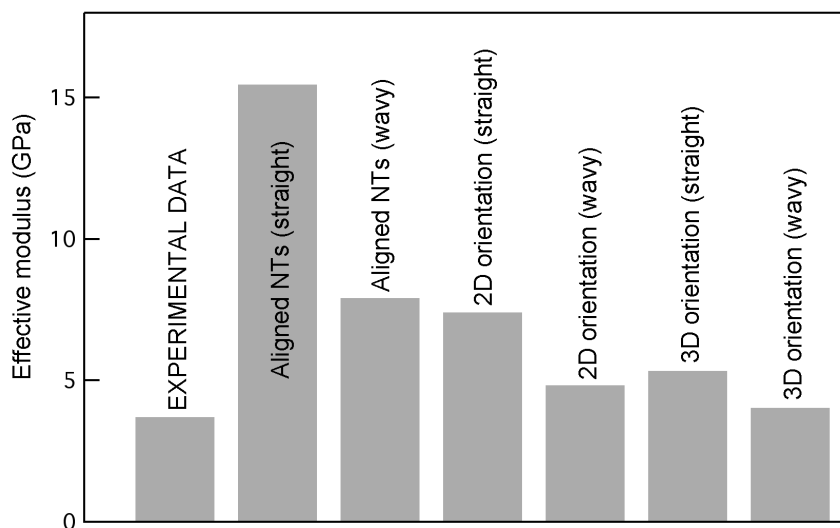


**Figure 35. Experimental data for 5 wt% MWNTs in epoxy (Schadler, Giannaris et al. 1998) and micromechanical predictions of NRP effective moduli assuming straight and wavy nanotubes with different NT orientations.**

At the moment it is impossible to distinguish the effects of nanotube waviness from other mechanisms that would tend to decrease the effective properties of the nanotube-reinforced polymer. Other conditions, such as a poor NT-polymer interface, inadequate NT dispersion, and nanotube degradation due to processing of the NRP would also result in experimental moduli less than those predicted using micromechanics. However, based on images of nanotubes embedded in polymers and

our modeling results presented here, we have demonstrated that nanotube waviness may be an additional mechanism which can strongly influence the effectiveness of nanotubes as structural reinforcement.

## **An Alternative Model to Incorporate Nanotube Waviness into Effective Moduli Predictions**

During the development of the  $E_{ERM}$  model, an alternative (albeit related) solution was conceived to incorporate inclusion waviness into micromechanical predictions of effective stiffness. In this alternative model, which we call the Numerical Strain Concentration Tensor (NSCT) method, the complete dilute strain concentration tensor  $A_r^{dil}$  is found via the solution of six separate finite element models with appropriate boundary conditions, a procedure that is described in detail in the literature (Bradshaw, Fisher et al. 2002). Once the dilute strain concentration tensor  $A_r^{dil}$  has been determined, it can then be used directly in the Mori-Tanaka solution (see equation (35)) to predict the NRP effective modulus.

The major difference between these two models is that the ERM model solves a single finite element model, analogous to a numerical tensile test, and then treats the wavy nanotube as an isotropic inclusion with a reduced modulus  $E_{ERM}$ . For the NSCT model, the solution to the six independent finite element models (with identical

geometry) yields an orthogonal effective response such that the isotropic simplification used in the ERM model is unnecessary. To demonstrate the difference in the two models, the effective moduli predictions for a two-phase *unidirectional* composite with a 10% volume fraction of NTs with  $E_{\text{ratio}}=400$  and  $\lambda/d=100$  are shown in Figure 36-Figure 38.

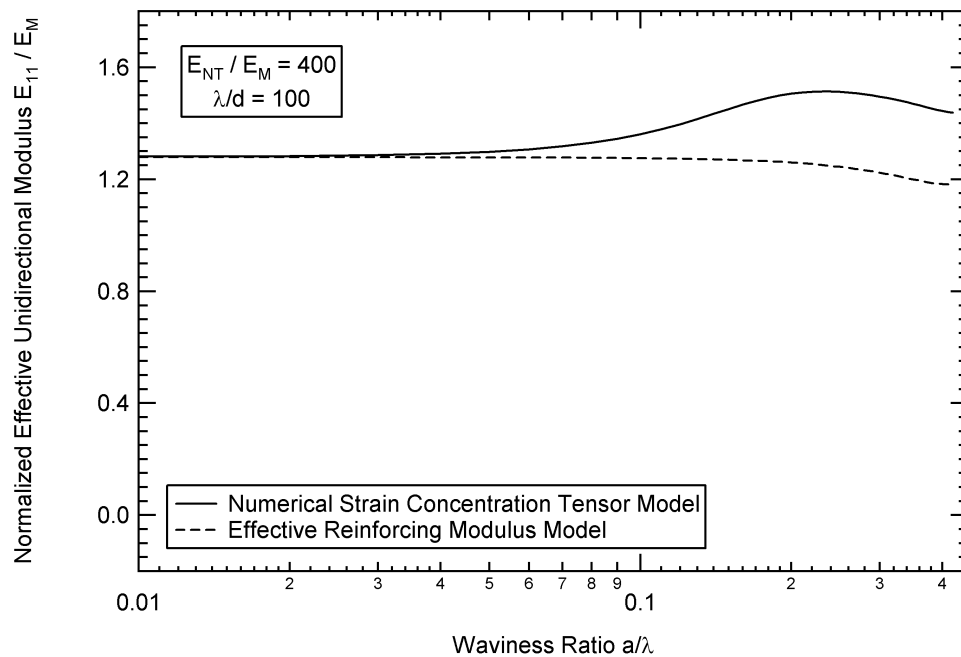


**Figure 36. Effective composite modulus  $E_{11}$  (in the x direction of Figure 21, out-of-plane of NT waviness) with increasing waviness ratio ( $a/\lambda$ ) for the ERM and NSCT models. (Bradshaw, Fisher et al. 2002)**

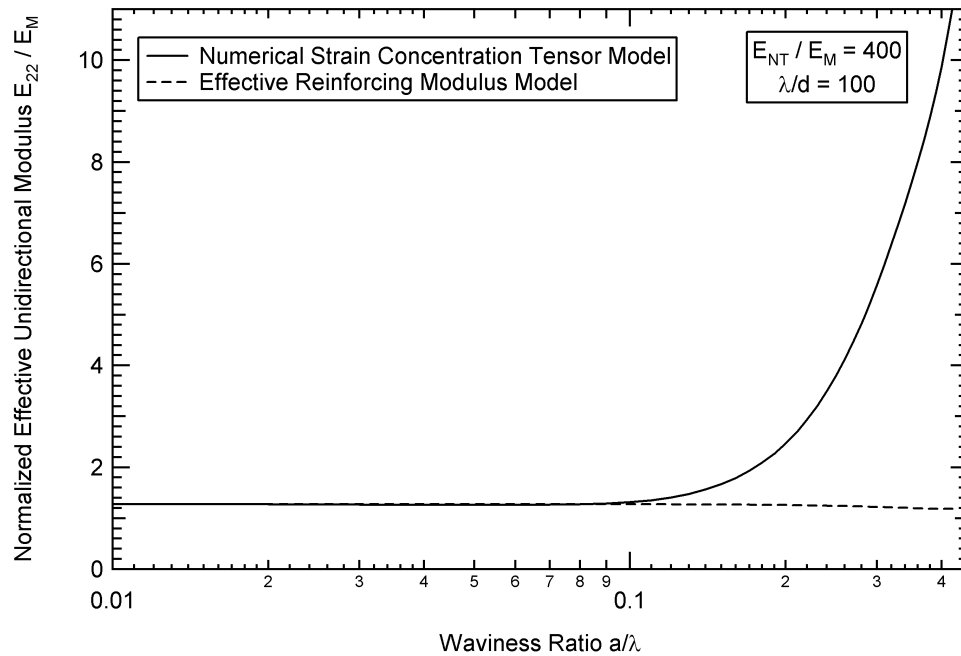


**Figure 37. Effective composite modulus  $E_{22}$  (in the y direction of Figure 21, in the plane of waviness and transverse to the NT axis) with increasing waviness ratio ( $a/\lambda$ ) for the ERM and NSCT models. (Bradshaw, Fisher et al. 2002)**

As one might expect, the largest difference between the two models is found in the  $E_{22}$  term, which the NSCT model predicts will increase for large values of waviness. This is sensible physically; as the waviness increases, the portion of the wavy nanotube that is aligned towards the 2-direction increases, such that the NT begins to provide significant reinforcement in this direction. This behavior cannot be captured in the ERM model, where only the response of a single finite element cell subject to loading parallel to the NT long axis is analyzed.

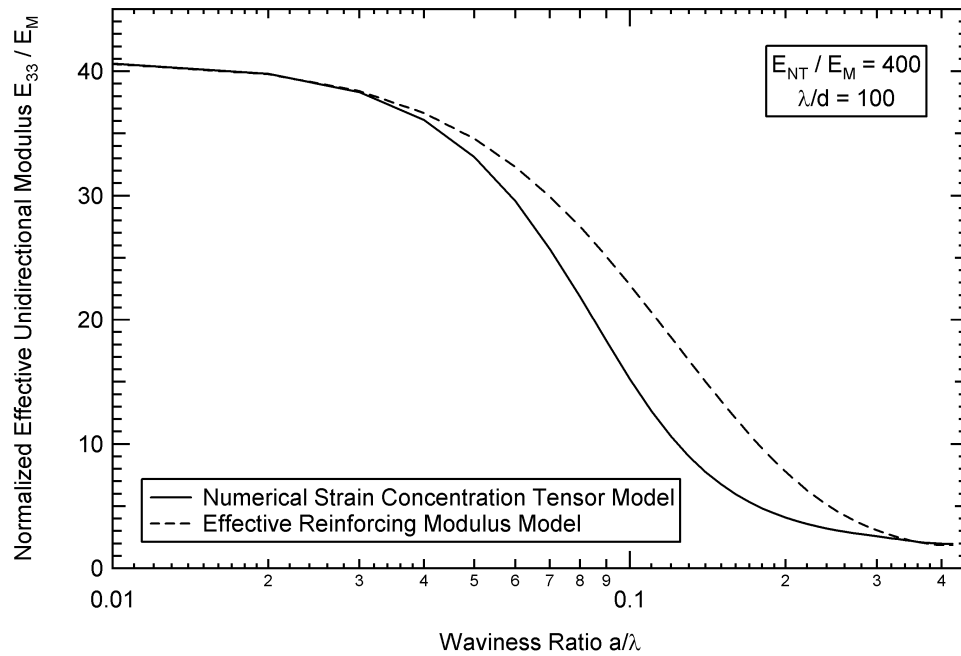


**Figure 38. Effective composite modulus  $E_{33}$  (in the z direction of Figure 21, parallel to the NT axis) with increasing waviness ratio ( $a/\lambda$ ) for the ERM and NSCT models. (Bradshaw, Fisher et al. 2002)**

The ERM and NSCT predictions for a two-phase NRP with a 3D random orientation of wavy nanotubes are shown in Figure 39. Here we assume isotropic constituent phases, a 10% NT volume fraction (where all NTs have the same waviness), and  $E_{\text{ratio}}=400$ . We see that for shorter wavelength ratios ( $\lambda/d=10$ ), the difference between the models is minimal until very large values of the waviness ratio  $a/\lambda$  are considered, at which point the NSCT model predicts a stiffer effective response. For larger wavelength ratios ( $\lambda/d=100$ ), the difference between the two models is more significant, although it should be noted that this difference is

exaggerated here given the large NT volume fraction modeled. We also note that Figure 39 assumes that all of the nanotubes have identical values of  $a/\lambda$ . As discussed previously, there is likely to be a distribution of NT waviness within the material, such that only a fraction of the nanotubes would be characterized by  $a/\lambda$  and  $\lambda/d$  parameters for which the difference between the ERM and NSCT results is significant.

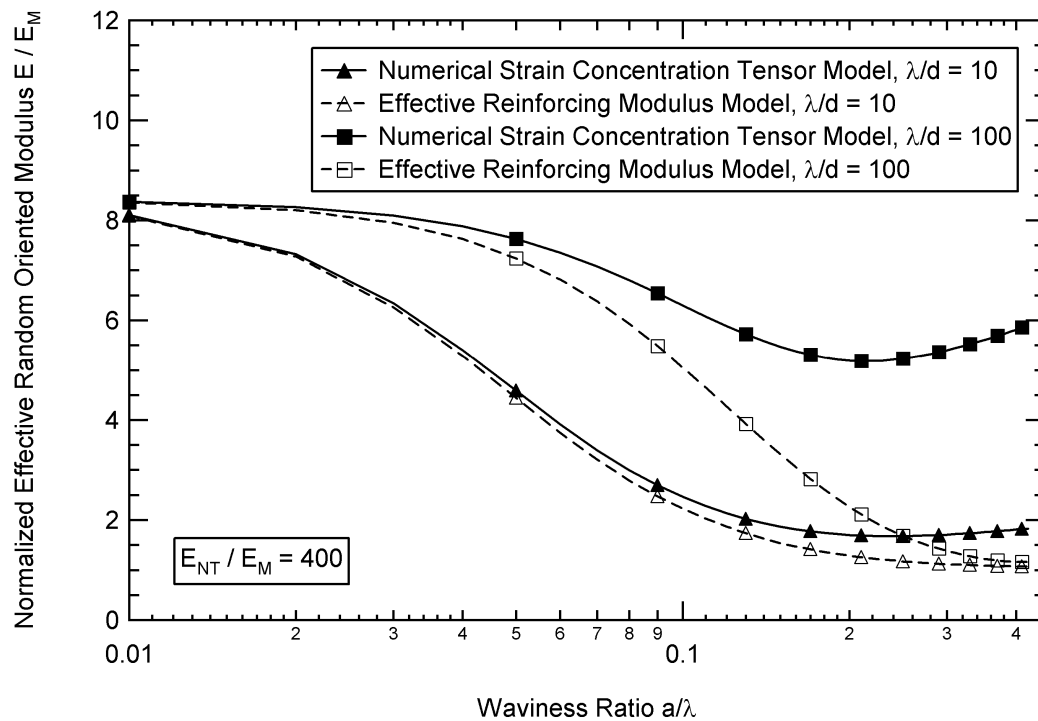


**Figure 39. Young's modulus predictions for an NRP with 3D randomly oriented wavy NTs using the ERM and the NSCT models for  $E_{\text{ratio}}=400$ . (Bradshaw, Fisher et al. 2002)**

For NRP samples with moderate waviness, the differences in moduli predictions given by the two models may be minimal and likely masked by other factors; in this case the ERM model may be preferable due to its simplicity. For cases where significant nanotube waviness is expected or has been observed, the NSCT model is preferred because it more accurately models the full impact of the wavy nanotube on the effective moduli of the NRP.

## Summary

Motivated by micrographs showing that nanotubes embedded within polymers often exhibit significant curvature, we have developed a model that incorporates this curvature into traditional micromechanical methods via a multiphase composite approach. Finite element results of embedded wavy inclusions show that the effective reinforcing moduli  $E_{ERM}$  of the inclusions quickly decreases as a function of inclusion waviness, and is also dependent on the wavelength ratio and the ratio of the phase moduli. Using material properties representative of nanotube-reinforced composites, we have shown that nanotube waviness can reduce the predicted effective moduli of these materials by a factor of two or more, and may be one reason why the modulus enhancement of NRPs, while significant, is somewhat less than predicted using standard micromechanical techniques. While for some applications (such as impact

resistance and energy absorption) nanotube waviness may be beneficial, for structural applications inclusion waviness can significantly degrade the modulus enhancement provided by the nanotube inclusions.

While here we use  $E_{ERM}$  values based on finite element modeling, alternative means to determine an appropriate value of  $E_{ERM}$ , incorporating more detailed atomic scale information, could also be used in a similar analysis. Adaptations of the current model to include inter-layer (MWNTs) and inter-tube (NT bundles) sliding, and a transversely isotropic NT inclusion, will also be addressed in future work.

Our results suggest that methods of NRP fabrication that reduce the waviness of embedded NTs would result in more efficient structural reinforcement. For example, one can hypothesize that nanotube waviness may be one reason why NRP modulus enhancement has sometimes only been reported at higher temperatures as shown in Figure 40 (Shaffer and Windle 1999; Jin, Pramoda et al. 2001). If compressive stresses developed during polymer cure introduce bending (and hence curvature) into the embedded nanotubes, significant NT reinforcement may only be realized as the NTs straighten due to polymer softening at elevated temperatures.

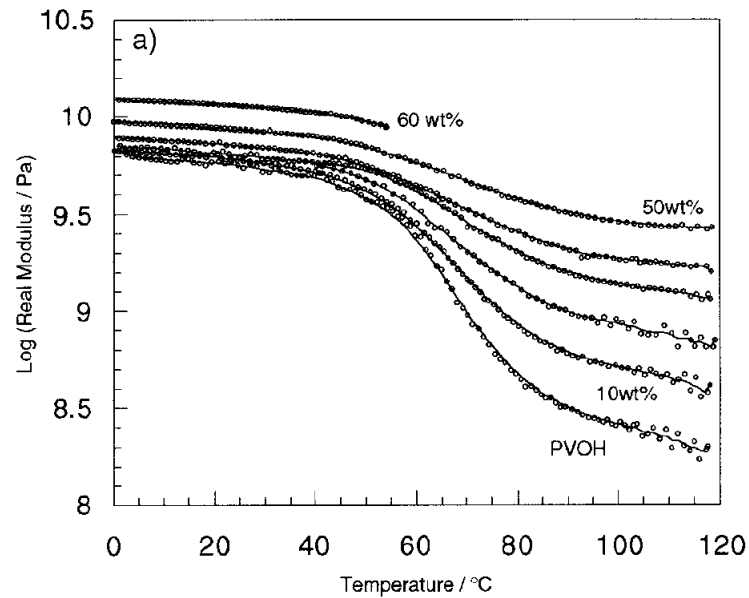


**Figure 40. Storage moduli of PVOH reinforced with MWNTs (Shaffer and Windle 1999).**

While it might seem intuitive that NT waviness would decrease the NRP effective modulus, the utility of the models presented in this Chapter is that for the first time we are able to quantify the impact of this waviness on the NRP effective modulus. One drawback of the model is that presently it is impossible to differentiate nanotube waviness from other reinforcement-limiting mechanisms in the system. Another simplification is the assumption of the sinusoidal shape describing the nanotube waviness. Based on images of free-standing and embedded nanotubes, it is likely that the waviness of the nanotube will vary both along, and between, the embedded nanotubes. Nanotube waviness is also likely to be strongly dependent on

the processing conditions and NT-polymer interaction for a particular system under investigation.

A potential means of experimentally validating the proposed model of nanotube waviness is the use of silicon nanostructures of well-defined shape and dimension, as shown in Figure 41 (Yin, Gates et al. 2000). These pieces are fabricated using a technique that combines near-field optical lithography, followed by a reactive ion etch and subsequent lift-off from the substrate. The result of the processing technique is nanometer-sized structures of single crystal silicon. This method has been proposed as a quick and efficient means of creating accurately dimensioned nanostructures at a very reasonable price.

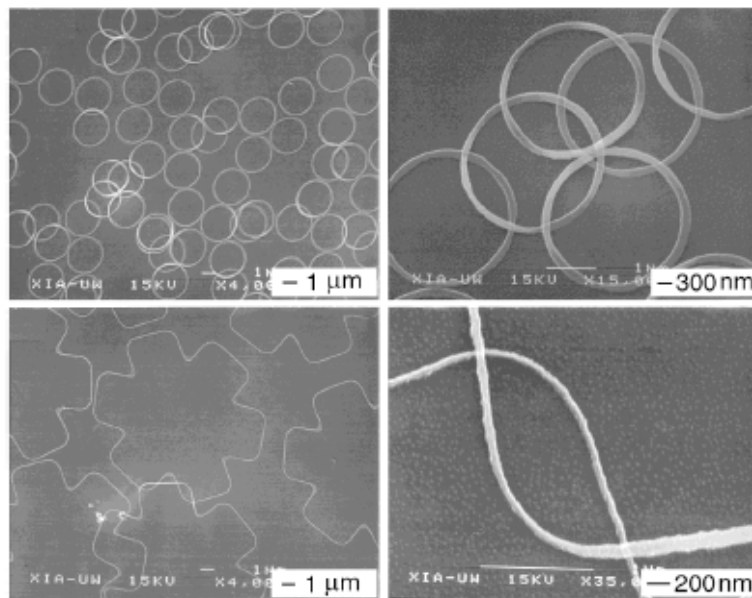


**Figure 41. SEM images of silicon nanostructures. (Yin, Gates et al. 2000)**

While the primary interest in these silicon nanostructures comes from the area of microelectronics, in regards to the current work these structures may provide model wavy inclusions of well-defined geometry as a means to experimentally validate the models proposed in this Chapter. Given that such nanowires can be easily fabricated, a model polymer matrix composite with idealized nanostructured inclusions could be produced. It would be useful to compare the experimental moduli obtained for such materials with the theoretical models presented here. While experimental validation of the proposed wavy nanotube model was beyond the scope of the work in this dissertation, future experimental work along these lines is warranted.

## CHAPTER 4: VISCOELASTIC BEHAVIOR OF CARBON NANOTUBE-REINFORCED POLYMERS

Recent experimental results demonstrate that substantial improvements in the elastic properties of a polymer can be attained by using small volume fractions of carbon nanotubes as a reinforcing phase. While these preliminary results are intriguing, to date limited theoretical and experimental work has been done to investigate the impact of the nanotubes on the viscoelastic response of the polymer. Because the nanotubes are on the same length scale as the polymer chains, it is hypothesized that the polymer segments in the vicinity of the nanotubes will be characterized by a mobility that is different from that of the polymer chains in the bulk material. This reduced mobility, non-bulk polymer behavior, which we will refer to as an *interphase*, results in significant differences between the viscoelastic (VE) behavior of the bulk polymer and that of the nanotube-reinforced polymer. Experimental work presented in the literature, and our own experimental data described below, verify this phenomena (Shaffer and Windle 1999; Gong, Liu et al. 2000). As discussed in more detail in Chapter 2, such differences in VE response are typically characterized by:

1. increases in the low temperature (below the polymer glass transition temperature  $T_g$ ) storage modulus,
2. significant increases in the high temperature (above  $T_g$ ) stiffness of the material,
3. shifting of the effective glass transition temperature of the material, usually to temperatures greater than the  $T_g$  of the polymer, and
4. broadening of the loss moduli and loss tangent peaks.

In order to further characterize the viscoelastic response of nanotube-reinforced polymers, we have started an experimental program characterizing nanotube-reinforced polycarbonate. Samples for this study have been provided by Dr. Linda Schadler at Rensselaer Polytechnic Institute, who has extensive experience in the fabrication of nanotube-reinforced polymers (see (Schadler, Giannaris et al. 1998)). She has kindly provided well dispersed samples of 1 and 2 wt% MWNTs in polycarbonate (PC), as well as pure PC samples fabricated using an identical high temperature molding process. Samples with higher loadings of NTs are currently being developed and will be the subject of future studies (Schadler 2002).

Using dynamical mechanical analysis, three modes of viscoelastic response were tested for both pure and NT-reinforced polycarbonate:

1. temperature sweeps to measure the effective glass transition temperature of the samples,
2. frequency sweeps at different temperatures to determine the relaxation spectra of the samples, and
3. time domain creep/recovery tests to study the physical aging characteristics of the materials.

The results from each form of viscoelastic testing show that the viscoelastic behavior of the NRP is different than that of the pure polymer. This behavior is attributed to the nanoscale interactions between the embedded nanotubes and the polymer chains in the vicinity of the nanotubes, which in effect causes the composite to behave as the three phase (nanotube/interphase/matrix) composite shown in Figure 42.<sup>1</sup> If one assumes that the behavior of the nanotubes is purely elastic, then the differences in viscoelastic behavior between the pure polymer and the corresponding NRP must be due to changes in the viscoelastic response of this non-bulk polymer (interphase) region. It is worth noting that, in general, the viscoelastic behavior of polymer matrix composites with micron-sized inclusions closely mirrors that of the

---

<sup>1</sup> One could also argue that an appropriate model of the response would be that of a two-phase (nanotube-altered polymer) composite, where the nanotubes cause a uniform change in polymer properties throughout the composite. However, in the authors opinion such behavior is unlikely at the nanoscale. For low volume fractions of nanotubes, there are likely to be regions of polymer so removed from the embedded nanotubes that the polymer response in this region is unaffected by the nanotubes and hence identical to that of the bulk polymer.

pure polymer used as the matrix phase. Thus models of NRP viscoelastic behavior will have to be modified to account for this reduced mobility interphase region.

Our experimental results for each mode of viscoelastic behavior ( $T_g$ , relaxation spectra, and physical aging) are consistent with the hypothesis that this non-bulk polymer phase can be characterized by restricted molecular mobility. The effect of this restricted mobility region on each mode of viscoelastic response, as well as the advantages and disadvantages of each testing procedure, are given in Table 8.

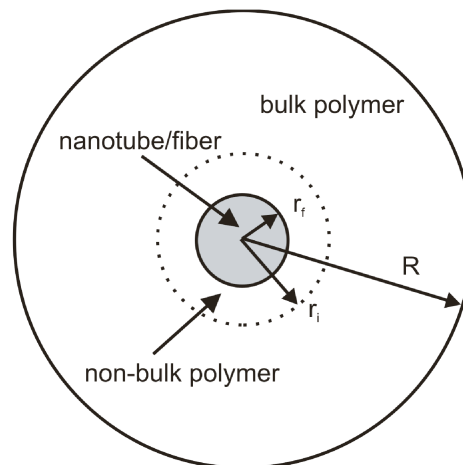


**Figure 42. Three phase model of nanotube-reinforced polymer. Interphase thickness  $t = r_i - r_f$ .**

	<b>Glass transition temperature</b>	<b>Frequency response</b>	<b>Physical aging</b>
<b>Effective NRP behavior</b>	Shift of $T_g$ to higher temperatures	Broadening of the relaxation spectra to higher frequencies	Longer times needed to rejuvenate the sample; slower effective aging <sup>2</sup>
<b>Strengths</b>	Easiest to test	Micromechanics models available	Most sensitive to the addition of the NTs
<b>Weaknesses</b>	Shift in $T_g$ is small; lack of $T_g$ molecular models	More difficult than $T_g$ analysis; less sensitive than physical aging	Most complicated to run; longer experimental times

**Table 8. Modes of viscoelastic characterization.**

In the sections that follow we will first present an introduction to viscoelasticity, focusing on a discussion of how the viscoelastic behavior of a polymer can be described based on the molecular mobility of the polymer chains. The influence of this molecular mobility on the glass transition temperature, time- and frequency-response of the material, and the physical aging characteristics of the polymer will follow. After briefly outlining the principles of dynamic mechanical analysis and the experimental tests that were conducted for this dissertation, we will present the experimental results of our testing of the glass transition temperature, frequency

---

<sup>2</sup> To date, complete rejuvenation to erase the thermal and mechanical history of the samples has yet to be achieved. However, our preliminary results lead us to believe that the long-term creep characteristics of the NRP sample will be significantly different from that of the bulk polymer. Further experimental work in this area is ongoing.

response, and physical aging of both blank (un-reinforced) and NRP samples. Included in the discussion of the frequency domain behavior will be initial modeling of the effective response using a frequency-domain Mori-Tanaka micromechanical approach. Such an approach may eventually lead to quantitative evaluation of the size and properties of the interphase region of the NRP via experimental results on macroscale-sized samples. We will conclude with a summary of the current results of this work and present future directions of research.

## **Introduction to Viscoelasticity**

The classical theory of linear elasticity assumes that the stress and strain within a material are directly proportional in accordance with Hooke's Law, such that  $\boldsymbol{\sigma} = \mathbf{C}\boldsymbol{\epsilon}$ , where  $\mathbf{C}$  is the stiffness tensor of the material and  $\boldsymbol{\sigma}$  and  $\boldsymbol{\epsilon}$  are the stress and strain in the material, respectively. The response of an elastic material is independent of strain rate (and thus time and frequency) and temperature (other than thermal expansion effects). For an elastic material, removal of the applied stress (or strain) implies the material will return to its pre-deformed shape, such that the energy of deformation required to produce the deformation is recovered. Elasticity theory properly describes the mechanical behavior of a wide range of solids, particularly at low temperatures and low levels of strain. On the other hand, for a wide range of

fluids, the state of stress is proportional to the strain rate of the material but is independent of the strain, and is described for a Newtonian fluid as  $\sigma = \eta \dot{\epsilon}$ , where  $\eta$  is the viscosity of the fluid and  $\sigma$  and  $\dot{\epsilon}$  are the stress and the rate of strain of the fluid, respectively. The energy required to deform a Newtonian fluid cannot be recovered.

The Hookean Law for elastic solids and the Newtonian Law for viscous fluids are each idealizations of material behavior, however, and do not represent accurate mechanical models for a wide range of materials. In particular, these models are insufficient to describe the mechanical behavior of most polymer systems, whose behavior can be described as having both solid-like and liquid-like characteristics. Specifically, given an applied deformation some of the energy input into the system is stored within the material (elastic response), while some of the energy is dissipated as heat (viscous response). Materials that demonstrate such behavior are better described by viscoelastic models, which incorporate both elastic-like and viscous-like response characteristics. For such materials the mechanical response is time-dependent, and can be described in terms of an integral equation of the form

$$\sigma_{ij}(t) = \int_0^t C_{ijkl}(t - \tau) \frac{d\epsilon_{kl}(\tau)}{d\tau} d\tau \quad (59)$$

where  $\sigma_{ij}$  and  $\epsilon_{kl}$  are the standard stress and strain tensors and  $C_{ijkl}$  is the time-dependent modulus. The viscoelastic behavior demonstrated by polymers is a direct

consequence of the complicated molecular motion that must underlie any mechanical deformation, as is described further in the next section.

Similar to the case of elasticity, given sufficiently small values of applied stress the response of the material is both superposable and scalable, such that when  $\sigma = \sigma_1 + \sigma_2$ ,  $\epsilon = F(\sigma) = F(\sigma_1) + F(\sigma_2)$ , and  $\epsilon = F(a\sigma) = aF(\sigma)$ , where  $a$  is a constant. In such a case the response is described as linear, and we will limit our discussion in this dissertation to such conditions. A full discussion of viscoelasticity is beyond the scope of this dissertation; the reader is directed to several excellent textbooks have been devoted to this area (Ferry 1980; Aklonis and MacKnight 1983; Tschoegl 1989).

### ***Molecular theory of polymers and viscoelasticity***

A polymer can be defined as a substance composed of molecules which have long sequences of one or more species of atoms or groups of atoms linked to each other by primary, usually covalent, bonds (Young and Lovell 1991). Thus on the nanoscale a polymer can be thought of as a “bowl of spaghetti”, where the individual polymer chains are highly entangled, and in the case of thermosetting polymers, cross-linked at various points along the chain. Whereas deformation of a solid can be simply thought of as displacements of the atoms from an equilibrium position, polymer deformation requires highly cooperative motion amongst adjacent polymer chains (and perhaps between different segments of the same polymer chain). When subject to a

given load, instantaneous rearrangements of the polymer chains result in an initial configuration of the local polymer chains that represents the (momentary) minimum free energy of the system. However, if the state of deformation is maintained over time, long-range cooperative motion of the polymer chains will result in different minimal free energy configurations. While rearrangements on a local scale are relatively rapid, the long-range cooperative motion among the polymer chains can be quite slow; this results in the range of relaxation times which typically characterize viscoelastic behavior.

It is this continual rearrangement of the polymer chains that results in the viscoelastic behavior demonstrated by most polymers. The critical parameter describing how the polymer will respond to an applied strain (or stress) is the mobility of the polymer chains. The mobility of the polymer chains is influenced by both the chemical structure (the length of the chains, the size of the side groups which are attached to the backbone chain, and entanglements and/or cross-links among the chains, etc.) and the available thermal energy. Thus, polymers demonstrate both time-dependent (based on the range of time scales that describe various configurational rearrangements of the chains) and temperature-dependent properties. The vital parameter describing the temperature-dependent response of a viscoelastic material is the glass transition temperature  $T_g$ , which is described below.

### ***Glass transition temperature***

Every polymer system has a characteristic temperature, which is known as the glass transition temperature, below which thermal motions of the individual chains is greatly restricted (Ferry 1980). This glass transition temperature is typically thought of using the concept of *free volume*. Free volume is the unoccupied “empty space” on the nanoscale; it is the available space that the polymer chains can use to accommodate their rearrangements in configuration. At sufficiently high temperatures, enough free volume is present such that the chains can instantaneously achieve their equilibrium volume, and thus the material is in thermodynamic equilibrium. Polymers at such temperatures are soft (for thermoplastic polymers the material may be in the melt state); this is referred to as the rubbery region of the mechanical response.

However, as the temperature is reduced, the amount of free volume within the polymer decreases, until eventually the molecular motion of the chains is impeded due to a lack of free volume. Because of an insufficient amount of free volume (or alternatively, thermal energy), chain motion is restricted and the viscoelastic properties of the polymer are largely independent of time (or frequency). This is referred to the glassy or pseudo-elastic state of the polymer. The temperature marking

the critical free volume at which this transition occurs is called the glass transition temperature, and is shown schematically in Figure 43.<sup>3</sup>

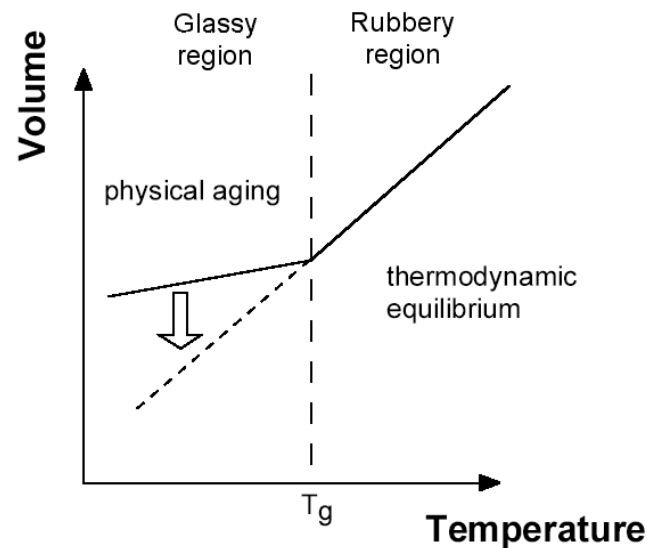


**Figure 43. The glass transition temperature and physical aging.**

Recall that a viscoelastic material is one that exhibits both elastic and viscous behavior. From the standpoint of mechanical behavior, this implies that a portion of the energy of deformation is recoverable (characterized by the storage modulus  $E'$ ) and that a portion of the energy of deformation is irrecoverable (characterized by the loss modulus  $E''$ ). The ratio of the viscous to elastic components of the polymer

---

<sup>3</sup> While we will treat  $T_g$  as a discrete temperature, in reality slight deviations in the chain configurations at the nanoscale will result in a continuous transition from glassy to rubbery behavior.

response is designated the loss tangent  $\tan \delta$ , such that  $\tan \delta = E''/E'$ . The difference in mechanical behavior between the glassy and rubbery regimes is most evident when these material properties are measured as a function of temperature.

A common method of determining the glass transition temperature of a polymer is to use dynamic mechanical analysis (DMA). In this technique, the mechanical response of a polymer is probed as a function of temperature, and the temperature at which  $\tan \delta$  is maximum is assigned as the glass transition temperature. (Note that this definition of  $T_g$  is somewhat arbitrary, and while this definition is the most common, alternative definitions can be employed as discussed in the literature.) An example of the temperature dependence of the mechanical response for an epoxy sample is shown in Figure 44. The glass transition temperature for this sample is approximately 155 °C, and coincides with the sharp drop in storage modulus.

The glassy regime of behavior (for  $T < \sim 150$  °C) is characterized by a stiff material response and a relatively constant storage modulus. As the test temperature approaches  $T_g$ , the storage modulus quickly decreases; this is referred to as the transition region of the mechanical response. For temperatures greater than  $T_g$ , the polymer response is described as rubbery, and displays a storage modulus that is orders of magnitude less than that of the glassy region. The behavior of the storage modulus in this region is strongly dependent on the chemical structure of the polymer. For thermoplastic polymers, the storage modulus will continually decrease as a

function of temperature as the polymer softens and ultimately melts at the melting temperature. For a thermoset system (such as the epoxy shown here), the rubbery region storage modulus will plateau at a relatively constant value until the polymer begins to degrade at sufficiently high temperatures.

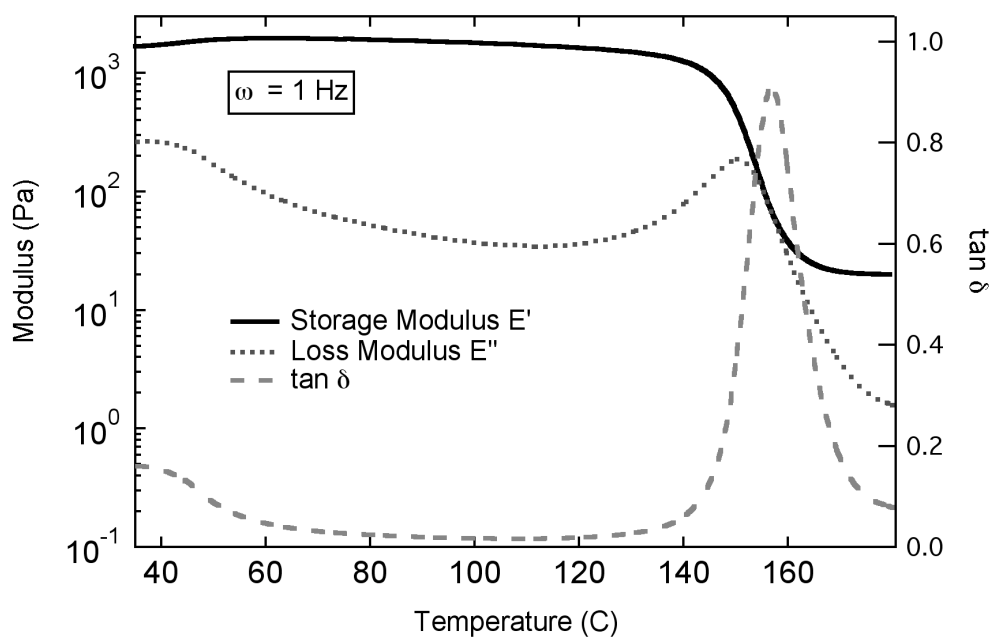


**Figure 44. Temperature dependence of the modulus of an epoxy sample.**

More information regarding the technique of dynamic mechanical analysis, along with definitions of the various viscoelastic moduli, is provided later in this Chapter. Other experimental techniques can also be used to measure the  $T_g$  of polymer samples, including differential scanning calorimetry (DSC) and thermomechanical

analysis (TMA); however, DMA is very sensitive to the changes in the underlying structure of the material and is particularly suited for transition measurements (Menard 1999).

### ***Physical aging***

Referring to Figure 43, below the glass transition temperature the material is not in thermodynamic equilibrium, as sufficient free volume is not available for the polymer chains to instantaneously achieve the minimal free energy state. Thus as the sample remains below  $T_g$ , long-scale cooperative coordination of the polymer chains will gradually allow the polymer to reach its thermodynamic equilibrium state. As this gradual evolution towards thermodynamic equilibrium takes place, material properties such as specific volume and modulus will also continuously change (Struik 1978). This process is known as *physical aging*, and is dependent on the thermal history of the sample. Because the mechanical properties of the polymer change as a result of physical aging, physical aging can have a large impact on the long-term properties of polymeric materials. For a more in-depth discussion of physical aging, the reader is referred to the literature (Struik 1978; Ferry 1980).

Physical aging is a thermoreversible process, and as such is distinct from degradative processes such as chemical aging and damage. If the sample is heated for a sufficient time above the glass transition temperature, the thermal history of the

sample is erased; this is a process called *rejuvenation*.<sup>4</sup> Once a sample has been rejuvenated, it loses all “memory” of its past thermal history. Upon a subsequent quench to below  $T_g$ , the process of physical aging then starts anew. The time spent below  $T_g$ , relative to the last rejuvenation, is called the aging time  $t_e$ .

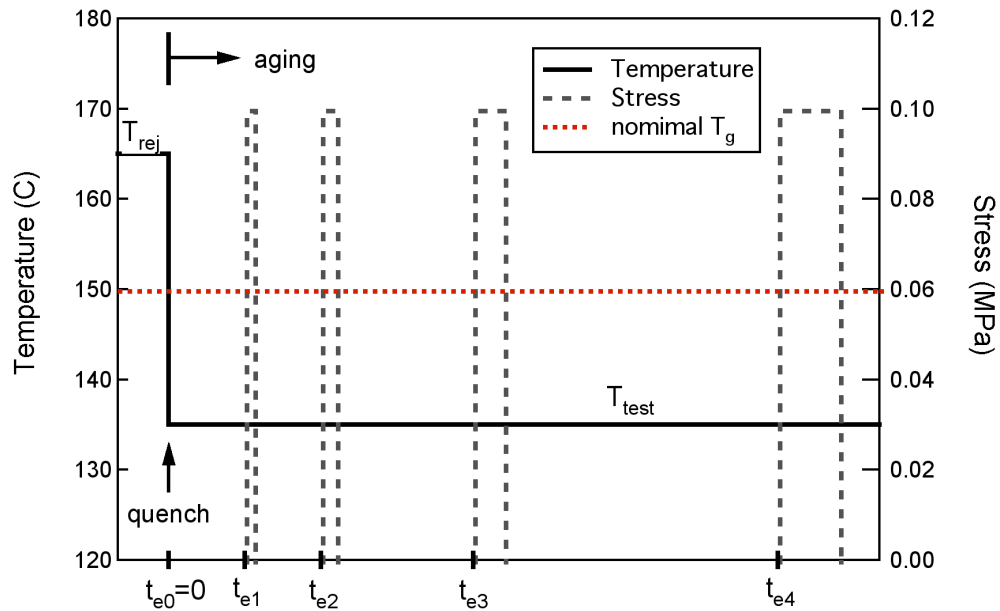


**Figure 45. Isothermal physical aging test method of Struik.**

Characterization of the isothermal physical aging characteristics of a polymer are typically carried out using the short-term creep test method developed by Struik

---

<sup>4</sup> While rejuvenation is typically thought of an instantaneous process occurring once the material is above  $T_g$ , in reality thermal gradients within the sample and other factors make it necessary to maintain the sample above  $T_g$  for a sufficient period of time before total rejuvenation takes place.

(1978) and described schematically in Figure 45.<sup>5</sup> After the material has been rejuvenated above  $T_g$  for a sufficient period of time, the sample is quenched to the test temperature  $T_{\text{test}}$  and maintained at this temperature for the duration of the test.

At different aging times  $t_e$  (time since quench), the sample undergoes a short-term creep test. The duration of the short-term test is 10% of the aging time at the start of the test, to ensure that further aging of the sample during the short-term creep test is negligible. At the end of each loading step, the applied load is removed and the sample allowed to recover until the start of the next short-term creep test. Typically the aging times at the start of each short-term test are chosen such that  $t_e^{i+1} = 2t_e^i$ . (For the experimental work discussed later in this chapter, the initial aging time was 45 minutes.) From each short-term creep test, a momentary compliance curve is obtained as shown in Figure 46 for a pure polycarbonate sample. As expected, during each individual creep test the compliance  $S(t)$  *decreases* (i.e. the stiffness *increases*) due to the molecular rearrangements of the polymer chains, which suggests a loss of chain mobility due to physical aging.

For typical physical aging of polymeric materials, the compliance curves at different aging times can be superposed through a horizontal shift. Analogous to the more standard shifting of material responses in time and frequency space (time-

---

<sup>5</sup> This method has also been extended to study the nonisothermal physical aging of polymeric materials (Bradshaw 1997).

temperature superposition, which is discussed in the next section), this shifting of momentary compliance curves is referred to as *time-aging time superposition*. Typically the momentary compliances at different aging times are shifted to the largest aging time, as this represents the compliance curve for which the greatest number of data points has been collected. An example of the shifting of the momentary compliance curves to create a reference momentary compliance curve, based on the polycarbonate data shown in Figure 46, is shown in Figure 47. The amount of shifting necessary to superpose the momentary compliance curve at aging time  $t_e$  to the reference aging time  $t_{e,ref}$  is referred to as the aging time shift factor  $a_{t_e}$ .

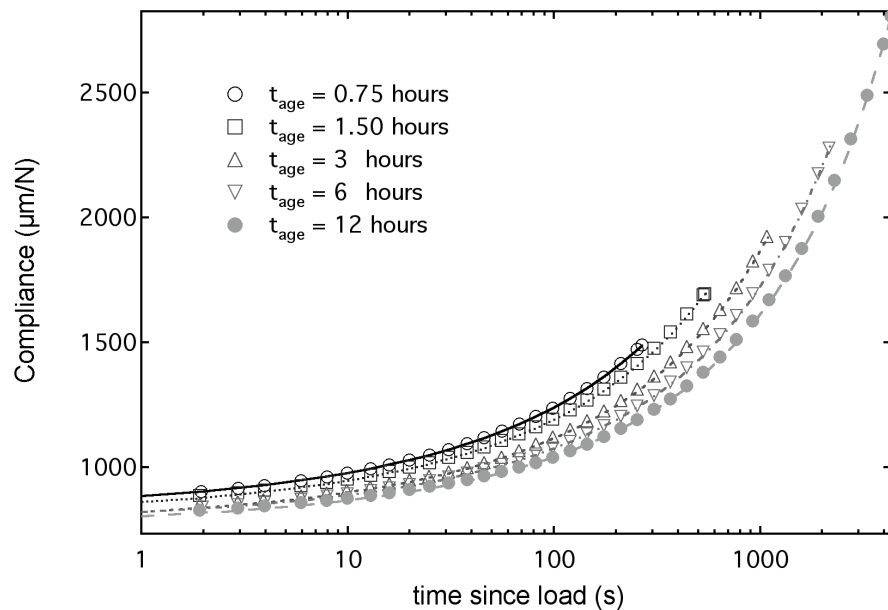


**Figure 46. Short-term momentary compliance curves for different aging times (pure PC sample, rejuvenated at 165 °C for nominal 15 minutes).**

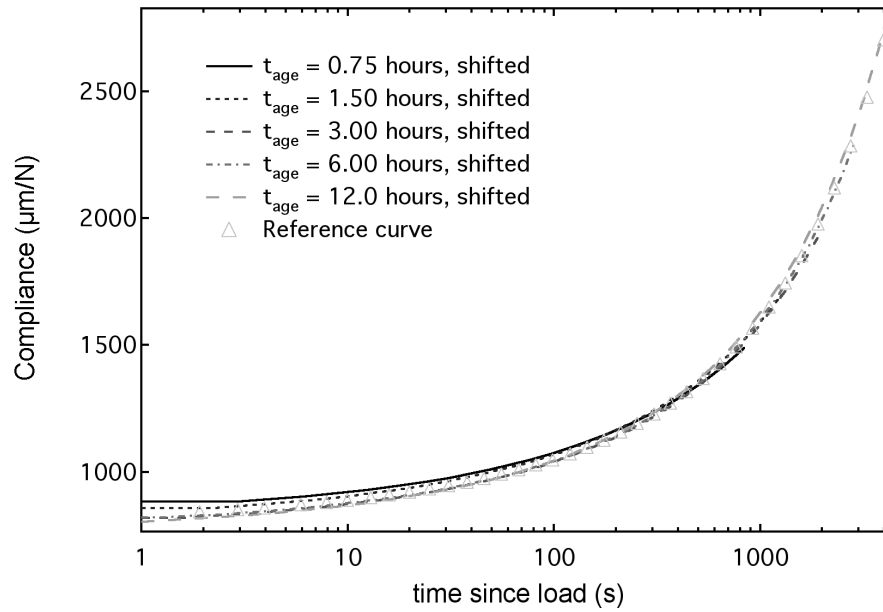


**Figure 47. Shifting of momentary compliance curves to form a reference curve (pure PC sample, rejuvenated at 165 °C for nominal 15 minutes).**

For a specimen isothermally aged at a given temperature  $T < T_g$ , it has been shown experimentally that the aging time shift factors  $a_{t_e}$  are linearly related to the aging time in log-log space via the *shift rate*  $\mu$ , such that

$$\mu = \frac{d \log a_{t_e}}{d \log t_e}. \quad (60)$$

This relationship is shown in Figure 48 for the same polycarbonate data presented earlier. The shift rate  $\mu$  is a material parameter that may be used to determine the momentary compliance (and hence the modulus) at a particular aging time given an

aging time reference curve. For most polymer materials, the shift rate  $a$  is on the order of 1 (Brinson and Gates 1995).<sup>6</sup>

Data reduction for all physical aging experimental data (including that presented above) was carried out using PHYAGE, a program developed at Northwestern to characterize the isothermal physical aging of polymers. The program uses an error minimization routine to fit an appropriate function to the experimental compliance data, and then proceeds to find the optimal reference curves and shift rates describing the physical aging of the polymer. Details of the program are provided elsewhere (Bradshaw and Brinson 1997c; Bradshaw and Brinson 1997a).

The fact that the momentary compliance curves at different aging times can be superposed via a horizontal shifting procedure demonstrates that on the nanoscale physical aging has the effect of altering the relaxation times (and thus the molecular mobility) characteristic of the polymer. Thus we suspect that the embedded carbon nanotubes may alter the physical aging response of the polymer, when compared to physical aging of the un-reinforced sample. Later in this chapter we will present our initial findings in this regard, which seem to verify this hypothesis.

---

<sup>6</sup> Given a sufficiently long period of physical aging, the material will eventually reach effective equilibrium, which is characterized by an order of magnitude decrease in the shift rate (McKenna, Leterrier et al. 1995). However, effective equilibrium is not considered in the present work.

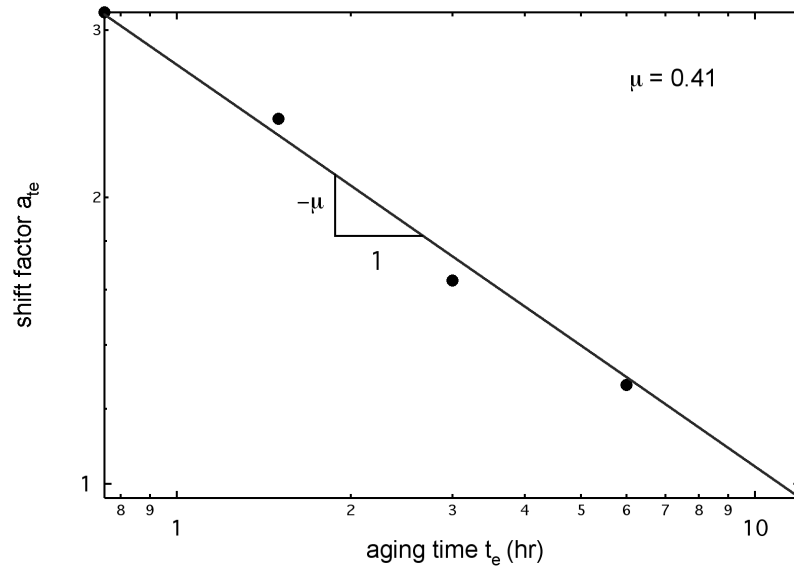


**Figure 48. Shift factors and the shift rate  $\mu$  describing physical aging. (Data for pure PC sample, rejuvenated at 165 °C for nominal 15 minutes)**

### *Time- and frequency- domain response*

Based on the previous discussion of the molecular structure of polymers, it is not surprising that such materials exhibit time-dependent properties. The viscoelastic time-dependent modulus can be characterized by a Prony series representation of the form

$$E(t) = E + \sum_{j=1}^N E_j e^{-\left(\frac{t}{\tau_j}\right)}, \quad (61)$$

where  $E$  is the rubbery asymptotic modulus,  $E_j$  are the Prony series coefficients, and  $\tau_j$  are the relaxation times. Taking the half-sided Fourier transform of (61) yields<sup>7</sup>

$$\bar{E}(\omega) = \int_0^{\infty} E(t) e^{i\omega t} dt, \quad (62)$$

where  $i$  is the imaginary number. The frequency-domain response is described by the complex modulus  $\bar{E}^*(\omega)$ , which is defined as

$$\bar{E}^*(\omega) = E'(\omega) - iE''(\omega), \quad (63)$$

$$E'(\omega) = E + \sum_{j=1}^N \frac{E_j \omega^2}{\tau_j^2 + \omega^2}$$

$$E''(\omega) = \sum_{j=1}^N \frac{E_j \omega}{\tau_j^2 + \omega^2}. \quad (64)$$

The terms defined in (64) are referred to as the storage modulus  $E'(\omega)$  and loss modulus  $E''(\omega)$ , respectively.<sup>8</sup> The storage modulus is a measure of the energy stored

---

<sup>7</sup> While this is generally referred to as a Fourier transform, note that it is missing the factor of  $1/2\pi$  that typically appears in the standard definition of the Fourier transform.

<sup>8</sup> Such notation follows the standard convention of viscoelasticity, where the use of single primes and double primes denote storage (elastic) and loss (viscous) components of a complex material function, respectively. This notation will be used throughout this dissertation.

and recovered by a viscoelastic material per cycle of sinusoidal deformation, whereas the loss modulus is a measure of the energy dissipated as heat during a similar cycle (Tschogel 1989). Note that as written in (64) both the storage and loss moduli are real quantities.

The ratio of the loss modulus to the storage modulus is referred to as the loss tangent  $\tan \delta$ , such that

$$\tan \delta = \frac{E''}{E'}. \quad (65)$$

The loss tangent is related to the ratio of energy loss to energy stored in the deformation cycle. Note that the loss tangent is a dimensionless parameter. An example of the storage and loss moduli and the  $\tan \delta$  as a function of temperature (for a constant frequency, sinusoidal deformation) was given previously in Figure 44.

### **Time-temperature superposition**

While experimental measurements of the polymer response can in theory be measured for any length of time, time scales on the order of months or years would be impractical for most applications. Here one can use the principle of time-temperature superposition, a method of reduced variables, in order to extend the time scales (by many orders of magnitude) of the response at a particular temperature of interest. For example, since experimental data may only be available over a limited range of

frequencies, the principle of time-temperature superposition is extremely useful in that it can extend the range of frequencies over which the material behavior can be studied. Because time-temperature superposition is a standard tool for the analysis of experimental viscoelastic data, it will only be briefly described below. The reader is referred to any classical book on viscoelasticity for a more precise treatment; see for example Ferry (1980).

The basic principle of time-temperature superposition (analogous to time-aging time superposition described previously) is that the material behavior at different temperatures can be superposed via horizontal shifting in log-log space to form a reference (or master) curve at a given temperature. This permits one to have a measure of the polymer response over a range of time (or frequency) scales using data collected within experimental accessible time scales.

This procedure is demonstrated using creep compliance data collected on an epoxy sample as shown in Figure 49 (O'Brien, Mather et al. 2001). Here data is collected over a relatively short time range (up to approximately 100 s) at temperatures ranging from 30 °C to 175 °C. These individual creep compliance curves are then shifted to the right (higher temperatures are shifted further and correspond to longer times) and superpose to form the master reference curve at 30 °C. Thus using time-temperature superposition, the material behavior at 30 °C is now available over approximately 14 orders of magnitude, which would certainly be inaccessible

experimentally. Mathematically, the shifting of material response data collected at different temperatures can be expressed as

$$E(t;T_1) = E\left(\frac{t}{a_T};T_{\text{ref}}\right), \quad (66)$$

where  $a_T$  is referred to as the temperature shift factor and  $T_{\text{ref}}$  is the temperature of the master curve.

Frequency-domain data collected at different temperatures can be shifted in an equivalent manner, providing the material response at a given temperature over a large range of frequencies. Occasionally slight vertical curve shifting will be required (this is true for both the time and frequency domain experimental data); often the basis of this vertical shifting is the temperature-dependence of the polymer density as discussed further in the literature (Ferry 1980; Aklonis and MacKnight 1983). Because time-temperature superposition was only used here as a means to extend the range of frequencies available for the collection of experimental data, further discussion of topics associated with time-temperature superposition (such as the standard WLF representation of the temperature shift factors) is not warranted here. The reader is referred to the literature for further reading in this area (Ferry 1980; Aklonis and MacKnight 1983).

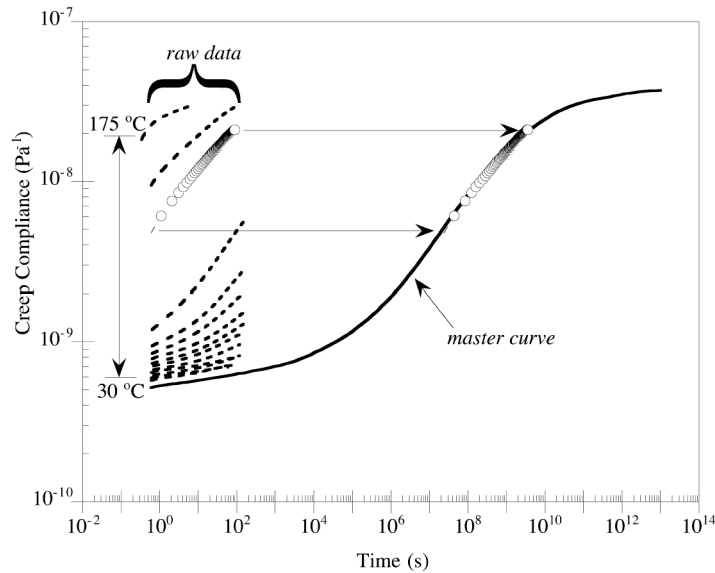


**Figure 49. Time-temperature superposition for the creep compliance of an epoxy.**

**$T_{ref}=30\text{ °C}$ . (O'Brien, Mather et al. 2001).**

### Relaxation spectrum

As the number of the Prony series elements representing the time dependent modulus in (61) goes to infinity, one obtains a continuous spectrum of relaxation times describing the viscoelastic response of the polymer. In this case, the time-dependent modulus can be expressed as

$$E(t) = E + \int_0^t H(\tau) e^{-\frac{t-\tau}{\lambda}} d(\ln \lambda) \quad (67)$$

where  $H(t)$  is referred to as the relaxation spectrum. The relaxation spectrum represents the infinitesimal contributions to the modulus from relaxation times lying in the range from  $t$  to  $t + dt$ . The relaxation spectrum is useful in qualitatively gauging the distribution of relaxation mechanisms (and hence, again, molecular mobility) at different time scales (Ferry 1980). Thus the relaxation spectrum will give us a qualitative manner in which to analyze the impact of the embedded nanotubes on the relaxation mechanisms of the nanotube-reinforced polymer.

For our purposes it will suffice to use Alfrey's approximation of the relaxation spectrum, which is defined as

$$H(t) \approx -\frac{dE(t)}{d \ln(t)}. \quad (68)$$

Thus the relaxation spectrum can be approximated as the negative slope of the time-dependent modulus (Ferry 1980). Assuming that a Prony series representation of the time-dependent modulus is known, the relaxation spectrum can thus be approximated via the analytical expression

$$H(t) \approx \sum_{j=1}^N \frac{t}{\tau_j} E_j e^{-\frac{t}{\tau_j}}. \quad (69)$$

Equation (69) was used to approximate the relaxation spectra for the different samples, and used the Prony series elements determined from the curve-fitting procedure described later in this Chapter.

### ***An interphase region in nanotube-reinforced polymers***

Because the nanotubes are on the same length scale as the polymer chains, it is anticipated that the NTs will alter the local polymer morphology in the region directly surrounding the nanotube (see Figure 42). We refer to this region of non-bulk polymer behavior as the interphase, borrowing a term used in the composites community that refers to the region separating the fiber and matrix phases. Due to changes in the local chain structure of the polymer, the interphase region will have mechanical properties different from those of the bulk polymer. While in traditional composites research the interface region is generally attributed to a host of factors (such as the use of fiber sizings, mechanical imperfections, unreacted polymer components, etc.), here we limit our discussion specifically to the change in molecular mobility of the polymer chains in this region due to the presence of, and interactions with, the nanotube inclusions.

Recent experimental work has estimated the interphase thickness for carbon fiber-epoxy composites to be on the order of 1  $\mu\text{m}$  for a 25  $\mu\text{m}$  diameter fiber (Thomason 1995; Mai, Mader et al. 1998). Because the interphase region makes up a very small fraction of the micron-sized fiber composite, its impact on the overall

viscoelastic response of the material is often neglected. However, recent molecular dynamic simulations of NRPs suggest that the local changes in the polymer structure are on the same length scale as the diameter of the NT, as shown in Figure 50 for a SWNT/PmPV/LaRC-SI composite system. (Odegard, Gates et al. 2001b; Wise and Hinkley 2001). In this case, the volume fraction of the interphase within an NRP will be much larger than the interphase region in a micron-sized composite.

For the system shown in Figure 50, poly(m-phenylenevinylene) (PmPV) is used to enhance the interfacial characteristics of the system, as it has been shown that such molecules tend to helically wrap themselves around the nanotube (Lordi and Yao 2000). From Figure 50 we see that the local density of the polymer molecules is greater in the vicinity of the nanotube, which from a molecular standpoint can be viewed as reducing the molecular mobility of these polymer chains (in comparison to those exhibiting bulk polymer behavior). It is hypothesized that such behavior will also be exhibited in nanotube-reinforced polymer systems without the use of an interfacial polymer, although much more work in this area is required.

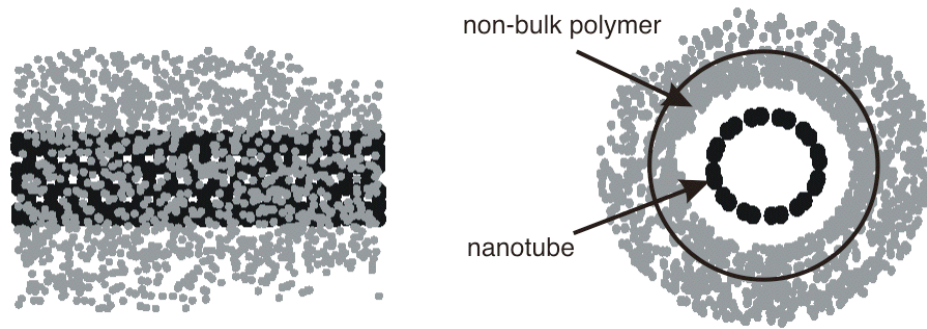


**Figure 50. Equilibrium structure of a (6,6) SWNT/PmPV/LaRC-SI composite system based on molecular dynamics simulations (Odegard, Gates et al. 2001b).**

Because the nanotubes have significantly more surface area (per unit volume) than micron-sized inclusions, a significant fraction of the polymer in NRP systems will be in the near vicinity of an embedded nanotube, and thus may be characterized by this non-bulk behavior. From simple geometric considerations (see Figure 42), the volume fraction of the interphase region  $V_i$  is related to the volume fraction of the fiber/nanotube inclusion  $V_f$  and the thickness of the interphase region  $t$  as (Fisher and Brinson 2002)

$$V_i = \frac{2t}{r_f} V_f + \frac{t^2}{r_f^2} V_f = \alpha V_f. \quad (70)$$

Likewise, the ratio of the volume fraction of the non-bulk polymer phase (interphase) to the total volume fraction of viscoelastic phases within the composite (interphase and matrix) can be expressed as

$$\frac{V_i}{V_i + V_m} = \frac{\phi V_f}{1 - \phi V_f}. \quad (71)$$

These expressions are shown graphically in Figure 51 as a function of fiber/nanotube volume fraction for various ratios of interphase thickness  $t$  to fiber radius  $r_f$ . Representative values of  $(t/r_f)$  are on the order of 0.05 for carbon fiber composites (Thomason 1995) and 1.0 for nanotube-reinforced polymers (Wise and Hinkley 2001), respectively.

From Figure 51, we see that for the case of nanotube-reinforced polymers (where the ratio  $t/r_f$  is on the order of 1.0), a significant portion of the NRP can be characterized as the interphase region. In this case, the non-bulk polymer behavior of the interphase region is expected to contribute to the overall viscoelastic response of the material. For the case for traditional micron-sized fiber polymer composites, where the ratio  $t/r_f$  may be on the order of 0.05, the interphase region is much smaller and often neglected in micromechanical predictions of effective properties.<sup>9</sup> We note that Figure 51 suggests that the interphase volume fraction will be appreciable for even relatively low loadings of nanotube inclusions.

---

<sup>9</sup> Fiber sizings are known to significantly enhance the fiber-matrix interface in traditional polymer matrix composites. However, because the interphase region in such systems is typically small, it is often neglected in micromechanical predictions for the effective modulus of these materials.

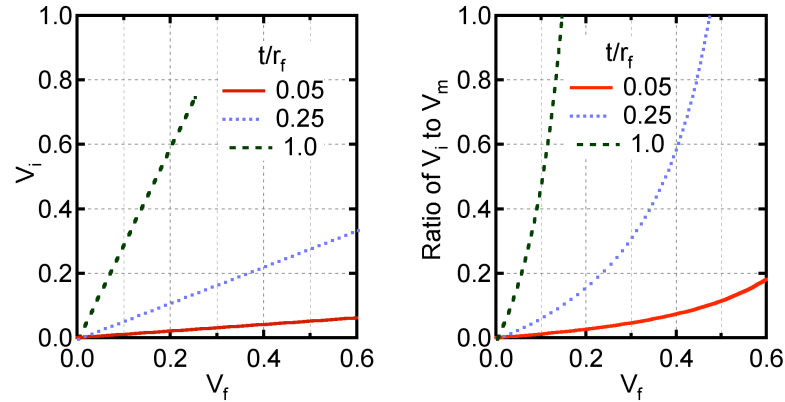


**Figure 51. Interphase volume fraction ( $V_i$ ) (left) and ratio of the interphase (non-bulk) to matrix (bulk) volume fraction ( $V_m$ ) (right) as a function of fiber volume fraction  $V_f$ .**

Perhaps the simplest means to model this non-bulk polymer behavior is to assume a distinct interphase region, within which interactions between the nanotubes and the polymer chains alter the characteristic relaxation times of the material. Recalling the Prony series form for a viscoelastic modulus discussed previously, the change in relaxation times of the interphase region can be modeled via the introduction of a mobility parameter  $\mu$ , which relates the mobility (and hence the mechanical properties) of the interphase to that of the pure polymer matrix (Fisher and Brinson 2002), such that<sup>10</sup>

---

<sup>10</sup> It is also likely that interactions between the polymer chains and the nanotubes will result in changes in the magnitude of the time (and frequency) domain moduli of the interphase region with respect to that of the pure polymer. Such changes could be incorporated into this model via multiplication of the Prony coefficients  $E_j$ . Such modeling efforts will be pursued in future work.

$$E(t) = E + \sum_{j=1}^N E_j e^{-\frac{t}{\tau_j}}. \quad (72)$$

The effect of the mobility parameter  $\tau_j$  on the time domain modulus of the material is shown schematically in Figure 52. In this manner the mobility parameter  $\tau_j$  can be used to qualitatively characterize the change in mechanical properties of the non-bulk polymer phase. For  $\tau_j < 1$  the polymer chains are more mobile, which shifts the transition region of the time-dependent response to shorter times. For  $\tau_j > 1$ , the opposite is true and the response of the non-bulk phase is stiffer than its bulk polymer counterpart. By definition,  $\tau_j = 1$  describes the bulk polymer response. Assuming such a form for the mechanical properties of the non-bulk polymer interphase region, one can use various micromechanical models to interpret experimental data for carbon nanotube-reinforced polymers. Such a procedure will be demonstrated later in this chapter.

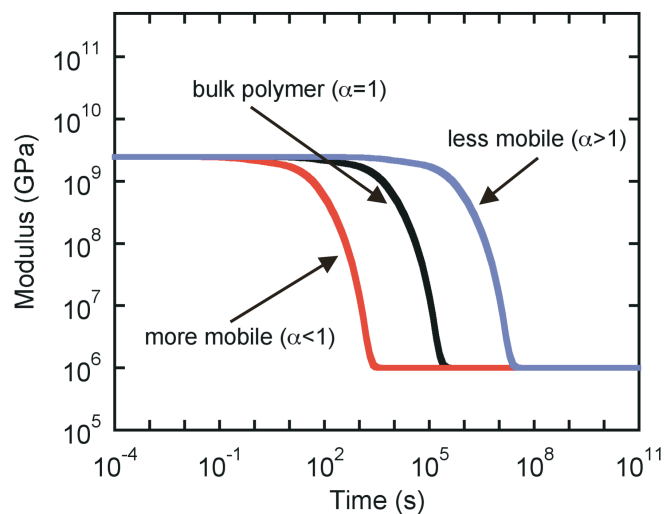


**Figure 52. Time-dependent modulus as a function of the mobility parameter  $\alpha$ .**

## Experimental Procedures

All experimental data described in this dissertation were collected using a TA Instruments DMA 2980 dynamic mechanical analyzer with a special film tension clamp (see Figure 53). Critical instrument specifications are as follows: temperature range from  $-150$  to  $600$  °C (using liquid nitrogen as a coolant), frequency range from  $0.001$  to  $200$  Hz, and a maximum applied force of  $18$  N. The film tension clamp was designed for specimens between  $5$  to  $30$  mm in length, up to  $8$  mm in width, and up to  $2$  mm in thickness. Typical lengths of the polycarbonate samples tested were (length  $\times$  width  $\times$  thickness)  $10 \times 6 \times 0.5$  mm.

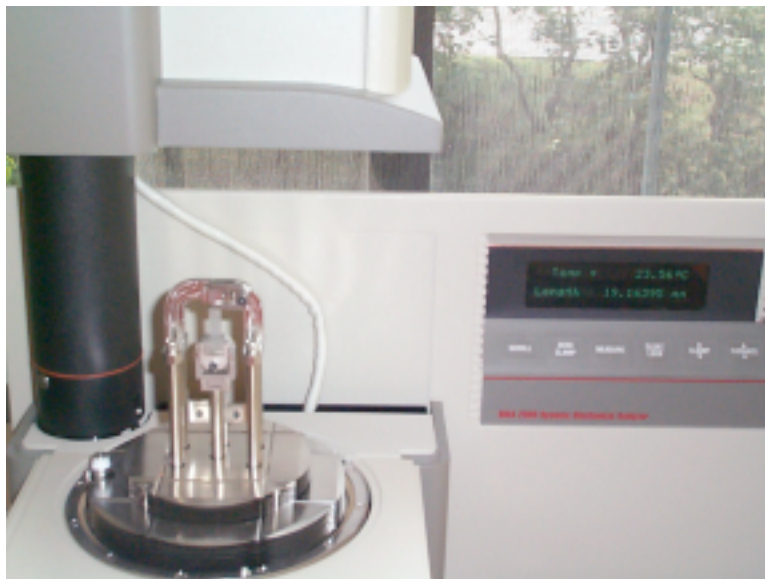


**Figure 53. TA Instruments DMA 2980 with film tension clamp.**

Nanotube-reinforced polycarbonate samples were provided by Dr. Linda Schadler at RPI, who has extensive experience fabricating nano-reinforced polymer samples. The samples were fabricated using a high-temperature molding operation that is proprietary. Currently we have received and tested both pure polycarbonate samples (fabricated using the same method as used for the reinforced polymer samples) and samples with 1 and 2 wt% embedded MWNTs; additional samples with other weight fractions of MWNTs will be tested in the future. The MWNTs used in the samples were provided by Dr. Rodney Andrews at the University of Kentucky, and were grown via chemical vapor deposition using Xylene-ferrocene as the carbon source. The outer diameters of the nanotubes are on the order of  $\sim 25$  nm. These samples are believed to have an excellent dispersion of nanotubes (Schadler 2002), and based on

Dr. Schadler's expertise in this area (Schadler, Giannaris et al. 1998; Ajayan, Schadler et al. 2000; Siegel, Chang et al. 2001), we believe these samples represent high-quality nanotube-reinforced polymers.

The samples were received from Dr. Schadler in the as-molded shape and stored for at least 24 hours in a room temperature desiccator using Drierite (Xenia, OH) as a desiccant. For DMA analysis, the samples were cut to size using a Struers (Cleveland, OH) Accutom-5 saw with a diamond blade (300 CA) running at 1000 rpm and a feed speed of .05 mm/s, using water as a coolant. The cut edges were then polished using 240 and 600 grit Carbimet grinding paper from Buehler (Lake Bluff, IL). Then samples were then returned to the desiccator for a period of at least 24 hours, and maintained in the desiccator until removed for testing.

Three types of viscoelastic testing were conducted using the DMA 2980. For temperature sweeps to measure the glass transition temperature, the samples were subjected to a sinusoidal displacement of 3  $\mu\text{m}$  (resulting in strains less than 0.1%) at a constant frequency of 1 Hz. After inserting the sample into the DMA, but prior to load, the sample was held isothermally at the initial test temperature (typically just above room temperature) for 10 minutes so that thermal equilibrium was established. The sinusoidal deformation was then initiated, and the temperature was ramped at 2°C/min until the final test temperature was reached (typically  $T_g + 30^\circ\text{C}$  for the pure polycarbonate samples and  $T_g + 50^\circ\text{C}$  for the reinforced samples).

For the testing of the frequency-domain response of the samples, the samples were held isothermally at the initial test temperature (typically 100 °C) for 15 minutes. The samples were then subjected to sinusoidal deformation at a constant amplitude of 3  $\mu\text{m}$ , at discrete frequencies from 200 to 0.2 Hz (five frequencies per decade, evenly spaced in log frequency space). After the testing at a particular temperature was completed, the temperature was raised 5°C (taking less than 1 minute), held isothermally for 5 minutes, and then the frequency scanning at the new test temperature conducted. This procedure was repeated until the measurements at the final test temperature (170 °C for the pure PC, 200 °C for the reinforced-samples) had been obtained.<sup>11</sup>

For the physical aging tests, the DMA 2890 was used in creep mode with an applied stress of 0.1 MPa (during the load portions of the testing). The sample was first equilibrated at the test temperature (below  $T_g$ ,  $T_{\text{test}}=135$  °C for all results presented in this dissertation) for a nominal time of 10 minutes.<sup>12</sup> The chamber temperature was then increased to the rejuvenation temperature  $T_{\text{rej}}$  and held for a nominal length of time  $t_{\text{rej}}$ . (The two rejuvenation procedures described later in this

---

<sup>11</sup> A stark difference between the behavior of the pure and reinforced PC samples was evident in this testing procedure. Whereas tests with the pure PC were prematurely ended  $\sim 175^\circ\text{C}$  due to severe elongation of the sample caused by flow, an identical testing methodology conducted on the reinforced PC samples was able to go to 200 °C with no apparent degradation in sample geometry.

<sup>12</sup> All times describing the procedure for the physical aging tests are nominal times in that they are measured from the beginning of the temperature jump, and not once the desired temperature has been reached.

chapter are 160 °C for 10 minutes and 165 °C for 15 minutes; note that  $t_{rej}$  is always greater than the *actual* time the sample was at the rejuvenation temperature due to thermal lag effects.) Once the rejuvenation step has been completed, the sample is quenched to  $T_{test}$  by jumping the setpoint of the heater controller to the test temperature, which in effect shuts off power to the heater until  $T_{test}$  was reached via ambient cooling.<sup>13</sup> At the start of the quench step the aging time is set to zero; load/unload tests were then conducted at an initial aging time of 22.5 minutes and then repeated at 3/4, 1.5, 3, 6, and 12 hours as outlined in Figure 45. Because it took approximately five minutes for the DMA chamber to establish equilibrium at  $T_{test}$ , the data collected at 22.5 minutes was not included in our analysis below (due to nonisothermal aging effects). A preload of 0.01N was maintained on the sample throughout both the load and unload portions of the test.

---

<sup>13</sup> Initial tests were also conducted using a liquid nitrogen cooling accessory, purchased from the DMA manufacturer, during the quench phase of the test. However, because the time to quench was only slightly faster using the liquid nitrogen accessory (approximately 3 minutes using the liquid nitrogen accessory versus 5 minutes by effectively shutting off power to the heater), the liquid nitrogen accessory was not used during the quench steps.

## Glass Transition Temperature for Nanotube-reinforced Polycarbonate

Perhaps the most straightforward manner to evaluate changes in viscoelastic behavior is to measure the glass transition temperature of a sample using the constant frequency-constant amplitude temperature scan method outlined earlier in this chapter. Using this procedure, the storage and loss moduli and the loss tangent of the material are measured as a function of temperature; the results of such scans on the blank and NT-reinforced polycarbonate systems are shown in Figure 54-Figure 56, respectively.

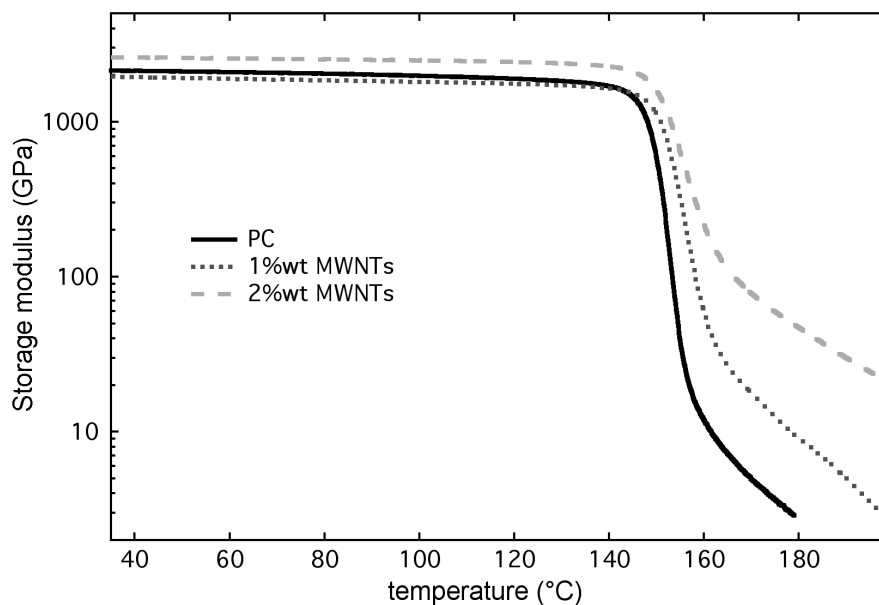


**Figure 54. Storage moduli as a function of temperature for PC samples.**

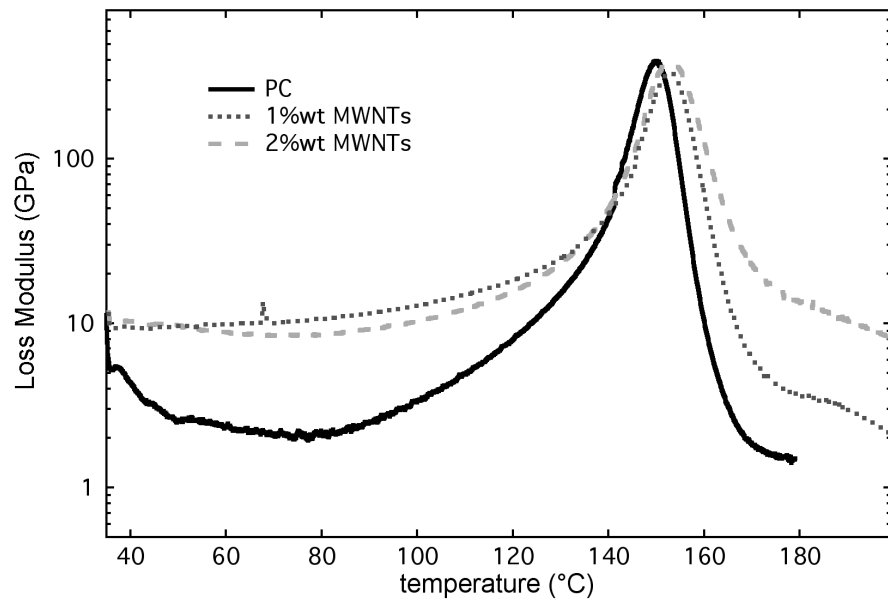


**Figure 55. Loss moduli as a function of temperature for PC samples.**

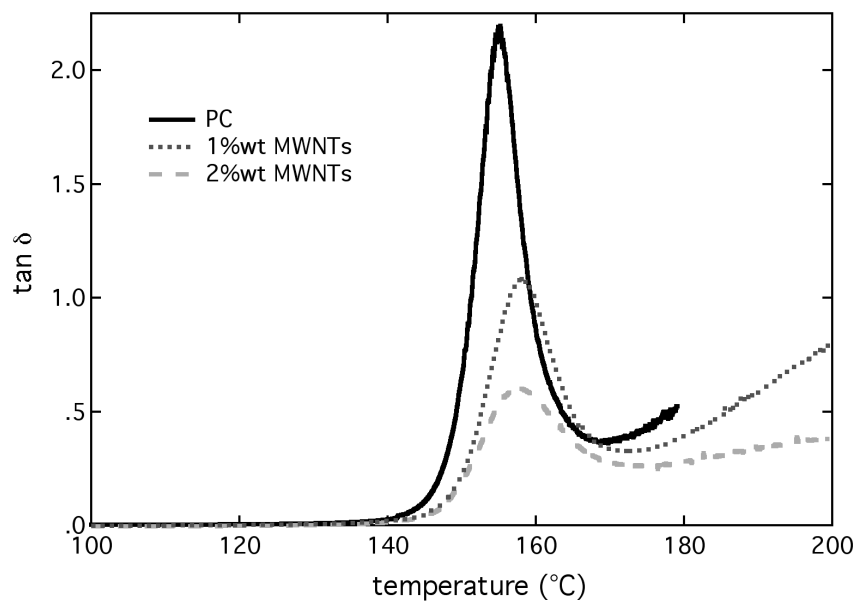


**Figure 56. Loss tangent as a function of temperature for PC samples.**

	<b>E' at 60 °C (MPa)</b>	<b>E' at 180 °C (MPa)</b>	<b>T<sub>g</sub> from E'' (°C)</b>	<b>T<sub>g</sub> from tan <math>\delta</math> (°C)<sup>14</sup></b>
<b>PC</b>	2090	2.9	150.0	155.2
<b>1% MWNT</b>	1954	9.2	152.6	158.3
<b>2% MWNT</b>	2640	47.6	152.3	157.3

**Table 9. Comparison of storage moduli and glass transition temperatures for polycarbonate-based samples.**

In Figure 54 we see an increase in the storage modulus for the 2 wt% MWNT sample, when compared to the response of the pure polycarbonate sample, at both low and high temperatures. While a similar improvement is not seen with the 1 wt% MWNT sample at low temperatures, we see that the high temperature (above  $T_g$ ) storage modulus of the sample is also greatly enhanced. (Because of the large modulus increase at higher temperatures, we believe that this slight decrease in storage modulus at low temperatures is due to experimental error.) Storage moduli values for each sample at temperatures of 60 °C and 180 °C are compared in Table 9. As discussed earlier, this drastic improvement in high temperature properties has also been identified in the literature.

Both the loss moduli (Figure 55) and loss tangent (Figure 56) curves show slight shifting of the peak location upon the addition of nanotubes. (It is unclear at this

---

<sup>14</sup> The peak of the loss tangent curve is typically a few degrees greater than the location of the peak in the loss moduli data.

time why the shift for 1 wt% MWNT is slightly larger than that for the 2 wt% sample, and replicate sample testing has not been possible in order to verify this result. This anomaly will be investigated in future experiments.) Also evident is a slight broadening of the peaks of these curves, which is most apparent in the loss tangent data in Figure 56 (which is plotted over a smaller temperature range from 100 to 200°C). As discussed previously, we believe that this broadening is indicative of an increase in the range of molecular mobility within the system. Because this broadening seems to predominantly occur on the high temperature side of the peaks, this suggests that the NTs are reducing the molecular mobility of certain polymer regions within the NRP. This is consistent with our hypothesis of a reduced mobility interphase region surrounding the nanotube. In Figure 56, we also see a decrease in the magnitude of the peaks of the loss tangent curves, which is due to the reduced fraction of bulk polymer within the material. Note that the maximum value of the loss tangent decreases by a factor of 2 with the addition of 1 wt% MWNTs, and then decreases by another factor of 2 for the 2 wt% sample.

While the slight shift in  $T_g$  and the broadening of the loss modulus peaks (on the high temperature side) are qualitatively sensible based on our hypothesis of a reduced mobility polymer phase surrounding the nanotubes, quantitative predictive models of how the mobility of the polymer chains influences the glass transition temperature do not exist. Thus we were led to investigate the relaxation spectra of the

NRP and the physical aging characteristics of the material. The results from these areas of investigations are presented below.

## **Frequency- and Time-Domain Response of Nanotube-reinforced Polycarbonate**

Dynamic mechanical analysis was also used to study the frequency-domain response of the polycarbonate-samples. Such tests provide another means with which to analyze the impact of the embedded nanotubes on the effective viscoelastic properties of the NRP. Frequency domain analysis lends itself quite nicely to micromechanical modeling of the effective response, which is accomplished by using appropriate elasticity solutions transformed into the frequency domain via the Dynamic Correspondence Principle. The specifics of the data collection techniques used to obtain the frequency domain data were discussed earlier in this chapter.

After describing the analysis of the frequency domain data and discussing the various responses (frequency domain, time domain, and relaxation spectrum) that we have obtained for the samples, we will demonstrate a frequency-domain micromechanical modeling approach using the Mori-Tanaka solution for a three dimensional random orientation of inclusions. By modeling the viscoelastic behavior of the interphase region as simply a change in the relaxation times of the bulk

polycarbonate response, via the mobility parameter  $\beta$ , it is possible to infer the behavior of this non-bulk polymer phase from experimental data obtained via macroscale mechanical testing of the bulk and reinforced polycarbonate samples. Such a model will be useful in interpreting experimental stiffness data obtained for nanotube-reinforced polymers and assessing changes in the mobility and mechanical behavior of the interphase region.

### ***Analysis of frequency-domain data***

Initial complex moduli data were collected over a range of frequencies (limited by the 0.01 to 200 Hz frequency range of the DMA machine) for temperatures ranging from approximately  $T_g - 50$  °C to  $T_g + 50$  °C. Then using the principle of time-temperature superposition, the moduli at different temperatures were shifted to form a reference curve at 150°C. Time-temperature superposition was carried out using software provided by the DMA manufacturer (TA Instruments, Thermal Analysis<sup>®</sup>), and a single temperature shift factor  $a_T$  chosen to provide the best fit for *both* storage and loss moduli data at a given temperature. An example of the raw data collected for a pure polycarbonate sample and shifted appropriately is shown in Figure 57. The nature of the anomalous behavior of the loss moduli curves at high frequencies is unknown but has been seen in the literature (Ferry 1980). Interestingly, most references to frequency-domain time-temperature superposition only consider the

storage modulus, and thus the behavior evident here is not typically discussed in the literature. In order to eliminate this behavior from our subsequent analysis, we will limit the upper frequency in our analysis to  $10^5$  Hz. Further investigation of this phenomena is warranted.

At this step in the analysis the storage and loss moduli data were fit to a 30-term Prony series using a linear least squares solver DYNAMFIT developed at Northwestern (Bradshaw and Brinson 1997b). The program assumes that the relaxation times  $\tau_j$  are equally spaced in log time, and then calculates the Prony coefficients  $E_0$  and  $E_j$  which best fit the data, equally weighing storage and loss moduli contributions to the root mean square error (rms) of the solution. An extra constraint imposed within the code forces all Prony coefficients  $E_j$  to be greater than zero; while such a constraint does slightly increase the rms error describing the fit, negative Prony coefficients are not physically reasonable and thus were not considered. Typical rms values for the Prony series curve fit were under 10%, and usually within 0.2% of the rms value for the Prony series fit which did not include the positive coefficient constraint.

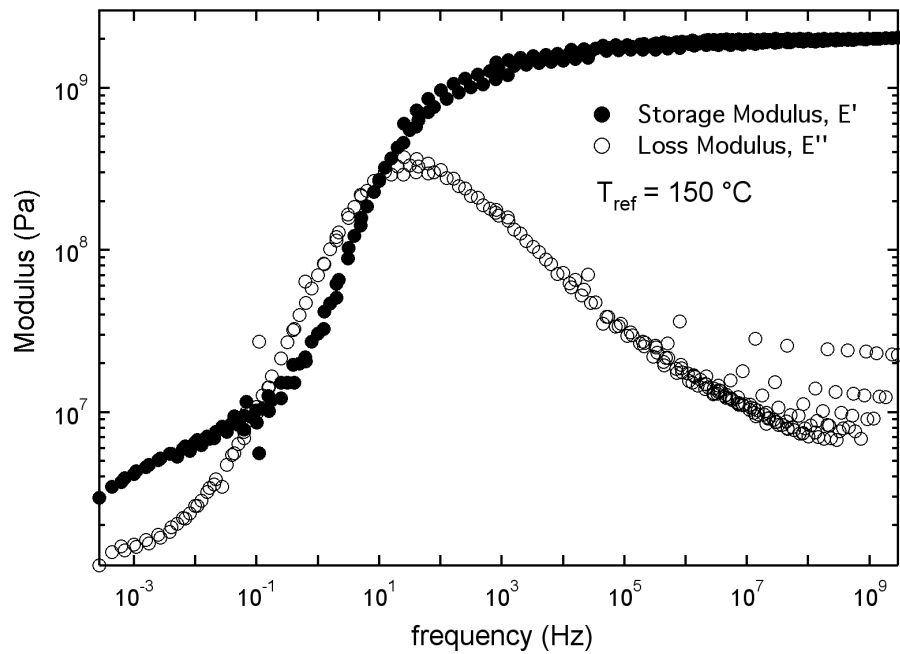


**Figure 57. Time-temperature shifted frequency-domain experimental data for a pure polycarbonate sample.**

An example of the Prony series fit to the experimental data for the case of pure polycarbonate (to a maximum frequency of  $10^5$ ) is shown in Figure 58. Once the Prony series terms have been obtained from the frequency-domain experimental data, the corresponding time-domain response and relaxation spectrum can be readily determined. The viscoelastic behavior for the blank and reinforced polycarbonate samples was characterized using this procedure and is described below.

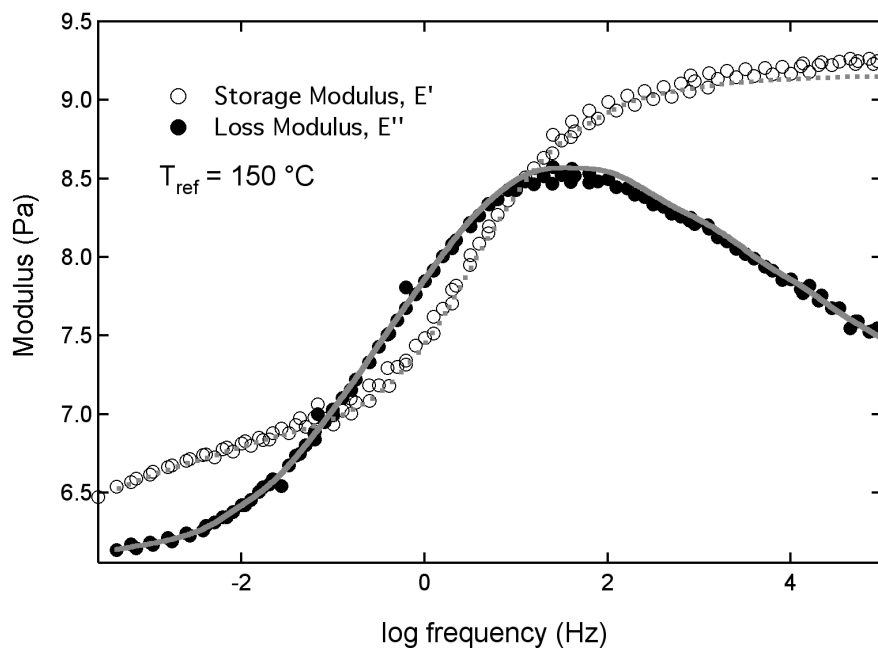


**Figure 58. Prony series representation of the frequency domain data.**

### *Experimental time and frequency domain response*

Using the procedure outlined above, the shifted storage and loss moduli of the polycarbonate samples as a function of frequency for a reference temperature of 150°C are shown in Figure 59 and Figure 60, respectively. The corresponding time response of the samples, predicted based on the Prony series coefficients found from analysis of frequency domain data, is shown in Figure 61. Similar to the results obtained in the temperature scan experiments, we see a large increase in the low frequency storage modulus (and a corresponding increase in  $E(t)$  at long times) with the use of the carbon nanotubes as a filler phase. The peaks of the loss modulus curves

are slightly shifted to higher frequencies as the percentage of nanotubes is increased, which is characteristic of a reduction in the effective molecular mobility of the sample.

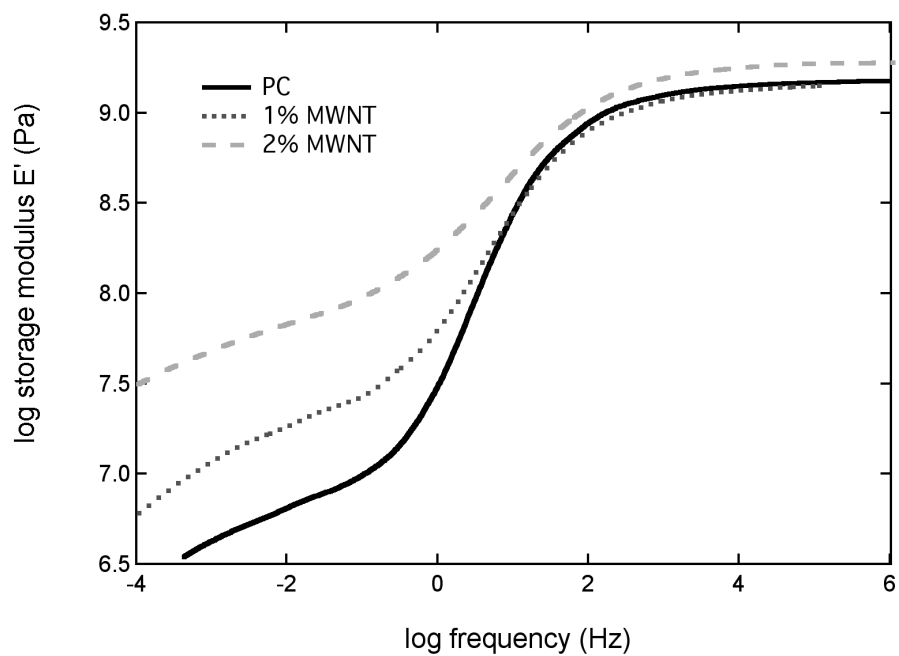


**Figure 59.** Frequency domain storage modulus for PC samples.  $T_{\text{ref}} = 150^{\circ}\text{C}$ .

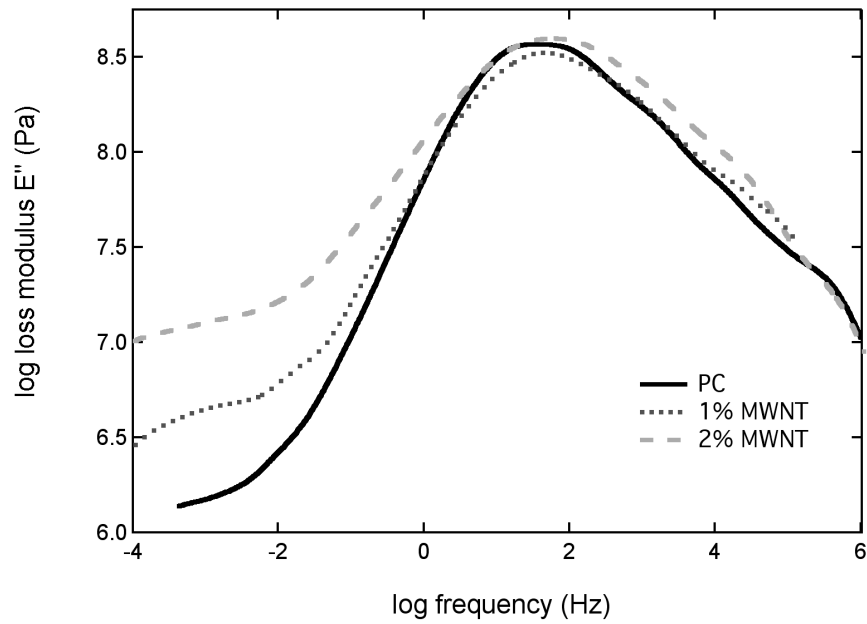


**Figure 60. Frequency domain loss modulus for PC samples.  $T_{ref} = 150^{\circ}\text{C}$ .**

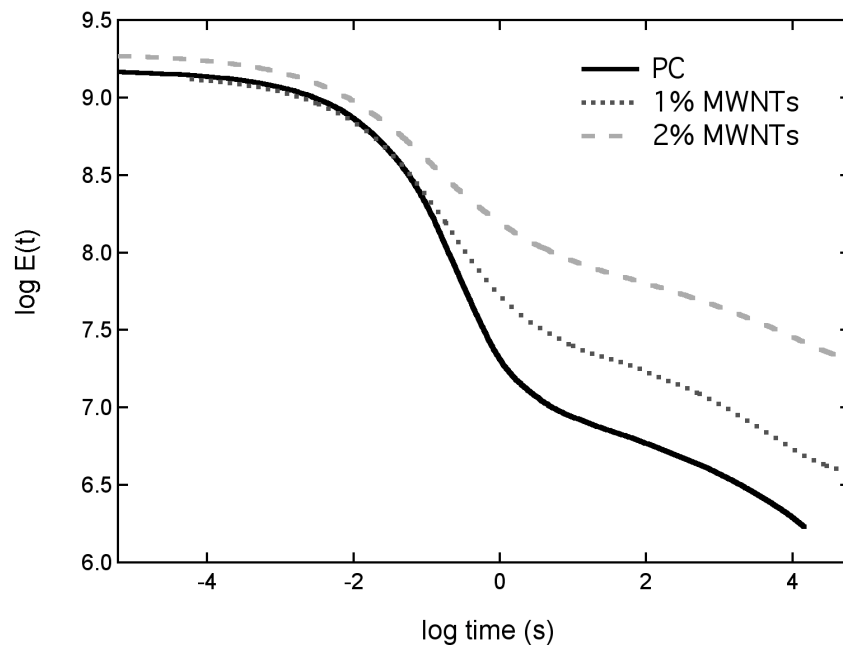


**Figure 61. Time domain response for PC samples.  $T_{ref} = 150^{\circ}\text{C}$ .**

The relaxation spectra for the blank and reinforced polycarbonate samples are shown in Figure 62. Here we see an increase in the relaxation spectrum at longer times with increasing nanotube volume fraction. Also apparent is a slight broadening of the primary relaxation peak towards longer times. The broadening of the primary relaxation peak and the increase in the relaxation spectrum at longer times are both indicative of an increased number of relaxation modes and the introduction of longer time relaxation processes within the reinforced samples. These changes are consistent with the hypothesis of a reduction in molecular mobility within the interphase. Meanwhile, the location of the primary relaxation peak does not appreciably change with the addition of the nanotubes, suggesting that the primary relaxation mechanism within the NRP is the same as that within the bulk polymer sample. This is yet more evidence that the nanotubes *only* reduce the molecular mobility of the interphase region, and that polymer chains well separated from the nanotubes are not affected by the presence of the nanotubes and retain the mobility of the bulk polymer sample. These results are consistent with the three phase (NT-interphase-polymer) model presented in Figure 42.

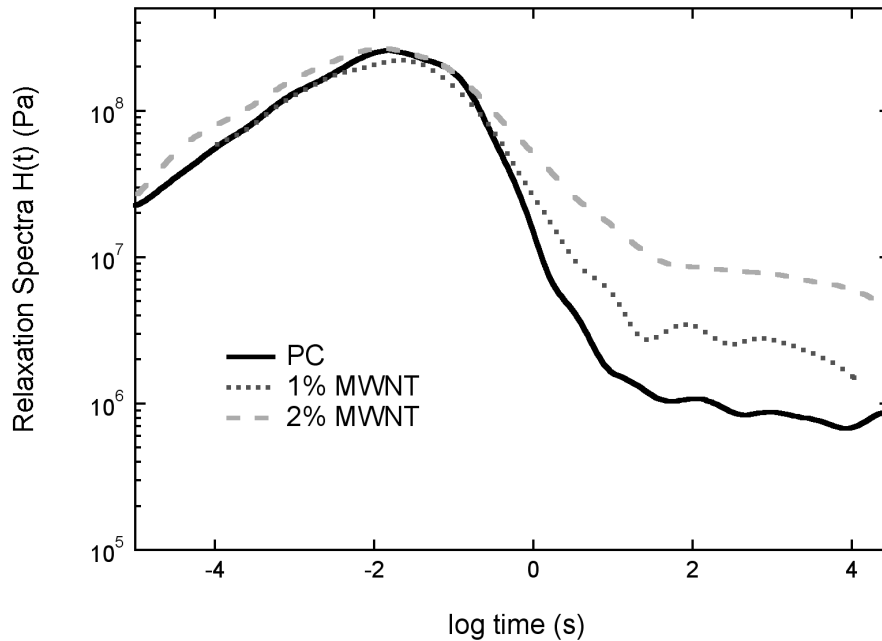


**Figure 62. Relaxation spectra for PC samples.  $T_{\text{ref}} = 150^{\circ}\text{C}$ .**

### ***Micromechanical modeling of NRP frequency domain behavior***

One of the advantages of analyzing the frequency domain response of nanotube-reinforced polymers is that micromechanical models are available for the analysis and interpretation of results. This is accomplished by use of the Dynamic Correspondence Principle, which allows suitable elasticity solutions to be extended for the study of viscoelastic materials. One can show that there is a direct analogy between elasticity problems in the time domain and viscoelasticity problems in the frequency domain when the elastic moduli are replaced by their corresponding complex viscoelastic moduli of the form  $\bar{E}^* = E' - iE''$ , and associated field quantities

are allowed to be complex (Hashin 1965; Hashin 1970; Fisher 1998). Thus the Mori-Tanaka solution for a multiphase composite with viscoelastic phase materials can be written as (see Chapter 3)

$$\bar{\mathbf{L}}^* = \sum_{r=1}^N c_r \left\{ \bar{\mathbf{L}}_r^* \bar{\mathbf{A}}_r^* \right\} + c_0 \bar{\mathbf{L}}_0^* \sum_{r=0}^N c_r \left\{ \bar{\mathbf{A}}_r^* \right\} \quad (73)$$

The dynamic correspondence principle has been used by a variety of researchers to model the viscoelastic behavior of materials, and in particular has been used in conjunction with the Mori-Tanaka method to look at the effective viscoelastic moduli of a three phase composite with viscoelastic interphase and matrix phases (Fisher 1998; Fisher and Brinson 2001). As shown in Figure 63, the viscoelastic Mori-Tanaka model closely follows the results of a corresponding viscoelastic finite element model for the effective storage and loss transverse modulus of a 60% fiber-10% interphase-30% matrix unidirectional composite (Fisher and Brinson 2001). Particularly encouraging is the relative agreement between the two solutions within the transition region. Based on this result we feel that the use of a viscoelastic implementation of the Mori-Tanaka method is warranted.<sup>15</sup>

---

<sup>15</sup> Note that in Figure 63 the viscoelastic behavior of the interphase and matrix material were described by two distinct sets of Prony series coefficients (Fisher 1998).

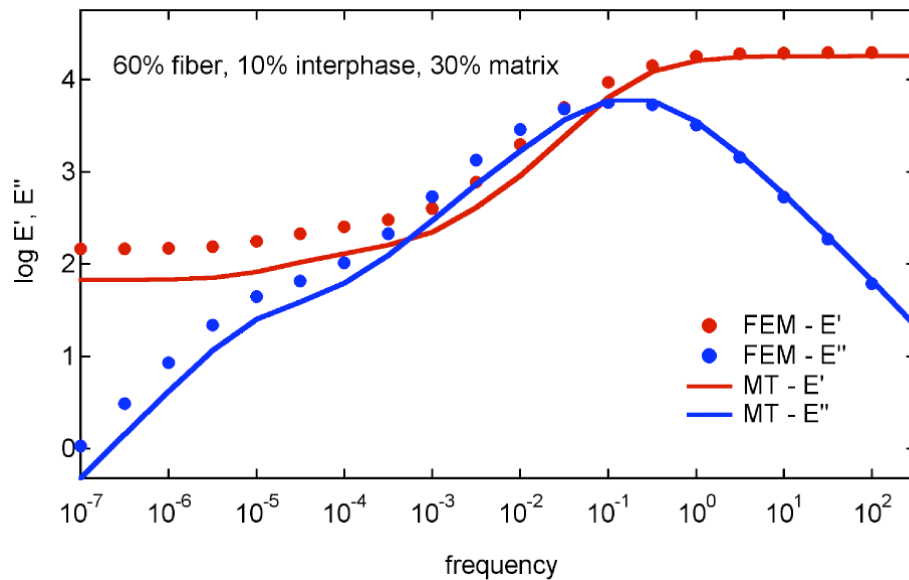


**Figure 63. Comparison of Mori-Tanaka and finite element solutions for the transverse modulus of a three phase unidirectional composite with viscoelastic interphase and matrix phases. (Fisher 1998)**

Initial micromechanical modeling results for the effective frequency domain response for the 2 wt% nanotube-reinforced polycarbonate samples are shown in Figure 64 and Figure 65. For the NRP composite, the viscoelastic matrix properties were assumed equal to those obtained for the bulk polycarbonate samples tested, and a 3D random orientation of NTs was assumed. The interphase volume fraction was chosen through a process of trial and error as 10%, and the interphase viscoelastic response was modeled as a simple shift in relaxation times of the pure polymer using the mobility parameter  $\eta=1000$  (also found through trial and error). For each of the NRP samples, the volume fraction of the nanotubes was assumed to be known (based

on the weight fraction of embedded nanotubes), and a nanotube (elastic) modulus of 200 GPa was chosen by fitting the high frequency portion of the Mori-Tanaka effective storage modulus to the experimental storage modulus of the NRP (see Figure 65).<sup>16</sup>

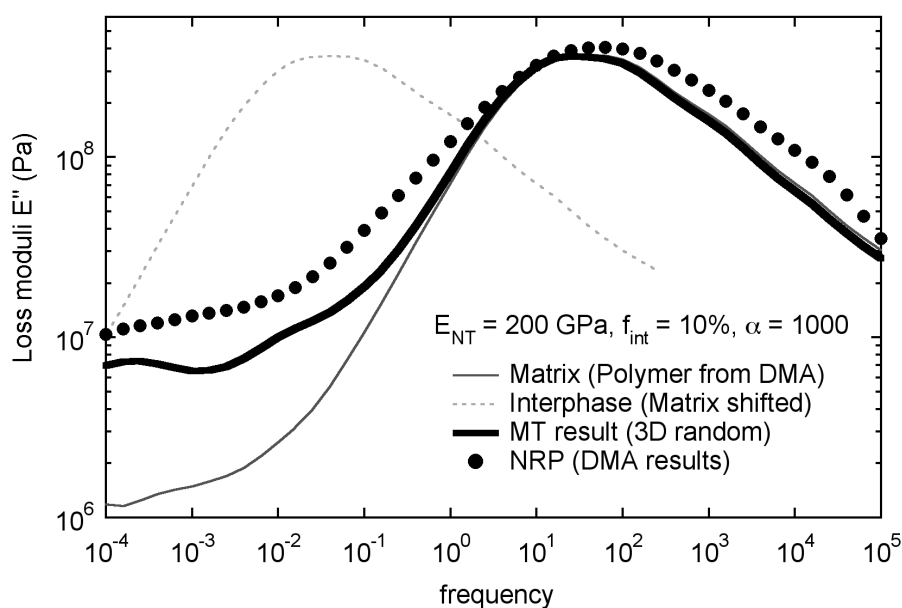


**Figure 64. Mori-Tanaka prediction for 2% MWNT sample loss modulus, assuming  $f_{\text{int}}=10\%$  and  $\alpha=1000$ .**

---

<sup>16</sup> A general rule of thumb for the conversion of weight fraction to volume fraction of nanotubes is to divide by a factor of two. This approximation was used here as the exact relationship between the densities of the nanotubes and the polymer was not known.

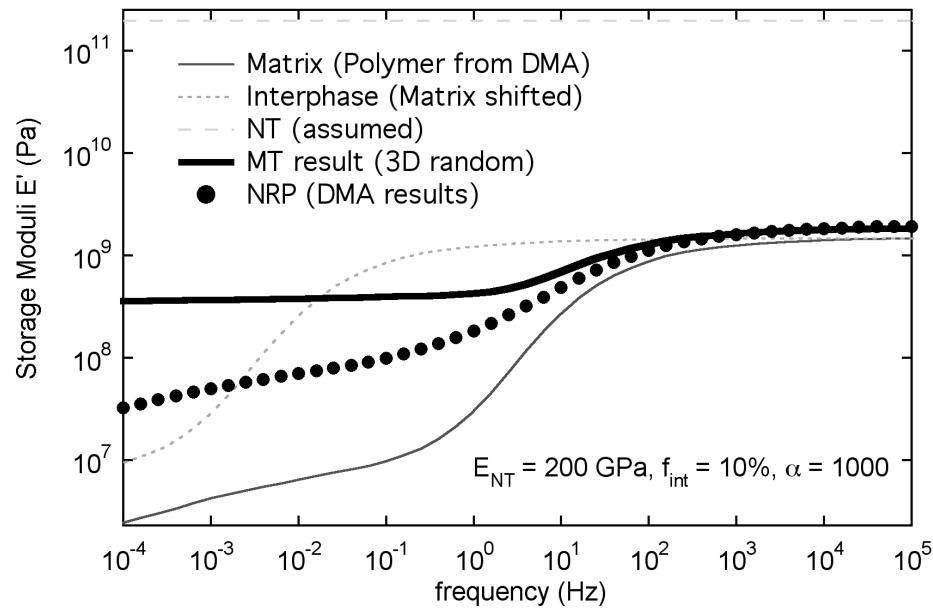


**Figure 65. Mori-Tanaka prediction for 2% MWNT sample storage modulus, assuming  $f_{int}=10\%$  and  $\alpha=1000$ .**

We are most interested in comparing the micromechanical solution with the experimental data for the loss modulus of the material, as the mechanical properties of the (elastic) nanotube should not factor in this analysis. In Figure 64, a comparison of the Mori-Tanaka prediction with the experimental NRP data for the effective loss modulus shows that qualitative agreement between the two is obtained when using an interphase volume fraction of 10% and a mobility parameter  $\alpha=1000$ . We are particularly interested in the low frequency response of the loss modulus, where the micromechanical predictions increase from that of the pure polymer and approach the NRP experimental data as the  $\alpha$  increases. (For comparison, Figure 66 shows the

Mori-Tanaka prediction for  $\eta=100$ .) Referring to Figure 65, we see that the Mori-Tanaka solution over-predicts (by an order of magnitude) the low frequency effective NRP *storage* modulus that was measured experimentally. This is directly related to the difficulties in predicting the elastic properties of NRPs using micromechanical methods. As discussed in Chapter 3, these over-predictions could be due to a number of factors, including poor NT-polymer interfacial behavior, inadequate NT dispersion, and embedded nanotube waviness.

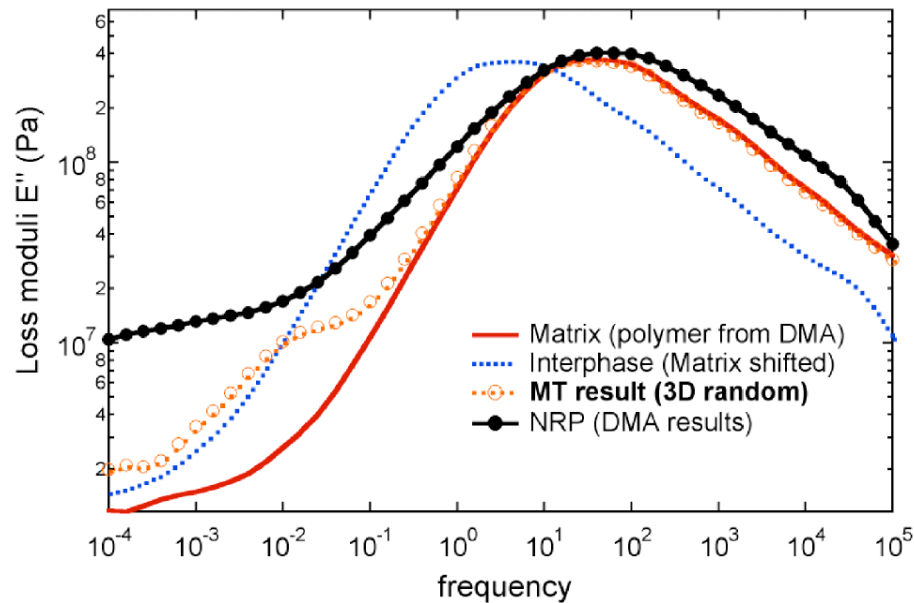


**Figure 66. Mori-Tanaka prediction for 2% MWNT sample loss modulus, assuming  $f_{int}=10\%$  and  $\eta=100$ .**

Figure 67 compares the Mori-Tanaka prediction and the experimental data for the effective loss modulus for the 1% MWNT-PC sample. Using the same values for the interphase volume fraction (10%) and the mobility parameter  $\mu$  ( $=1000$ ), we again see very good qualitative agreement between the Mori-Tanaka model and the experimental data.

These initial modeling efforts are illustrative of the future research directions for this work. As more data is collected, we will seek to fit the volume fraction and viscoelastic behavior of the interphase to experimental data collected over a range of nanotube volume fractions using the procedure demonstrated briefly above. However, the initial work presented here demonstrates that the impact of the nanotubes on the effective viscoelastic behavior of the NRP can be modeled using a three-phase Mori-Tanaka model. Furthermore, given the simple model of the interphase viscoelastic properties used here, we see that a relatively large volume fraction of interphase (10%) with significantly reduced mobility (three orders of magnitude) provides qualitative agreement between our micromechanical model predictions and the experimentally obtained data. Eventually, we foresee basing models of the interphase viscoelastic properties on nanoscale experimental data and/or molecular dynamics simulations of the NT-polymer system.

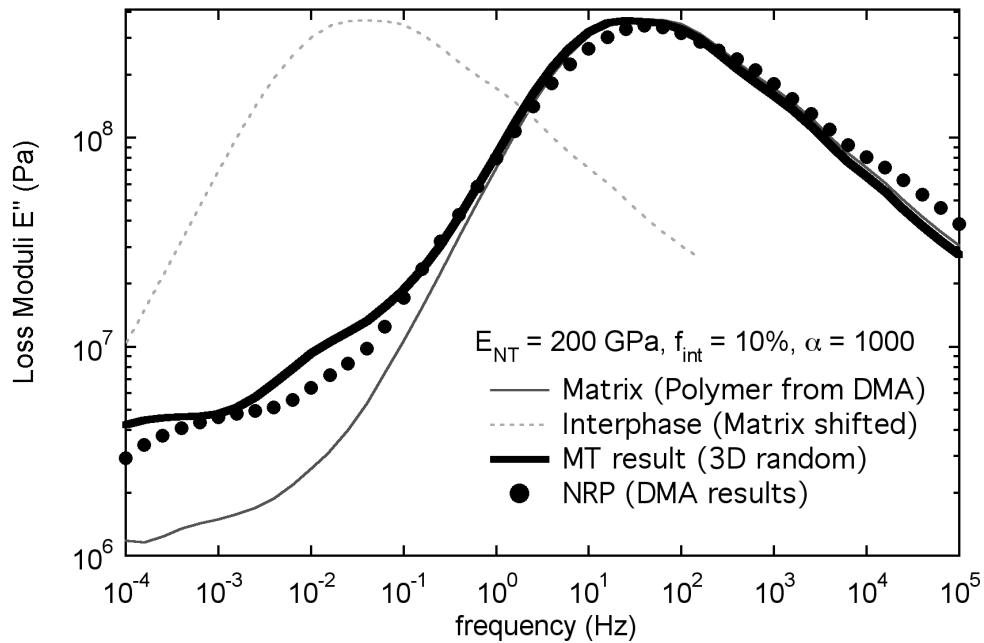


**Figure 67. Mori-Tanaka prediction for 1% MWNT sample loss modulus, assuming  $f_{int}=10\%$  and  $\alpha=1000$ .**

## Physical Aging of Nanotube-reinforced Polycarbonate

Physical aging tests were conducted on both blank and nanotube-reinforced polycarbonate samples to ascertain the effect of the nanotubes on the effective physical aging characteristics of the material. The experimental procedure used to conduct the physical aging tests was described earlier in this chapter. An isothermal aging/test temperature of 135 °C was used for all tests, which is sufficiently close to the nominal  $T_g$  of the polycarbonate, such that significant aging affects will take place over relatively short periods of time.

Two sets of rejuvenation parameters ( $T_{rej}$ ,  $t_{rej}$ ) were used in this work: 160 °C for 10 minutes and 165 °C for 15 minutes. The higher temperature / longer time rejuvenation procedure was used after initial tests on samples rejuvenated at the lower  $T_{rej}$  showed evidence that full rejuvenation (i.e. a full erasure of previous thermal history) was not achieved under these conditions. We believe this to be the case because shift rates much smaller than one were obtained based on an analysis of the experimental data. In all cases, shift rates decreased as the weight fraction of the nanotubes increased.

Momentary creep compliance curves, and their shifting to form a master reference curve at the longest aging time, for a blank polycarbonate sample rejuvenated at 165 °C for 15 minutes were shown in Figure 46 and Figure 47, respectively. Corresponding plots for the 2% MWNT-PC samples tested using the same rejuvenation procedure are shown in Figure 68 and Figure 69. As expected, the compliance values of the 2% MWNT-PC sample are smaller than those for the blank PC, indicating a stiffer (higher modulus) response for the reinforced samples.

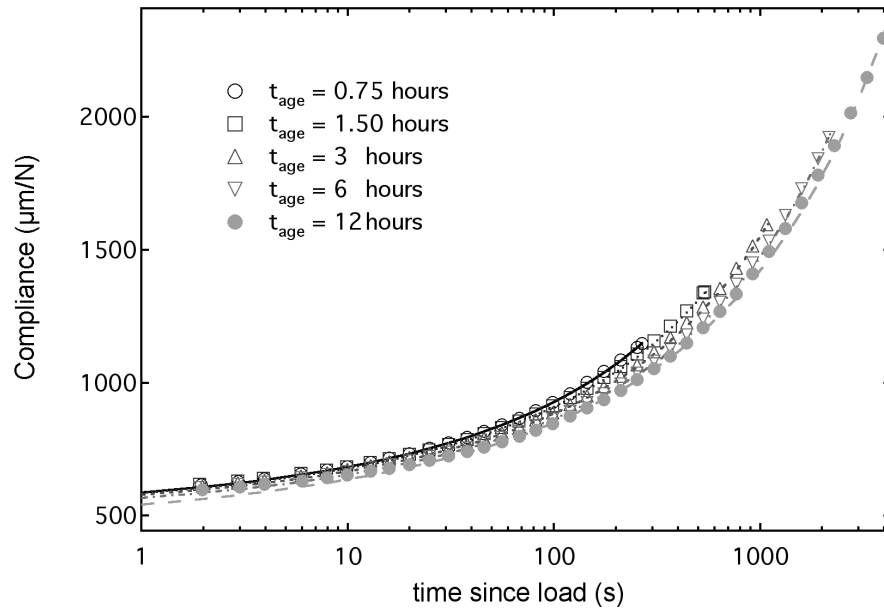


**Figure 68. Momentary compliance curves for 2% MWNT-PC sample rejuvenated at 165 °C for 15 minutes.**

A qualitative comparison of the momentary creep compliance curves suggests that while the shapes of the curves are quite similar, the amount of shifting necessary to superpose the curves at the longest aging time (aging time shift factor  $a_{t_e}$ ) is quite different. The shift factors for the blank and NT-reinforced samples are plotted as a function of aging time in Figure 70 and Figure 71 for the each of the two rejuvenation methods (160 °C for 10 minutes and 165 °C for 15 minutes), respectively. The shift rates calculated from this data are given in Table 10.

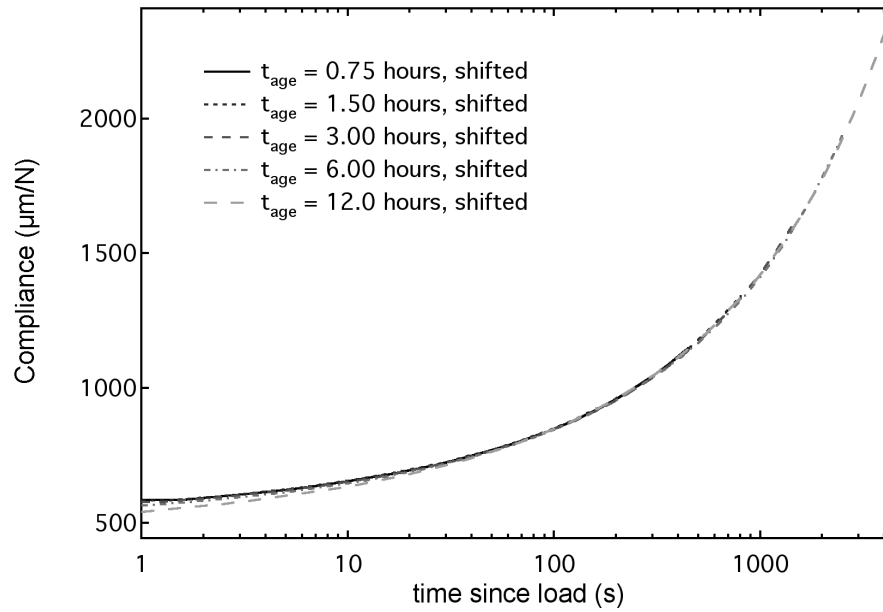


**Figure 69. Shifting of momentary compliance curves for 2% MWNT-PC sample rejuvenated at 165 °C for 15 minutes.**

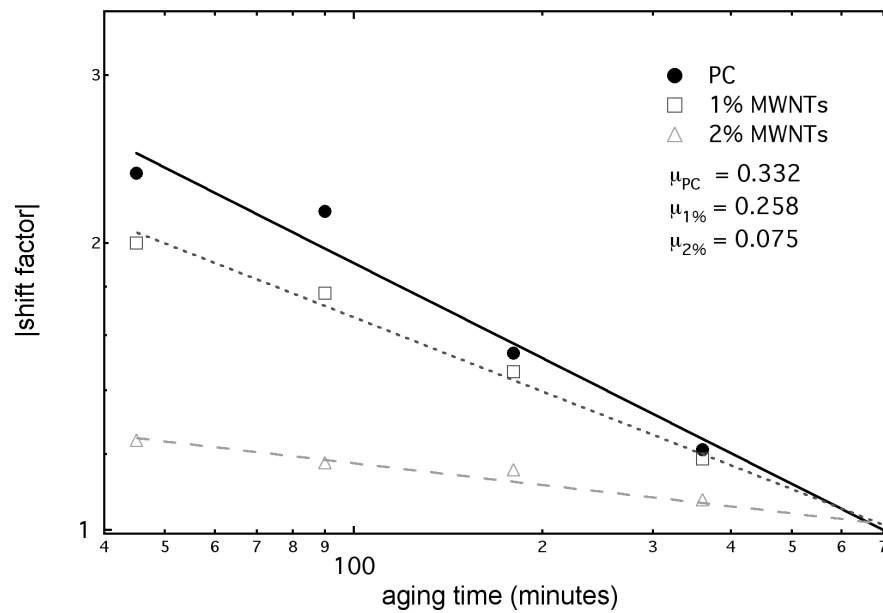


**Figure 70. Shift rate  $\mu$  for 160 °C rejuvenation for 10 minutes.**

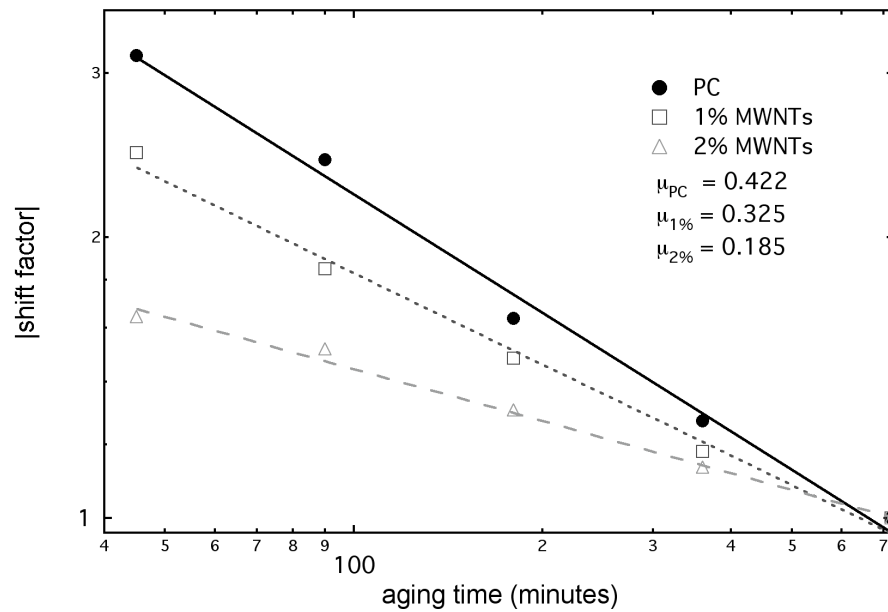


**Figure 71. Shift rate  $\mu$  for 165 °C rejuvenation for 15 minutes.**

Rejuvenation procedure	RPI PC sample	Shift rate (data)	Shift rate (PHYAGE)
160 °C for 10 minutes	Blank	0.332	0.325
	1% MWNTs	0.258	0.260
	2% MWNTs	0.075	0.082
165 °C for 15 minutes	Blank	0.422	0.405
	1% MWNTs	0.325	0.307
	2% MWNTs	0.185	0.187

**Table 10. Shift rates of blank and NT-reinforced polycarbonate samples.**

The shift rates determined for each of the samples are consistent with the hypothesis that the effective mobility of the nanotube-reinforced samples is more restricted than that measured for the pure polycarbonate.<sup>17</sup> As the weight fraction of nanotubes (and thus the volume of the interphase region) increases, the effective shift rates of the material (for a given rejuvenation procedure) decrease. From the standpoint of free volume, this can be viewed as the NRP samples requiring longer periods of time for the molecular rearrangements that lead to physical aging to occur. The fact that the shift rates obtained for the higher temperature / longer time rejuvenation are greater than those obtained for the lower temperature rejuvenation suggests that the former erased “more” of the prior thermal history of the sample. However, because these experimental shift rates are still much lower than unity, we believe that full rejuvenation of the samples (particularly the nanotube-reinforced samples) may not have been achieved. Optimal rejuvenation parameters for these samples will be the subject of future work. Nonetheless, the following conclusions can be drawn based on the physical aging tests conducted to date:

---

<sup>17</sup> At this moment it is impossible to rule out the possibility that the differences in rejuvenation is solely caused by the change in effective  $T_g$  of the material due to the presence of the nanotubes. Once a full rejuvenation protocol has been established, we will be able to analyze this possibility in greater detail. Nonetheless, we anticipate that the embedded nanotubes will result in different physical aging behavior between the blank and NT-reinforced samples.

- The embedded nanotubes significantly influence the rejuvenation of the polycarbonate samples,
- Shift rates for (partially) rejuvenated samples decrease as the weight fraction of nanotubes increase; we attribute this to an interphase region surrounding the nanotubes,
- The shift rate behavior can be described qualitatively using the concept of a reduced mobility, non-bulk polymer interphase region,
- This reduced mobility interphase region is consistent with the results of other viscoelastic testing ( $T_g$  and relaxation spectra) that have been measured for these same polycarbonate-based samples, and
- These results suggest that changes in the physical aging behavior of the NRP may be sensitive to changes in molecular mobility, such that physical aging studies may be useful in evaluating such changes in nanotube-reinforced polymer systems.

Currently we are in the process of re-evaluating the rejuvenation procedure in order to develop a protocol which completely erases the thermal history of the samples, without compromising the structure or properties of the samples. Once this has been completed, physical aging tests will be re-run on each of the samples described in this work, as well as additional samples with other weight fractions of

nanotubes which we hope to receive shortly. Based on the preliminary physical aging results presented here, we feel that the nanotubes will significantly alter the aging characteristics of the NRP (with respect to the pure polymer), and as such appreciably impact the long-term viscoelastic behavior of the NRP.

## **Summary**

We have compared the effective viscoelastic response of pure and nanotube-reinforced polycarbonate samples using dynamic mechanical analysis. Three types of viscoelastic behavior were analyzed: the glass transition temperature, the frequency response, and physical aging. The results of each of these tests demonstrate that the effective viscoelastic behavior of the nanotube-reinforced polymer is consistent with the hypothesis that a reduced mobility, non-bulk polymer interphase forms in the region surrounding the nanotube. This reduction in mobility is believed to be due to the nanostructure of the NRP, and is attributed to interactions between the polymer chains and the nanotubes.

Preliminary micromechanical modeling suggests that this interphase region may be quite large (several times the volume fraction of the nanotubes) and have viscoelastic properties quite different from those of the bulk polymer (a three order of magnitude shift in relaxation times using the simple model described here). While

such modeling may assist in the interpretation of experimental data, the utility of the predictions are limited due to the number of assumptions that are implicit within the model. In the next chapter we will discuss proposed future experiments on a novel nanotube-reinforced polymer system, based on an ordered and uniform carbon nanotube array. The promise of such a system is that the large degree of control with respect to the composite geometry greatly simplifies the mechanical modeling of the effective response.

## **CHAPTER 5: CONCLUSIONS AND FUTURE WORK**

### **Summary**

Theoretical predictions of the mechanical properties of carbon nanotubes, and in particular their predicted high strengths (on the order of 60 GPa) and moduli (~1 TPa), make them attractive candidates as a reinforcement filler material in polymer-based structural composites. Recent experimental testing of individual nanotubes and nanotube bundles has verified these predictions. In addition, their outstanding electrical and thermal properties suggest that carbon nanotubes incorporated into polymers can significantly enhance these properties as well. The possibility of multifunctional composite materials with controllable electrical and thermal properties, in addition to order-of-magnitude enhancements in the mechanical behavior, has resulted in a tremendous amount of work dedicated to these material systems within the last few years.

Initial experimental work on carbon nanotube-reinforced polymers has demonstrated that large increases in effective moduli and strength can be attained with the addition of small amounts of carbon nanotubes. However, modeling the effective properties of a nanotube-reinforced polymer is made difficult because of complexities

related to: the structure and properties of the nanotubes, the orientation and dispersion of the nanotubes within the polymer, the characteristics of the interface and load transfer between the NTs and the polymer, and an understanding of the impact of the nanotubes on the molecular mobility of the polymer chains. Accurate models of how these issues influence the effective properties of the nanotube-reinforced polymer will be necessary in order to optimize the fabrication and effective properties of nanotube-polymer systems.

Modeling of NRP effective behavior is complicated by the range of length scales characteristic of these materials. It will be necessary for models developed at these different length scales, from atomistic simulations to continuum theories, to work in concert to accurately model the NRP mechanical response. Such an approach is demonstrated in this work, where we have sought to extend traditional micromechanics and viscoelastic models of composite and polymer behavior to account for nanoscale characteristics of these materials.

Two models have been developed in this dissertation as a means to incorporate nanoscale information into predictions of macroscale effective behavior. In Chapter 3, we discussed a hybrid finite element-micromechanics method that allows one to incorporate the waviness of the embedded nanotubes into micromechanics predictions of the effective elastic moduli using a multiphase composite approach. While this procedure was demonstrated using the Mori-Tanaka method, in general this type of

analysis can be used with any micromechanical approach. The results of this work show that nanotube waviness significantly reduces the NRP effective modulus compared to predictions obtained assuming straight nanotubes.

The effective viscoelastic response of nanotube-reinforced polycarbonate was discussed in Chapter 4. Our experimental data suggests that the viscoelastic response of the NRP is significantly different from that of the bulk polymer; for all tests this difference is consistent with the presence of regions of non-bulk polymer with restricted mobility within the material. We believe that this interphase region is a direct consequence of the size scale of the nanotubes and their nanoscale interactions with the polymer chains. A second micromechanical-based model was developed to describe the impact of a reduced mobility interphase on the effective viscoelastic response of the NRP. Our results suggest that accounting for this interphase region will be critical in developing accurate models of the viscoelastic response of the NRP. Additional experimental work in this area is ongoing.

Each of the models presented in this dissertation are viewed as preliminary descriptions of the NRP effective behavior, and can be extended with the addition of nanoscale information to complement the continuum approaches used here. For example, atomistic simulations of the interface between the nanotube and the polymer and/or the mobility of polymer chains in the direct vicinity of the nanotubes will provide additional details of the nanoscale response that will influence the NRP

mechanical behavior. Experimental work at both the nano- and micro-scale will provide additional insight into the effective behavior of these systems.

One of the inherent difficulties with modeling carbon nanotube-reinforced polymers is the large number of parameters that are expected to impact the effective response of the NRP, but are currently not well understood. As discussed in Chapter 2, these issues include the dispersion and orientation of the nanotubes within the polymer, as well as an understanding of the interfacial characteristics and load transfer capabilities of a particular NT-polymer system. The work in this dissertation highlights embedded nanotube waviness and the existence/properties/extent of an interphase region surrounding the NT as two additional parameters that must also be considered. Given the complexity of modeling these systems, it would be desirable to develop experimental techniques capable of isolating a subset of these parameters for in-depth study. Such a model NRP has been proposed (Ruoff 2001) and is based on an ordered array of carbon nanotubes, which when infiltrated with a suitable polymer will yield a nanotube-reinforced polymer with highly uniform and controllable NT diameter, spacing, and alignment. This system will greatly facilitate the interpretation of experimental results, and we believe will lead to breakthroughs in our understanding of NRP behavior. This proposed avenue of future research is discussed below.

## **Aligned Carbon Nanotube Array Composites**

The development of aligned carbon nanotube array (polymer) composites will greatly facilitate experimental and theoretical work in this area. The fabrication of such systems will involve four steps:

- 1) the fabrication of porous anodic alumina (PAA) to create a well-ordered, uniform template with precise control over the pore geometries,
- 2) synthesis of carbon nanotubes via pyrolysis of hydrocarbon gases within the pores of the PAA template,
- 3) etching of the alumina substrate to partially expose one end of the nanotubes, and
- 4) infiltration of polymer as a matrix material.

This work will be a collaboration with the Ruoff group at Northwestern, and significant progress has already been demonstrated for Steps 1 and 2 above (Xu 2002b). For completeness, the steps of the fabrication process will be outlined below; further details of the procedure are described elsewhere (Xu 2002b).

As shown in Figure 72, the formation of PAA is achieved through a two-step anodization process, which has been shown to leave a well-ordered pore geometry

with controllable dimensions (Masuda, Yamada et al. 1997). The geometry of the porous structure is controlled by various parameters in the fabrication process, including the electrolyte used (pore diameter  $D$  as shown in Figure 73), the anodization voltage (interpore spacing  $d$ ), the anodization time (film thickness  $t$ ), and the reaction temperature. Pore diameters between 30-230 nm, interpore spacing between 200-460 nm, and film thickness on the order of hundreds of  $\mu\text{m}$  have been reported (Kyotani, Tsai et al. 1996; Li, Muller et al. 2000). It is anticipated that the lateral film dimensions (represented by  $w$  in Figure 73) could be 1 cm or larger (Xu 2002a).

Once a suitable template has been developed, carbon nanotubes can be grown within the pores via pyrolysis of hydrocarbon gases. Similar methods have previously been used to grow carbon nanotubes and are discussed in the literature (Kyotani, Tsai et al. 1996; Che, Lakshmi et al. 1998; Li, Papadopoulos et al. 1999). This deposition procedure has been shown to produce carbon nanotubes that closely match the geometry of the underlying template, such that well-ordered arrays of nanotubes with excellent alignment and spacing can be produced. An example of such an array is shown in Figure 74.

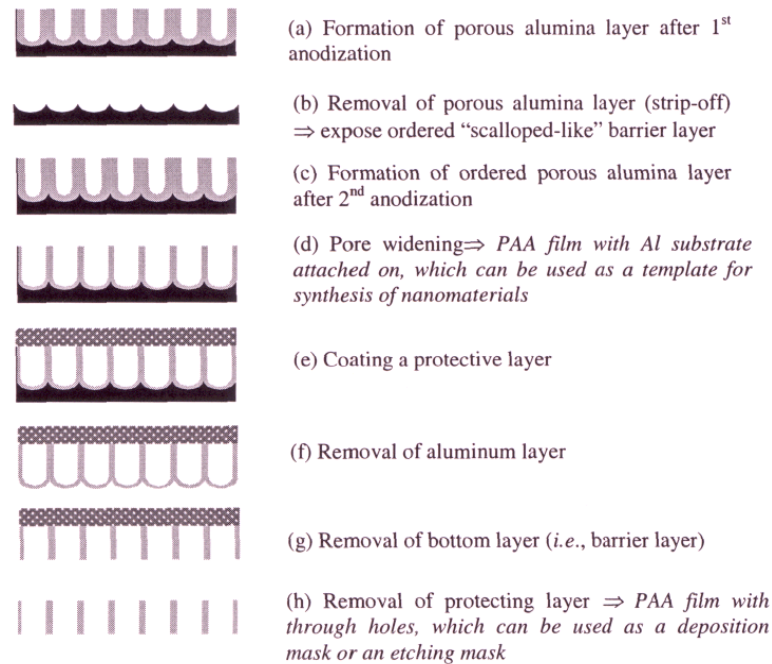


**Figure 72. Schematic of the porous anodic alumina (PAA) fabrication method (Xu 2002b).**

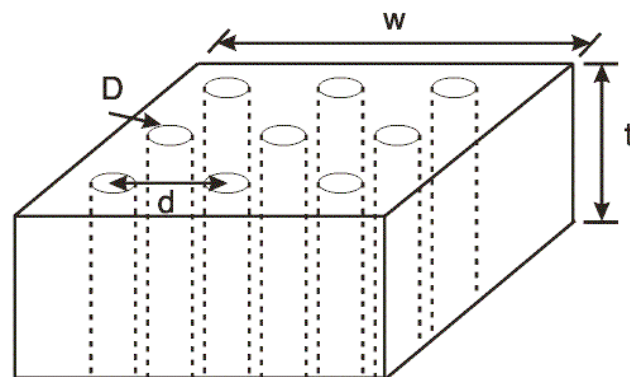


**Figure 73. Schematic illustration of the geometry of the PAA films.**

Once carbon nanotubes have been deposited in the pores of the PAA template, etching procedures can be developed to dissolve the alumina and leave free standing nanotubes (Kyotani, Tsai et al. 1996). Here, however, we wish to partially etch only one side of the alumina template, leaving a “paint-brush” geometry where the NTs are embedded within the alumina template at one and exposed at the other end. We believe that given such a structure, we can fill the empty space surrounding the exposed ends of the nanotubes with a polymer, in effecting creating a nanotube-reinforced polymer with uniform, well-ordered, and aligned nanotubes.

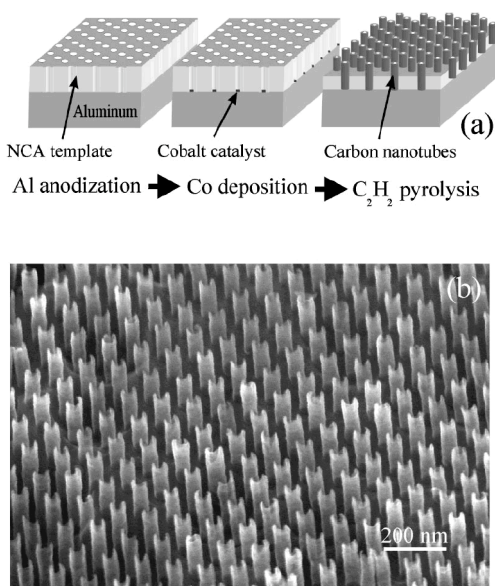


**Figure 74. Fabrication of ordered carbon nanotube arrays. (Li, Papadopoulos et al. 1999).**

The advantage of the proposed nanotube-polymer system is that it eliminates, or allows one to control, several composite parameters that are expected to influence the effective behavior of these systems. This will allow experiments to be devised to specifically isolate particular parameters for study. For example, experimental testing and modeling of the proposed ordered carbon nanotube array composites would have the following advantages:

1. The regular, aligned structure will simplify the modeling of the effective properties.
2. Control over the carbon deposition procedure will provide consistent NT properties and uniform NT geometry.
3. The geometry of the NTs will eliminate several NRP fabrication parameters, including:
  - a. orientation of the nanotubes,
  - b. dispersion of the nanotubes, and
  - c. heterogeneity of the sample.
4. The sample configuration will facilitate experiments that isolate NT- and matrix-dominated properties (see Figure 75). In particular, transverse (to the long axis of the nanotubes) tension and shear tests will be more sensitive to changes in the mechanical behavior of the interphase.

5. The geometry of the NTs will facilitate nanoscale experimentation, particularly NT pullout tests which can be done to evaluate the interfacial behavior of the material (see Figure 75).
6. Control of the interpore spacing and NT diameters will allow one to vary both the nanotube and interphase volume fractions.

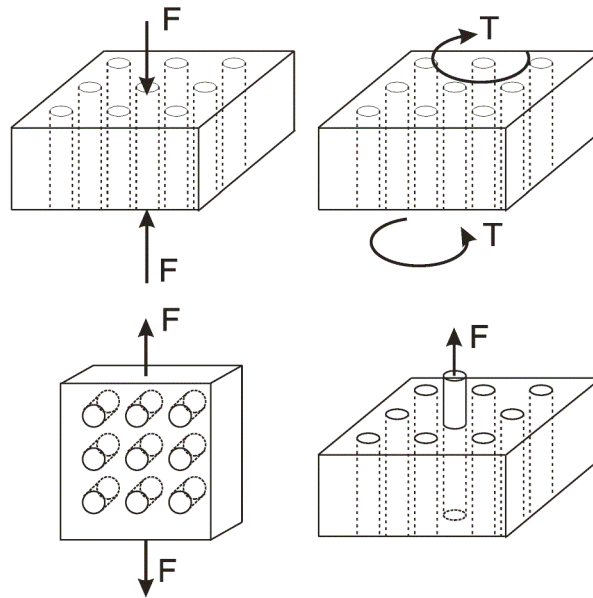


**Figure 75. Proposed experiments on the aligned carbon nanotube array composites.**

The simplifications brought about by the proposed model geometry, in conjunction with appropriately designed experiments, will lead to additional insight into the mechanical behavior of nanotube-reinforced polymers. The properties

achievable with such a composite may also be competitive from the prospective of practical applications.

## REFERENCES

- Ajayan, P., O. Stephan, C. Colliex and D. Trauth (1994). "Aligned carbon nanotube arrays formed by cutting a polymer resin-nanotube composite," *Science*, v. 265, pp. 1212-1214.
- Ajayan, P. M., L. S. Schadler, C. Giannaris and A. Rubio (2000). "Single-walled carbon nanotube-polymer composites: strength and weakness," *Advanced Materials*, v. 12(10), pp. 750-753.
- Aklonis, J. J. and W. J. MacKnight (1983). *Introduction to Polymer Viscoelasticity*. New York, John Wiley and Sons.
- Andrews, R. (2001). Private communication.
- Andrews, R., D. Jacques, M. Minot and T. Rantell (2002). "Fabrication of carbon multiwalled nanotube/polymer composites by shear mixing," *Macromolecular Materials and Engineering*, v. 287(6), pp. 395-403.
- Andrews, R., D. Jacques, A. M. Rao, F. Derbyshire, D. Qian, X. Fan, E. C. Dickey and J. Chen (1999). "Continuous production of aligned carbon nanotubes: A step closer to commercial realization," *Chemical Physics Letters*, v. 303(16), pp. 467-474.
- Barraza, H. J., F. Pompeo, E. A. O'Rear and D. E. Resasco (2002). "SWNT-filled thermoplastic and elastomeric composites prepared by miniemulsion polymerization," *Nanoletters*, v. 2(8), pp. 797-802.
- Belytschko, T., S. P. Xiao, G. C. Schatz and R. Ruoff (2002). "Atomistic simulations of nanotube fracture," *Physics Review B*, v. 65(23), pp. 235430.
- Bengu, E. and L. D. Marks (2001). "Single-walled BN nanostructures," *Physical Review Letters*, v. 86(11), pp. 2385.
- Benveniste, Y. (1987). "A new approach to the application of Mori-Tanaka's theory in composite materials," *Mechanics of Materials*, v. 6, pp. 147-157.
- Benveniste, Y., G. J. Dvorak and T. Chen (1991). "On diagonal and elastic symmetry of the approximate effective stiffness tensor of heterogeneous media," *Journal of the Mechanics and Physics of Solids*, v. 39(7), pp. 927-946.

- Biercuk, M. J., M. C. Llaguno, M. Radosavljevic, J. K. Hyun and A. T. Johnson (2002). "Carbon nanotube composites for thermal management," *Applied Physics Letters*, v. 80(15), pp. 2767-2769.
- Boresi, A., R. Schmidt and O. Sidebottom (1993). *Advanced Mechanics of Materials*. New York, John Wiley & Sons, Inc.
- Bower, C., R. Rosen, J. Lin, J. Han and O. Zhou (1999). "Deformation of carbon nanotubes in nanotube-polymer composites," *Applied Physics Letters*, v. 74(22), pp. 3317-3319.
- Bower, C., O. Zhou, W. Zhu, D. J. Werder and S. Jin (2000). "Nucleation and growth of carbon nanotubes by microwave plasma chemical vapor deposition," *Applied Physics Letters*, v. 77(17), pp. 2767-2769.
- Bradshaw, R. D. (1997). *A method of mechanical response prediction for fiber-reinforced composite laminates undergoing nonisothermal physical aging*. PhD dissertation, Northwestern University, Evanston, IL.
- Bradshaw, R. D. and L. C. Brinson (1997a). "Physical aging in polymer and polymer composites: An analysis and method for time-aging time superposition," *Polymer Engineering and Science*, v. 37, pp. 31-44.
- Bradshaw, R. D. and L. C. Brinson (1997b). "A sign control method for fitting and interconverting material functions for linearly viscoelastic materials," *Mechanics of Time-Dependent Materials*, v. 1, pp. 85-108.
- Bradshaw, R. D. and L. C. Brinson (1997c). *User's manual for PHYAGE: A data reduction program for isothermal time-aging time superposition*. Northwestern University, Evanston, IL.
- Bradshaw, R. D., F. T. Fisher and L. C. Brinson (2002). "Fiber waviness in nanotube-reinforced polymer composites: II. Modelling via numerical approximation of the dilute strain concentration tensor," *Composites Science and Technology*, submitted.
- Brechet, Y., J. Cavaille, E. Chabert, L. Chazeau, R. Dendieval, L. Flandin and C. Gauthier (2001). "Polymer based nanocomposites: Effect of filler-filler and filler-matrix interactions," *Advanced Engineering Materials*, v. 3(8), pp. 571-577.
- Brinson, L. and W. Lin (1998). "Comparison of micromechanics methods for effective properties of multiphase viscoelastic composites," *Composite Structures*, v. 41, pp. 353-367.
- Brinson, L. C. and T. S. Gates (1995). "Effects of physical aging on long term creep of polymers and polymer matrix composites," *International Journal of Solids and Structures*, v. 32(6-7), pp. 827.

- Bronikowski, M. J., P. A. Willis, D. T. Colbert, K. A. Smith and R. E. Smalley (2001). "Gas-phase production of carbon single-walled nanotubes from carbon monoxide via the HiPco process: A parametric study," *Journal of Vacuum Science Technology A*, v. 19(4), pp. 1800-1805.
- Cassell, A. M., J. A. Raymakers, J. Kong and H. Dai (1999). "Large scale CVD synthesis of single-walled carbon nanotubes," *Journal of Physical Chemistry B*, v. 103, pp. 6484-6492.
- Che, G., B. B. Lakshmi, C. R. Martin and E. R. Fisher (1998). "Chemical vapor deposition based on synthesis of carbon nanotubes and nanofibers using a template method," *Chemistry of Materials*, v. 10, pp. 260-267.
- Che, J., T. Çağın and W. Goddard III (1999). "Generalized extended empirical bond-order dependent force fields including nonbond interactions," *Theoretical Chemistry Accounts*, v. 102(346-354).
- Chen, G., M. Shaffer, D. Coleby, G. Dixon, W. Zhou, D. Fray and A. Windle (2000). "Carbon nanotube and polypyrrole composites: Coating and doping," *Advanced Materials*, v. 12(7), pp. 522-526.
- Chen, X. Q., T. Saito, H. Yamada and K. Matsushige (2001). "Aligning single-wall carbon nanotubes with an alternating-current electric field," *Applied Physics Letters*, v. 78(23), pp. 3714.
- Chou, T.-W. and K. Takahashi (1987). "Non-linear elastic behaviour of flexible fibre composites," *Composites*, v. 18(1), pp. 25-34.
- Cochet, M., W. Maser, A. Benito, M. Callejas, M. Martinez, J.-M. Beniot, J. Schreiber and O. Chauvet (2001). "Synthesis of a new polyaniline/nanotube composite: "In-situ" polymerisation and charge transfer through site-selective interaction," *Chemical Communications*, v., pp. 1450-1451.
- Collins, P. G. and P. Avouris (2000). "Nanotubes for electronics," *Scientific American*, v. December.
- Cooper, C. A., R. J. Young and M. Halsall (2001). "Investigation into the deformation of carbon nanotubes and their composites through the use of Raman spectroscopy," *Composites: Part A*, v. 32, pp. 401-411.
- Curran, S. A., P. M. Ajayan, W. J. Blau, D. L. Carroll, J. N. Coleman, A. B. Dalton, A. P. Davey, A. Drury, B. McCarthy, S. Maier and A. Strevens (1998). "A composite from poly(m-phenylenevinylene-co-2,5-dioctoxy-p-phenylenevinylene) and carbon nanotubes: A novel material for molecular optoelectronics," *Advanced Materials*, v. 10(14), pp. 1091-1093.

- Demczyk, B. G., J. Cumings, A. Zettl and R. O. Ritchie (2001). "Structure of boron nitride nanotubes," *Applied Physics Letters*, v. 78(18), pp. 2772.
- Dresselhaus, M. S., G. Dresselhaus and P. C. Eklund (1996). *Science of Fullerenes and Carbon Nanotubes*. New York, Academic Press.
- Drexler, K. E. (1992). *Nanosystems: Molecular Machinery, Manufacturing, and Computation*. New York, John Wiley & Sons, Inc.
- Ebbesen, T. W. and P. M. Ajayan (1992). "Large-scale synthesis of carbon nanotubes," *Nature*, v. 358, pp. 220.
- Endo, M. (1988). "Grow carbon fibers in the vapor-phase," *Chemtech*, v. 18, pp. 568.
- Falvo, M. R., G. J. Clary, R. M. Taylor II, V. Chi, F. P. Brooks Jr, S. Washburn and R. Superfine (1997). "Bending and buckling of carbon nanotubes under large strain," *Nature*, v. 389, pp. 582-584.
- Fan, J., M. Wan, D. Zhu, B. Chang, Z. Pan and S. Xie (1999). "Synthesis, characterizations, and physical properties of carbon nanotubes coated by conducting polypyrrole," *Journal of Applied Polymer Science*, v. 74, pp. 2605-2610.
- Ferry, J. D. (1980). *Viscoelastic Properties of Polymers*. New York, John Wiley & Sons, Inc.
- Fisher, F. T. (1998). *Viscoelastic behavior of polymer matrix composites with interphase effects: Theoretical models and finite element analysis*. MS Thesis, Northwestern University, Evanston, IL.
- Fisher, F. T., R. D. Bradshaw and L. C. Brinson (2002a). "Effects of nanotube waviness on the modulus of nanotube-reinforced polymers," *Applied Physics Letters*, v. 80(24), pp. 4647-4649.
- Fisher, F. T., R. D. Bradshaw and L. C. Brinson (2002b). "Fiber waviness in nanotube-reinforced polymer composites: I. Modulus predictions using effective nanotube properties," *Composites Science and Technology*, submitted.
- Fisher, F. T. and L. C. Brinson (2001). "Viscoelastic interphases in polymer matrix composites: Theoretical models and finite element analysis," *Composites Science and Technology*, v. 61(5), pp. 731-748.
- Fisher, F. T. and L. C. Brinson (2002). "Viscoelasticity and physical aging of carbon nanotube-reinforced polymers". Society for Experimental Mechanics, Milwaukee, WI.

- Fox, R. W. and A. T. McDonald (1992). *Introduction to Fluid Mechanics*. New York, John Wiley & Sons, Inc.
- Gao, G., T. Çagin and W. A. Goddard III (1998). "Energetics, structure, mechanical and vibrational properties of single-walled carbon nanotubes," *Nanotechnology*, v. 9, pp. 184-191.
- Gong, X., J. Liu, S. Baskaran, R. D. Voise and J. S. Young (2000). "Surfactant-assisted processing of carbon nanotube/polymer composites," *Chemistry of Materials*, v. 12, pp. 1049-1052.
- Govindjee, S. and J. Sackman (1999). "On the use of continuum mechanics to estimate the properties of nanotubes," *Solid State Communications*, v. 111, pp. 227-230.
- Grimes, C., C. Mungle, D. Kouzoudis, S. Fang and P. Eklund (2000). "The 500 MHz to 5.50 GHz complex permittivity spectra of single-wall carbon nanotube-loaded polymer composites," *Chemical Physics Letters*, v. 319, pp. 460-464.
- Hadjiev, V., M. Iliev, S. Arepalli, P. Nikolaev and B. Files (2001). "Raman scattering test of single-wall carbon nanotube composites," *Applied Physics Letters*, v. 78(21), pp. 3193-3195.
- Haggenmueller, R., H. H. Gommans, A. G. Rinzler, J. E. Fischer and K. I. Winey (2000). "Aligned single-wall carbon nanotubes in composites by melt processing methods," *Chemical Physics Letters*, v. 330, pp. 219-225.
- Harris, P. J. F. (1999). *Carbon Nanotubes and Related Structures: New Materials for the 21st Century*. Cambridge, Cambridge University Press.
- Hashin, Z. (1965). "Viscoelastic behavior of heterogeneous media," *Journal of Applied Mechanics*, v. 32, pp. 630-636.
- Hashin, Z. (1970). "Complex moduli of viscoelastic composites: II. Fiber reinforced materials," *International Journal of Solids and Structures*, v. 6, pp. 797-807.
- Hernández, E., C. Goze, P. Bernier and A. Rubio (1998). "Elastic properties of C and B<sub>x</sub>C<sub>y</sub>N<sub>z</sub> composite nanotubes," *Physical Review Letters*, v. 80(20), pp. 4502-4505.
- Huang, J. H. (2001). "Some closed-form solutions for effective moduli of composites containing randomly orientated short fibers," *Materials Science and Engineering A*, v. 315, pp. 11-20.
- Iijima, S. (1991). "Helical microtubules of graphitic carbon," *Nature*, v. 354, pp. 56.
- Jamieson, V. (2000). "Carbon nanotubes roll on," *Physics World*, v. 13(6).

- Jia, Z., Z. Wang, C. Xu, J. Liang, B. Wei, D. Wu and S. Zhu (1999). "Study on poly(methyl methacrylate)/carbon nanotube composites," *Materials Science and Engineering A*, v. 271, pp. 395-400.
- Jin, L., C. Bower and O. Zhou (1998). "Alignment of carbon nanotubes in a polymer matrix by mechanical stretching," *Applied Physics Letters*, v. 73(9), pp. 1197-1199.
- Jin, Z., K. Pramoda, G. Xu and S. Goh (2001). "Dynamic mechanical behavior of melt-processed multi-walled carbon nanotube/poly(methyl methacrylate) composites," *Chemical Physics Letters*, v. 37, pp. 43-47.
- Jin, Z., X. Sun, G. Xu, S. Goh and W. Ji (2000). "Nonlinear optical properties of some polymer/multi-walled carbon nanotube composites," *Chemical Physics Letters*, v. 318, pp. 505-510.
- Journet, C., W. K. Maser, P. Bernier, A. Loiseau, M. L. de la Chapelle, S. Lefrants, P. Deniard, R. Lee and J. E. Fischer (1997). "Large-scale production of single-walled carbon nanotubes by the electric-arc technique," *Nature*, v. 388, pp. 756-758.
- Krishnan, A., E. Dujardin, T. W. Ebbesen, P. N. Yianilos and M. M. J. Treacy (1998). "Young's modulus of single-walled nanotubes," *Physical Review B*, v. 58(20), pp. 14103-14019.
- Kuo, C.-M., K. Takahashi and T.-S. Chou (1988). "Effect of fiber waviness on the nonlinear elastic behavior of flexible composites," *Journal of Composite Materials*, v. 22, pp. 1004-1025.
- Kyotani, T., L. Tsai and A. Tomita (1996). "Preparation of ultrafine carbon tubes in nanochannels of an anodic aluminum oxide film," *Chemistry of Materials*, v. 8, pp. 2109-2113.
- Li, A. P., F. Muller and U. Gosele (2000). "Polycrystalline and monocrystalline pore arrays with large interpore distance in anodic alumina," *Electrochemical and Solid-State Letters*, v. 3(3), pp. 131-134.
- Li, F., M. Cheng, S. Bai, G. Su and M. S. Dresselhaus (2000). "Tensile strength of single-walled carbon nanotubes directly measured from their macroscopic ropes," *Applied Physics Letters*, v. 77(20), pp. 3161-3163.
- Li, J., C. Papadopoulos, J. Xu and M. Moskovits (1999). "Highly-ordered carbon nanotube arrays for electronics applications," *Applied Physics Letters*, v. 75(3), pp. 367-369.
- Li, J. Y. (1999). "On micromechanics approximation for the effective thermoelastic moduli of multi-phase composite materials," *Mechanics of Materials*, v. 31, pp. 149-159.

- Liao, K. and S. Li (2001). "Interfacial characteristics of a carbon nanotube-polystyrene composite system," *Applied Physics Letters*, v. 79(25), pp. 4225-4227.
- Liu, X. and Q. Wu (2002). "Phase transition in nylon 6/clay nanocomposites on annealing," *Polymer*, v. 43, pp. 1933-1936.
- López, M. J., A. Rubio, J. A. Alonso, L.-C. Qin and S. Iijima (2001). "Novel polygonized single-wall carbon nanotube bundles," *Physical Review Letters*, v. 86(14), pp. 3056.
- Lordi, V. and N. Yao (2000). "Molecular mechanics of binding in carbon-nanotube-polymer composites," *Journal of Materials Research*, v. 15(12), pp. 2770-2779.
- Lourie, O., D. M. Cox and H. D. Wagner (1998). "Buckling and collapse of embedded carbon nanotubes," *Physical Review Letters*, v. 81(8), pp. 1638-1641.
- Lourie, O. and H. Wagner (1999). "Evidence of stress transfer and formation of fracture clusters in carbon nanotube-based composites," *Composites Science and Technology*, v. 59, pp. 975-977.
- Lourie, O. and H. D. Wagner (1998a). "Evaluation of Young's modulus of carbon nanotubes by micro-Raman spectroscopy," *Journal of Materials Research*, v. 13(9), pp. 2418-2422.
- Lourie, O. and H. D. Wagner (1998b). "Transmission electron microscopy observations of fracture of single-wall carbon nanotubes under axial tension," *Applied Physics Letters*, v. 73(24), pp. 3527-3529.
- Lozano, K. and E. Barrera (2001). "Nanofiber-reinforced thermoplastic composites. I. Thermoanalytical and mechanical analyses," *Journal of Applied Polymer Science*, v. 79, pp. 125-133.
- Lu, J. P. (1997). "Elastic properties of carbon nanotubes and nanoropes," *Physical Review Letters*, v. 79(7), pp. 1297-1300.
- Mai, K., E. Mader and M. Muhle (1998). "Interphase characterization in composites with new non-destructive methods," *Composites Part A*, v. 29A, pp. 1111-1119.
- Masuda, H., H. Yamada, M. Satoh, H. Asoh, M. Nakao and T. Tamamura (1997). "Highly ordered nanochannel-array architecture in anodic alumina," *Applied Physics Letters*, v. 71(19), pp. 2770-2772.
- Matienzo, L. J., D. W. Wang and F. Emmi (1994). *Polymer Fabrication Techniques. Characterization of Polymers*. N. J. Chou, S. P. Kowalczyk, R. Saraf and H.-M. Tong. Boston, Butterworth-Heinmann.

- McCarthy, B., J. N. Coleman, S. A. Curran, A. B. Dalton, A. P. Davey, Z. Konya, A. Fonseca, J. B. Nagy and W. J. Blau (2000). "Observation of site selective binding in a polymer nanotube composite," *Journal of Materials Science Letters*, v. 19(24), pp. 2239-2241.
- McKenna, G. B., Y. Leterrier and C. R. Schultheisz (1995). "The evolution of material properties during physical aging," *Polymer Engineering and Science*, v. 35(5), pp. 403-410.
- Menard, K. P. (1999). *Dynamic Mechanical Analysis: A Practical Introduction*. Boca Raton, FL, CRC Press.
- Mori, T. and K. Tanaka (1973). "Average stress in matrix and average elastic energy of materials with misfitting inclusions," *Acta Metallurgica*, v. 21, pp. 571-574.
- O'Brien, D. J., P. T. Mather and S. R. White (2001). "Viscoelastic properties of an epoxy resin during cure," *Journal of Composite Materials*, v. 35(10), pp. 883-904.
- Odegard, G., T. Gates, L. Nicholson and K. Wise (2001a). *Equivalent-continuum modeling of nano-structured materials*. NASA, Hampton, VA. TM-2001-210863
- Odegard, G. M., T. S. Gates and K. E. Wise (2001b). "Constitutive modeling of nanotube-reinforced polymer composites". 43rd AIAA/ASME/ASCE/AHS/ASC Structures, Structural Dynamics, and Materials Conference, Denver, CO.
- Pan, Z. W., S. S. Xie, L. Lu, B. H. Chang, L. F. Sun, W. Y. Zhou, G. Wang and D. L. Zhang (1999). "Tensile tests of ropes of very long aligned multiwalled carbon nanotubes," *Applied Physics Letters*, v. 74(21), pp. 3152-3154.
- Poncharal, P., Z. L. Wang, D. Ugarte and W. A. de Heer (1999). "Electrostatic deflections and electromechanical resonances of carbon nanotubes," *Science*, v. 283, pp. 1513-1516.
- Qian, D., E. C. Dickey, R. Andrews and T. Rantell (2000). "Load transfer and deformation mechanisms in carbon nanotube-polystyrene composites," *Applied Physics Letters*, v. 76(20), pp. 2868-2870.
- Qui, Y. P. and G. J. Weng (1991). "The influence of inclusion shape on the overall elastoplastic behavior of a two-phase isotropic composite," *International Journal of Solids and Structures*, v. 27(12), pp. 1537-1550.
- Randle, V. (1992). *Microtexture Determination and its Application*. London, UK, Institute of Materials.
- Ruoff, R. S. (2001). Private communication.

- Ruoff, R. S. and D. C. Lorents (1995). "Mechanical and thermal properties of carbon nanotubes," *Carbon*, v. 33(7), pp. 925-930.
- Salvetat, J.-P., J.-M. Bonard, N. H. Thomson, A. J. Kulik, L. Forró, W. Benoit and L. Zuppiroli (1999). "Mechanical properties of carbon nanotubes," *Applied Physics A*, v. 69, pp. 255-260.
- Salvetat, J.-P., G. Briggs, J.-M. Bonard, R. Basca, A. Kulik, T. Stöckli, N. Burnham and L. Forró (1999). "Elastic and shear moduli of single-walled carbon nanotube ropes," *Physical Review Letters*, v. 82(5), pp. 944-947.
- Salvetat, J.-P., A. J. Kulik, J.-M. Bonard, G. D. A. Briggs, T. Stöckli, K. Métérier, S. Bonnamy, F. Béguin, N. A. Burnham and L. Forró (1999). "Elastic modulus of ordered and disordered multiwalled carbon nanotubes," *Advanced Materials*, v. 11(2), pp. 161-165.
- Sánchez-Portal, S., E. Artacho, J. M. Soler, A. Rubio and P. Ordejón (1999). "*Ab initio* structural, elastic, and vibrational properties of carbon nanotubes," *Physical Review B*, v. 59(19), pp. 12678-12688.
- Sandler, J., M. S. P. Shaffer, T. Prasse, W. Bauhofer, K. Schulte and A. H. Windle (1999). "Development of a dispersion process for carbon nanotubes in an epoxy matrix and the resulting electrical properties," *Polymer*, v. 40(21), pp. 5967-5971.
- Schadler, L. S. (2002). Private communication.
- Schadler, L. S., S. C. Giannaris and P. M. Ajayan (1998). "Load transfer in carbon nanotube epoxy composites," *Applied Physics Letters*, v. 73(26), pp. 3842-3844.
- Schjodt-Thomsen, J. and R. Pyrz (2001). "The Mori-Tanaka stiffness tensor: Diagonal symmetry, complex fibre orientations and non-dilute volume fractions," *Mechanics of Materials*, v. 33, pp. 531-544.
- Shaffer, M. S. P. and A. H. Windle (1999). "Fabrication and characterization of carbon nanotube/poly(vinyl alcohol) composites," *Advanced Materials*, v. 11(11), pp. 937-941.
- Siegel, R., S. Chang, B. Ash, J. Stone, P. Ajayan, R. Doremus and L. Schadler (2001). "Mechanical behavior of polymer and ceramic matrix nanocomposites," *Scripta Materialia*, v. 44, pp. 2061-2064.
- Smith, B. W., Z. Benes, D. E. Luzzi, J. E. Fischer, D. A. Walters, M. J. Casavant, J. Schmidt and R. E. Smalley (2000). "Structural anisotropy of magnetically aligned single wall carbon nanotube films," *Applied Physics Letters*, v. 77(5), pp. 663-665.

- Srivastava, D., D. W. Brenner, J. D. Schall, K. D. Ausman, M.-F. Yu and R. S. Ruoff (1999). "Predictions of enhanced chemistry reactivity at regions of local conformational strain on carbon nanotubes: Kinky chemistry," *Journal of Physical Chemistry B*, v. 103(21), pp. 4330-4337.
- Stéphan, C., T. P. Nguyen, M. L. de la Chapelle, S. Lefrant, C. Journet and P. Bernier (2000). "Characterization of singlewalled carbon nanotubes-PMMA composites," *Synthetic Metals*, v. 108, pp. 139-149.
- Struik, L. C. E. (1978). *Physical Aging in Amorphous Polymers and other Materials*. New York, Elsevier.
- Tandon, G. P. and G. J. Weng (1986). "Average stress in the matrix and effective moduli of randomly orientated composites," *Composites Science and Technology*, v. 27, pp. 111-132.
- Tang, B. Z. and H. Xu (1999). "Preparation, alignment, and optical properties of soluble poly(phenylacetylene)-wrapped carbon nanotubes," *Macromolecules*, v. 32, pp. 2569-2576.
- Thess, A., R. Lee, P. Nikolaev, H. Dia, P. Petit, J. Robert, C. Xu, Y. H. Lee, S. G. Kim, A. G. Rinzler, D. T. Colbert, G. E. Scuseria, D. Tománek, J. E. Fischer and R. E. Smalley (1996). "Crystalline ropes of metallic carbon nanotubes," *Science*, v. 273, pp. 483-487.
- Thomason, J. L. (1995). "The interface region in glass fibre-reinforced epoxy resin composites: 3. Characterization of fibre surface coatings and the interphase," *Composites*, v. 26, pp. 487-498.
- Treacy, M. M. J., T. W. Ebbesen and J. M. Gibson (1996). "Exceptionally high Young's modulus observed for individual carbon nanotubes," *Nature*, v. 381, pp. 678-680.
- Tschogel, N. W. (1989). *The Phenomenological Theory Of Linear Viscoelastic Behavior*. Berlin, Springer-Verlag.
- Vander Wal, R. L. and T. M. Ticich (2001). "Flame and furnace synthesis of single-walled and multi-walled carbon nanotubes and nanofibers," *Journal of Physical Chemistry*, v. 105(42), pp. 10249-10256.
- Wagner, H. D., O. Lourie, Y. Feldman and R. Tenne (1998). "Stress-induced fragmentation of multiwall carbon nanotubes in a polymer matrix," *Applied Physics Letters*, v. 72(2), pp. 188-190.

- Weng, G. J. (1990). "The theoretical connection between Mori-Tanaka's theory and the Hashin-Shtrikman-Wadpole bounds," *International Journal of Engineering Science*, v. 28(11), pp. 1111-1120.
- Wise, K. and J. Hinkley (2001). "Molecular dynamics simulations of nanotube-polymer composites". American Physical Society Spring Meeting, Seattle, WA.
- Wong, E. W., P. E. Sheehan and C. M. Lieber (1997). "Nanobeam mechanics: Elasticity, strength, and toughness of nanorods and nanotubes," *Science*, v. 277, pp. 1971-1975.
- Wood, J. R., Q. Zhao, M. D. Frogley, E. R. Meurs, A. D. Prins, T. Peijs, D. J. Dunstan and H. D. Wagner (2000). "Carbon nanotubes: From molecular to macroscopic sensors," *Physical Review B*, v. 62(11), pp. 7571-7575.
- Wood, J. R., Q. Zhao and H. D. Wagner (2001). "Orientation of carbon nanotubes in polymers and its detection by Raman spectroscopy," *Composites: Part A*, v. 32, pp. 391-399.
- Wu, Q., X. Liu and L. A. Berglund (2002). "FT-IR spectroscopic study of hydrogen bonding in PA6/clay nanocomposites," *Polymer*, v. 43, pp. 2445-2449.
- Xiao, M., L. Sun, J. Liu, Y. Li and K. Gong (2002). "Synthesis and properties of polystyrene/graphite nanocomposites," *Polymer*, v. 43, pp. 2245-2248.
- Xie, S., W. Li, Z. Pan, B. Chang and L. Sun (2000). "Mechanical and physical properties on carbon nanotube," *Journal of Physics and Chemistry of Solids*, v. 61, pp. 1153-1158.
- Xin, Z., Z. Jianjun and O.-Y. Zhong-can (2000). "Strain energy and Young's modulus of single-wall carbon nanotubes calculated from electronic energy-band theory," *Physical Review B*, v. 62(20), pp. 13692.
- Xu, T. (2002a). Private communication.
- Xu, T. (2002b). *Template synthesis of nanomaterials and nanostructures*. PhD proposal, Northwestern University, Evanston, IL.
- Yakobson, B. I., M. P. Campbell, C. J. Brabec and J. Bernholc (1997). "High strain rate fracture and C-chain unraveling in carbon nanotubes," *Computational Materials Science*, v. 8, pp. 341-348.
- Yakobson, B. I. and R. E. Smalley (1997). "Fullerene nanotubes: C<sub>1,000,000</sub> and beyond," *American Scientist*, v. July-August.

- Yin, Y., B. Gates and Y. Xia (2000). "A soft lithography approach to the fabrication of nanostructures of single crystalline silicon with well-defined dimensions and shapes," *Advanced Materials*, v. 12(19), pp. 1426-1430.
- Young, R. J. and P. A. Lovell (1991). *Introduction to Polymers*. London, Chapman & Hall.
- Yu, M.-F., B. S. Files, S. Arepalli and R. S. Ruoff (2000). "Tensile loading of ropes of single wall carbon nanotubes and their mechanical properties," *Physical Review Letters*, v. 84(24), pp. 5552-5555.
- Yu, M.-F., T. Kowalewski and R. S. Ruoff (2000). "Investigation of the radial deformability of individual carbon nanotubes under controlled indentation force," *Physical Review Letters*, v. 85(7), pp. 1456-1459.
- Yu, M.-F., O. Lourie, M. Dyer, K. Moloni, T. F. Kelly and R. S. Ruoff (2000). "Strength and breaking mechanism of multiwalled carbon nanotubes under tensile load," *Science*, v. 287, pp. 637-640.
- Yu, M.-F., B. I. Yakobson and R. S. Ruoff (2000). "Controlled sliding and pullout of nested shells in individual multiwalled carbon nanotubes," *Journal of Physical Chemistry B*, v. 104, pp. 8764-8767.
- Zhao, Q., J. R. Wood and H. D. Wagner (2001). "Stress fields around defects and fibers in a polymer using carbon nanotubes as sensors," *Applied Physics Letters*, v. 78, pp. 1748.
- Zhao, Y. H. and G. J. Weng (1990). "Effective elastic moduli of ribbon-reinforced composites," *Journal of Applied Mechanics*, v. 57, pp. 158-167.
- Zhao, Y. H. and G. J. Weng (1996). "Influence of random bridging on the elastic and elastoplastic properties of fiber reinforced composites," *Acta Mechanica*, v. 116, pp. 29-44.

## APPENDIX

### Summary of the nanotube-reinforced polymer literature

**Key: AD = arc discharge, LV = laser vaporization,  
CVD = chemical vapor deposition, NA = not applicable**

Paper	Polymer	NT	Notes
(Ajayan, Stephan et al. 1994)	Epoxy	AD MWNTs	Shear-induced alignment of NTs
(Ajayan, Schadler et al. 2000)	Epoxy	SWNT bundles	Curving and stretching of the NTs on loading; at fracture see pulling apart of the bundles, not NT fracture
(Andrews, Jacques et al. 2002)	Polystyrene	MWNTs (0-25% wt)	Significant increases in effective elastic modulus
(Bower, Rosen et al. 1999)	Thermoplastic (polyhydroxy-aminoether)	MWNTs	Alignment via mechanical stretching above $T_g$
(Bradshaw, Fisher et al. 2002)	NA	NA	Numerical computation of the dilute strain concentration tensor to account for NT waviness
(Chen, Shaffer et al. 2000)	Polypyrrole (PPy)	AD NTs	Mainly interested in electrical properties; some impedance spectroscopy data
(Cochet, Maser et al. 2001)	Conducting polymer polyaniline (PANI)	AD SWNTs (10, 20, 30, 40, 50% wt)	"In-situ" polymerization; Raman measurements suggest effective site-selective interactions between the PANI and the MWNTs facilitating charge-transfer processes

(Cooper, Young et al. 2001)	Epoxy (Araldite LY5052)	LV SWNTs; AD SWNTs, MWNTs (1% wt)	Looked at differences in the Raman responses of the NTs; interested in the use of NTs as strain sensors
(Curran, Ajayan et al. 1998)	PmPV	AD MWNTs	Polymer chains "wrap" helically about the NTs; TEM evidence of good adhesion
(Fan, Wan et al. 1999)	Polypyrrole (PPY)	CVD NTs	The CNTs function as a template for PPY polymerization.
(Fisher, Bradshaw et al. 2002a)	NA	NA	Model to incorporate nanotube waviness into micromechanical predictions of NRP effective modulus.
(Fisher, Bradshaw et al. 2002b)	NA	NA	Micromechanics predictions of NRP effective stiffness are much greater than experimental results
(Gong, Liu et al. 2000)	Epoxy	AD MWNTs	Shift in $T_g$ attributed to the role of the surfactant.
(Grimes, Mungle et al. 2000)	PEMA	AD SWNT bundles (0-23% wt)	Effective electrical properties
(Hadjiev, Iliev et al. 2001)	Epoxy (Epon 862/EPI-CURE W)	LV SWNTs (1% wt)	Raman data suggests direct coupling of NT to epoxy; load is transferred predominantly along the nanorope axis
(Haggenmueller, Gommans et al. 2000)	PMMA	SWNTs	Alignment via combination of solvent casting and melt processing of the NRP.
(Jia, Wang et al. 1999)	PMMA	NTs	CNTs participate in PMMA polymerization; effective properties decrease for greater than 7 wt% NTs due to residual stresses in the matrix
(Jin, Bower et al. 1998)	PHAE (thermoplastic)	AD MWNTs	NT alignment via mechanical stretching above $T_g$ ; loading to 500% strain without fracture

(Jin, Sun et al. 2000)	PEG, P2VP, P4VP, PVPh; PEO	AD MWNTs	Interested in nonlinear optical effects; create "polymer-coated" and "polymer-grafted" MWNTs
(Jin, Pramoda et al. 2001)	PMMA using a melt-blending process	AD MWNTs	Large increases in storage modulus at high temperature; suggest increases are due to the amorphous nature of the polymer matrix
(Liao and Li 2001)	Polystyrene	NTs	Molecular mechanics model of the interface; estimated the interfacial shear stress to be 160 MPa
(Lordi and Yao 2000)	PmPV, PMMA, PPA	(10,10) SWNTs	MD work suggesting that the helical nature of PmPV allows it to closely interact with the NTs.
(Lourie, Cox et al. 1998)	Epoxy (Araldite LY564, Ciba-Geigy)	AD MWNTs	Interested in the buckling and collapse of NTs in microtomed TEM samples
(Lourie and Wagner 1998a)	Epoxy	SWNT; AD MWNTs; carbon fiber	Raman analysis of the compressive stresses caused by polymer shrinkage upon cure
(Lourie and Wagner 1998b)	Epoxy	SWNT bundles	Aligned SWNT bundles bridging cracks/holes in the polymer
(Lourie and Wagner 1999)	Epoxy (Araldite LY564, Ciba-Geigy)	AD MWNTs	Formation of damage doublets in adjacent CNTs, comparable to those in fiber reinforced composites; due to redistribution of stress from a failed fiber to its unfailed neighbors
(Lozano and Barrera 2001)	Polypropylene	Pyrograf nanofibers, 100 nm ave. diameter	Nanofibers raised working temperature 100 °C and dynamic modulus increased 350%, but no change in strength
(McCarthy, Coleman et al. 2000)	ImPV, a PPV derivative	AD and CVD NTs	Crystalline polymer nucleates from NT defects; show that the polymer coats the NT as a periodic, ordered structure.
(Odegard, Gates et al. 2001a)	LaRC-SI polyimide with PmPV interface	SWNTs	Equivalent continuum model of NT and interphase as an effective fiber for micromechanics predictions

(Qian, Dickey et al. 2000)	Polystyrene (PS)	MWNTs (1% wt)	~ 35% increase in modulus and ~ 25% in ultimate stress
(Sandler, Shaffer et al. 1999)	Epoxy	CVD MWNTs	Antistatic applications; large increases in electrical conductivity for low volume fractions of NTs
(Schadler, Giannaris et al. 1998)	Epoxy (Shell Epon 828)	MWNTs (5% wt)	Results suggest that only the outer layer of the MWNT is loaded in tension, whereas all tubes loaded in compression
(Shaffer and Windle 1999)	Poly(vinyl alcohol) (PVOH)	CVD MWNTs (0-60 wt%)	Minimal enhancement below $T_g$ , significant increase in mechanical properties above $T_g$
(Stéphan, Nguyen et al. 2000)	PMMA (spin-coating)	AD SWNTs	Polymer intercalation between NTs within a bundle
(Tang and Xu 1999)	poly(phenylacetylene) (PPA)	MWNTs	NTs helically wrapped by the PPA chains; NTs protect PPA from photodegradation under harsh laser irradiation.
(Wagner, Lourie et al. 1998)	Urethane/diacrylate oligomer (EBERCRYL 4858)	AD MWNTs	MWNT-polymer stress transfer efficiency estimated to be an order of magnitude larger than in conventional fiber-based composites
(Wood, Zhao et al. 2000)	Urethane/diacrylate oligomer (EBERCRYL 4858)	SWNTs (0.1% wt)	Use of NTs as sensitive nanoscale strain gauges, where 0.1 wt% NT causes the polymer to become Raman active
(Wood, Zhao et al. 2001)	Urethane/diacrylate oligomer (EBERCRYL 4858)	SWNTs (flow orientated)	Difference between mechanical and spectroscopic data at high strain caused by the interface yielding in shear, halting stress transfer to the NTs
(Zhao, Wood et al. 2001)	Urethane/diacrylate oligomer (EBERCRYL 4858)	SWNTs (0.1% wt)	Interested in the use of NTs as strain sensors

## Tensor representation using contracted notation

For a linear elastic material, the state of stress at a point can be represented by stress components  $\sigma_{ij}$ , which are related to strain components  $\epsilon_{ij}$  via

$$\sigma_{ij} = C_{ijkl} \epsilon_{kl}, \quad (74)$$

$$\epsilon_{ij} = S_{ijkl} \sigma_{kl} \quad (75)$$

where  $(i, j, k, l = 1, 2, 3)$  and  $C_{ijkl}$  and  $S_{ijkl}$  are referred to as the stiffness and compliance tensors, respectively. Repeated indices imply summation over those indices.

It is standard practice in the micromechanics and composites community to utilize contracted (alternatively called Voigt or two-index) notation in order to simplify notation. In general such notation involves the following replacement scheme to simplify tensor indices

$$\begin{aligned} 11 &\rightarrow 1, & 22 &\rightarrow 2, & 33 &\rightarrow 3 \\ 23 &\rightarrow 4, & 31 &\rightarrow 5, & 12 &\rightarrow 6 \end{aligned} \quad (76)$$

Using this replacement scheme, the components of the stress, strain, and stiffness tensors can be written as

$$\begin{aligned}
\sigma_{11} &= \sigma_1, & \sigma_{22} &= \sigma_2, & \sigma_{33} &= \sigma_3, \\
\sigma_{23} &= \sigma_{32} = \sigma_4 = \sigma_4, & & & & \\
\sigma_{13} &= \sigma_{31} = \sigma_5 = \sigma_5, & & & & \\
\sigma_{12} &= \sigma_{21} = \sigma_6 = \sigma_6. & & & & 
\end{aligned} \tag{77}$$

$$\begin{aligned}
\sigma_{11} &= \sigma_1, & \sigma_{22} &= \sigma_2, & \sigma_{33} &= \sigma_3, \\
2\sigma_{23} &= \sigma_{23} = \sigma_4 = \sigma_4, & & & & \\
2\sigma_{13} &= \sigma_{13} = \sigma_5 = \sigma_5, & & & & \\
2\sigma_{12} &= \sigma_{12} = \sigma_6 = \sigma_6. & & & & 
\end{aligned} \tag{78}$$

$$\begin{aligned}
C_{1111} &= C_{11}, & C_{1122} &= C_{12}, & C_{1133} &= C_{13}, & C_{1123} &= 2C_{14}, & C_{1131} &= 2C_{15}, & C_{1112} &= 2C_{16}, \\
C_{2211} &= C_{21}, & C_{2222} &= C_{22}, & C_{2233} &= C_{23}, & C_{2223} &= 2C_{24}, & C_{2231} &= 2C_{25}, & C_{2212} &= 2C_{26}, \\
C_{3311} &= C_{31}, & C_{3322} &= C_{32}, & C_{3333} &= C_{33}, & C_{3323} &= 2C_{34}, & C_{3331} &= 2C_{35}, & C_{3312} &= 2C_{36}, \\
C_{2311} &= C_{41}, & C_{2322} &= C_{42}, & C_{2333} &= C_{43}, & C_{2323} &= 2C_{44}, & C_{2331} &= 2C_{45}, & C_{2312} &= 2C_{46}, \\
C_{3111} &= C_{51}, & C_{3122} &= C_{52}, & C_{3133} &= C_{53}, & C_{3123} &= 2C_{54}, & C_{3131} &= 2C_{55}, & C_{3112} &= 2C_{56}, \\
C_{1211} &= C_{61}, & C_{1222} &= C_{62}, & C_{1233} &= C_{63}, & C_{1223} &= 2C_{64}, & C_{1231} &= 2C_{65}, & C_{1212} &= 2C_{66}.
\end{aligned} \tag{79}$$

Such substitution permits the constitutive equations describing the stress-strain response of the material to be written in contracted notation as

$$\sigma_i = C_{ij} \epsilon_j, \quad \epsilon_i = S_{ij} \sigma_j, \tag{80}$$

where  $(i,j = 1,2,..6)$  and due to energy considerations,  $C_{ij} = C_{ji}$  and  $S_{ij} = S_{ji}$ .

In general there are 36 independent constants  $C_{ij}$  (and likewise  $S_{ij}$ ) necessary to describe the stress-strain response of an elastic material. However, for special classes of materials the number of elastic constants is reduced due to special symmetry

conditions. Two common cases of material symmetry that are used throughout this work are transversely isotropic and isotropic symmetry. For a material that is transversely isotropic with a 2-3 plane of isotropy, the contracted stiffness tensor is of the following form

$$\begin{matrix}
 \begin{matrix} \square \\ \square \\ \square \\ \square \\ \square \\ \square \end{matrix} & \begin{matrix} 1 \\ 2 \\ 3 \\ 4 \\ 5 \\ 6 \end{matrix} & \begin{matrix} \square \\ \square \\ \square \\ \square \\ \square \\ \square \end{matrix} & \begin{matrix} C_{11} \\ C_{12} \\ C_{12} \\ 0 \\ 0 \\ 0 \end{matrix} & \begin{matrix} C_{12} \\ C_{22} \\ C_{23} \\ 0 \\ 0 \\ 0 \end{matrix} & \begin{matrix} C_{12} \\ C_{23} \\ C_{22} \\ 0 \\ 0 \\ 0 \end{matrix} & \begin{matrix} 0 \\ 0 \\ 0 \\ \frac{C_{22} - C_{23}}{2} \\ 0 \\ 0 \end{matrix} & \begin{matrix} 0 \\ 0 \\ 0 \\ 0 \\ C_{55} \\ 0 \end{matrix} & \begin{matrix} 0 \\ 0 \\ 0 \\ 0 \\ 0 \\ C_{55} \end{matrix} & \begin{matrix} \square \\ \square \\ \square \\ \square \\ \square \\ \square \end{matrix} & \begin{matrix} 1 \\ 2 \\ 3 \\ 4 \\ 5 \\ 6 \end{matrix} & \begin{matrix} \square \\ \square \\ \square \\ \square \\ \square \\ \square \end{matrix}
 \end{matrix} \tag{81}$$

For an isotropic material the constitutive equation is further simplified such that

$$\begin{matrix}
 \begin{matrix} \square \\ \square \\ \square \\ \square \\ \square \\ \square \end{matrix} & \begin{matrix} 1 \\ 2 \\ 3 \\ 4 \\ 5 \\ 6 \end{matrix} & \begin{matrix} \square \\ \square \\ \square \\ \square \\ \square \\ \square \end{matrix} & \begin{matrix} C_{11} \\ C_{12} \\ C_{12} \\ 0 \\ 0 \\ 0 \end{matrix} & \begin{matrix} C_{12} \\ C_{11} \\ C_{12} \\ 0 \\ 0 \\ 0 \end{matrix} & \begin{matrix} C_{12} \\ C_{12} \\ C_{11} \\ 0 \\ 0 \\ 0 \end{matrix} & \begin{matrix} 0 \\ 0 \\ 0 \\ \frac{C_{11} - C_{12}}{2} \\ 0 \\ 0 \end{matrix} & \begin{matrix} 0 \\ 0 \\ 0 \\ 0 \\ \frac{C_{11} - C_{12}}{2} \\ 0 \end{matrix} & \begin{matrix} 0 \\ 0 \\ 0 \\ 0 \\ 0 \\ \frac{C_{11} - C_{12}}{2} \end{matrix} & \begin{matrix} \square \\ \square \\ \square \\ \square \\ \square \\ \square \end{matrix} & \begin{matrix} 1 \\ 2 \\ 3 \\ 4 \\ 5 \\ 6 \end{matrix} & \begin{matrix} \square \\ \square \\ \square \\ \square \\ \square \\ \square \end{matrix}
 \end{matrix} \tag{82}$$

While contracted notation can be a useful tool in that it significantly simplifies the bookkeeping required for the tensor manipulation, care must be taken to ensure that the tensor contraction is maintained in a consistent manner throughout the

analysis. For example, for the contraction of the Eshelby tensor it is necessary to include a factor of two for the shear strain components to maintain the appropriate tensorial relationship (as demonstrated later in this Appendix). Consistent use of tensorial shear strain  $\epsilon_{ij}$  and engineering shear strain  $\gamma_{ij}$  (where  $\gamma_{ij} = \frac{1}{2}\epsilon_{ij}$ ) throughout the analysis is critical.

### **Components of the Eshelby $S_{ijkl}$ tensor along the $x_3$ axis**

For an ellipsoidal inclusion aligned along the 3-axis with aspect ratio  $\alpha = \frac{L}{d}$ , the components of the Eshelby tensor are given as (Tandon and Weng 1986)

$$\begin{aligned}
S_{1111} = S_{2222} &= \frac{3}{8(1-\nu_0)} \frac{\nu^2}{\nu^2-1} + \frac{1}{4(1-\nu_0)} \frac{\nu}{\nu^2-1} \frac{9}{4(\nu^2-1)} g \\
S_{3333} &= \frac{1}{2(1-\nu_0)} \frac{\nu}{\nu^2-1} + \frac{3\nu^2-1}{\nu^2-1} \frac{\nu}{\nu^2-1} + \frac{3\nu^2}{\nu^2-1} \frac{g}{\nu^2-1} \\
S_{1122} = S_{2211} &= \frac{1}{4(1-\nu_0)} \frac{\nu^2}{2(\nu^2-1)} + \frac{\nu}{\nu^2-1} \frac{\nu}{\nu^2-1} + \frac{3}{4(\nu^2-1)} \frac{g}{\nu^2-1} \\
S_{1133} = S_{2233} &= \frac{1}{2(1-\nu_0)} \frac{\nu^2}{\nu^2-1} + \frac{1}{4(1-\nu_0)} \frac{3\nu^2}{\nu^2-1} \frac{g}{\nu^2-1} \quad (83) \\
S_{3311} = S_{3322} &= \frac{1}{2(1-\nu_0)} \frac{\nu}{\nu^2-1} + \frac{1}{\nu^2-1} + \frac{1}{2(1-\nu_0)} \frac{\nu}{\nu^2-1} + \frac{3}{2(\nu^2-1)} \frac{g}{\nu^2-1} \\
S_{1212} = S_{2121} &= \frac{1}{4(1-\nu_0)} \frac{\nu^2}{2(\nu^2-1)} \frac{\nu}{\nu^2-1} + \frac{3}{4(\nu^2-1)} \frac{g}{\nu^2-1} \\
S_{3131} = S_{3232} &= \frac{1}{4(1-\nu_0)} \frac{\nu}{\nu^2-1} \frac{\nu^2+1}{\nu^2-1} + \frac{1}{2} \frac{\nu}{\nu^2-1} \frac{3(\nu^2+1)}{\nu^2-1} \frac{g}{\nu^2-1}
\end{aligned}$$

where  $\nu_0$  is the Poisson ratio of the matrix, and

$$\begin{aligned}
g &= \frac{\nu}{(\nu^2-1)^{3/2}} \frac{\nu}{\nu^2-1} (\nu^2-1)^{1/2} \cosh^{-1} \frac{\nu}{\nu^2-1} \\
&= \frac{\nu}{(1-\nu^2)^{3/2}} \frac{\nu}{\nu^2-1} \cos^{-1} \frac{\nu}{\nu^2-1} (1-\nu^2)^{1/2}
\end{aligned} \quad (84)$$

for prolate and oblate shapes inclusion cross-sections, respectively. All other components of the Eshelby tensor are zero.

For an ellipsoidal inclusion with an infinite aspect ratio ( $l/d \rightarrow \infty$ ) parallel to the 3-axis, the components of the Eshelby tensor simplify to:

$$\begin{aligned}
 S_{3333} &= S_{3311} = S_{3322} = 0 \\
 S_{1111} &= S_{2222} = \frac{5\nu_0 + 4\nu_0}{8(1 - \nu_0)} \\
 S_{1122} &= S_{2211} = \frac{4\nu_0 - 1}{8(1 - \nu_0)} \\
 S_{1133} &= S_{2233} = \frac{\nu_0}{2(1 - \nu_0)}
 \end{aligned} \tag{85}$$

$$S_{1212} = \frac{3\nu_0 + 4\nu_0}{8(1 - \nu_0)}$$

$$S_{3131} = S_{3232} = \frac{1}{4}.$$

For spheroidal inclusions the Eshelby components further simplify to:

$$S_{1111} = S_{2222} = S_{3333} = \frac{7\nu_0 + 5\nu_0}{15(1 - \nu_0)}$$

$$S_{1122} = S_{2233} = S_{3311} = \frac{5\nu_0 - 1}{15(1 - \nu_0)} \tag{86}$$

$$S_{1212} = S_{2323} = S_{3131} = \frac{4\nu_0 + 5\nu_0}{15(1 - \nu_0)}.$$

The different Eshelby components presented above are those of a fourth-order tensor that by definition relate the (stress-free) transformation strain to the perturbed strain in an inclusion via

$$\epsilon_{ij}^{pt} = S_{ijkl} \epsilon_{kl}^*, \quad (87)$$

where the perturbed strain  $\epsilon_{ij}^{pt}$  represents the difference between the far-field applied strain  $\epsilon_{ij}^0$  and the average strain in the inclusion  $\epsilon_{ij}^r$  via  $\epsilon_{ij}^{pt} = \epsilon_{ij}^r - \epsilon_{ij}^0$ .

It is customary in micromechanics, and the composites field in general, to take advantage of contracted (or two-index) notation to simplify the bookkeeping of the tensor indices. However, specific care must be taken when contracting the Eshelby tensor for such analyzes. The difficulty arises in contracting those terms of the Eshelby tensor relating the shear components of the perturbed and transformation strains, and is best described via an example. Writing out (87) for the case of  $\epsilon_{23}^{pt}$ ,

$$\begin{aligned} \epsilon_{23}^{pt} = & S_{2311} \epsilon_{11}^* + S_{2312} \epsilon_{12}^* + S_{2313} \epsilon_{13}^* \\ & + S_{2321} \epsilon_{21}^* + S_{2322} \epsilon_{22}^* + S_{2323} \epsilon_{23}^*, \\ & + S_{2331} \epsilon_{31}^* + S_{2332} \epsilon_{32}^* + S_{2333} \epsilon_{33}^* \end{aligned} \quad (88)$$

which for a general ellipsoidal inclusion simplifies to the following non-zero components of the Eshelby tensor

$$\square_{23}^{\text{pt}} = S_{2323}\square_{23}^* + S_{2332}\square_{32}^* = 2S_{2323}\square_{23}^*, \quad (89)$$

where  $\square_{23}^* = \square_{32}^*$  and  $S_{2323} = S_{2332}$ . This can be represented using contracted notation as

$$\square_4^{\text{pt}} = S_{44}\square_4^*. \quad (90)$$

where  $S_{44}=2S_{2323}$ . Thus the complete representation of the Eshelby tensor in contracted notation is:

$$\begin{aligned} S_{11} &= S_{1111}, & S_{22} &= S_{2222}, & S_{33} &= S_{3333}, \\ S_{12} &= S_{1122}, & S_{13} &= S_{1133}, & S_{23} &= S_{2233}, \\ S_{21} &= S_{2211}, & S_{31} &= S_{3311}, & S_{32} &= S_{3322}, \\ S_{44} &= 2S_{2323}, & S_{55} &= 2S_{1313}, & S_{66} &= 2S_{1212}. \end{aligned} \quad (91)$$

### Inter-relations between elastic constants

Input Constants	Output Constants				
	E =	$\nu$ =	G =	K =	$\lambda$ =
E, $\nu$	-	-	$\frac{E}{2(1+\nu)}$	$\frac{E}{3(1-2\nu)}$	$\frac{E\nu}{(1+\nu)(1-2\nu)}$
E, G	-	$\frac{E-2G}{2G}$	-	$\frac{EG}{3(3G-E)}$	$\frac{G(E-2G)}{3G-E}$
E, K	-	$\frac{3K-E}{6K}$	$\frac{3KE}{9K-E}$	-	$\frac{3K(3K-E)}{9K-E}$
E, $\lambda$	-	$\frac{2\nu}{E+\nu+R}$	$\frac{E-3\nu+R}{4}$	$\frac{E+3\nu+R}{6}$	-
$\nu$ , K	$3K(1-2\nu)$	-	$\frac{3K(1-2\nu)}{2(1+\nu)}$	-	$\frac{3K\nu}{1+\nu}$
$\nu$ , $\lambda$	$\frac{\nu(1+\nu)(1-2\nu)}{\nu}$	-	$\frac{\nu(1-2\nu)}{2\nu}$	$\frac{\nu(1+\nu)}{3\nu}$	-
$\nu$ , G	$2G(1+\nu)$	-	-	$\frac{2G(1+\nu)}{3(1-2\nu)}$	$\frac{2G\nu}{1-2\nu}$
G, K	$\frac{9KG}{3K+G}$	$\frac{3K-2G}{6K+2G}$	-	-	$\frac{3K-2G}{3K}$
G, $\lambda$	$\frac{G(3\nu+2G)}{\nu+G}$	$\frac{\nu}{2(\nu+G)}$	-	$\frac{3\nu+2G}{3}$	-
K, $\lambda$	$\frac{9K(K-\nu)}{3K-\nu}$	$\frac{\nu}{3K-\nu}$	$\frac{3}{2}(K-\nu)$	-	-

Table 11. Inter-relations among the elastic constants.  $R = \sqrt{E^2 + 9\nu^2 + 2E\nu}$

## VITA

Frank Thomas Fisher was born in Abington, PA on February 8, 1972, to Frank and Betsy Fisher, and grew up with younger brothers Mike and Sean in the nearby Philadelphia suburb of Warminster, PA. After graduating from Archbishop Wood High School for Boys (Warminster, PA) in 1990, he attended the University of Pittsburgh (Pittsburgh, PA) where he graduated with undergraduate degrees in Mechanical Engineering (Magna Cum Laude) and Applied Mathematics (Summa Cum Laude) in 1995.

After graduation Frank enrolled in the doctoral program in Mechanical Engineering at Northwestern University in Evanston, IL. He soon joined the research group of Professor Cate Brinson and began studying the viscoelastic behavior of polymer matrix composites, with a focus on viscoelasticity and related phenomena. In 1998 he received an MS degree in Mechanical Engineering for his work studying the influence of a viscoelastic interphase on the physical aging of a three-phase composite (“Viscoelastic Behavior of Polymer Matrix Composites with Interphase Effects: Theoretical Models and Finite Element Analysis”).

Long interested in education and with the full support of Professor Brinson, Frank temporarily suspended his PhD studies in September 1999 and enrolled in the Learning Sciences program in the School of Education and Social Policy at

Northwestern. Here he worked with Dr. Penelope Peterson as part of the NSF-funded VaNTH Engineering Research Center for Bioengineering Educational Technologies through the Biomedical Engineering Department at Northwestern. His research focused on the theory of adaptive expertise, the concept that in addition to concept knowledge successful experts display additional cognitive dispositions that facilitate the use of their expertise. Frank adapted this idea for the learning and practice of engineering, developing measures to evaluate and study adaptiveness in undergraduate engineering students. He received an MA degree in Learning Sciences in December 2000.

Frank returned to complete his PhD in Mechanical Engineering in September 2000, beginning work on a new NASA-funded project modeling the mechanical properties of carbon nanotube-reinforced composites. After graduation Frank will continue his research at Northwestern as a post-doctoral fellow in the Department of Mechanical Engineering, before starting a career in academia, where he can continue to pursue his interests in Mechanical Engineering and Engineering Education.

Frank Fisher is co-author of the following publications:

F. T. Fisher, L. C. Brinson, A. Eitan, and L. S. Schadler (2002). Reduced polymer chain mobility in low volume fraction carbon nanotube-reinforced polycarbonate: Spectral response and effective viscoelastic properties. Manuscript in preparation.

R. D. Bradshaw, F. T. Fisher, L. C. Brinson (2002). Fiber waviness in nanotube-reinforced polymer composites: II. Modeling via numerical approximation of the dilute strain concentration tensor, to appear in *Composites Science and Technology*.

Fisher, F. T., R. D. Bradshaw, L. C. Brinson (2002). Fiber waviness in nanotube-reinforced polymer composites: I. Modulus predictions using effective nanotube properties, to appear in *Composites Science and Technology*.

Fisher, F. T., R. D. Bradshaw, L. C. Brinson (2002). Effects of nanotube waviness on the modulus of nanotube-reinforced polymers. *Applied Physics Letters*, 80(24): 4647-4649.

F.T. Fisher and L.C. Brinson (2002). Viscoelasticity and physical aging of carbon nanotube-reinforced polymers. Proceedings for the 2002 Society for Experimental Mechanics Annual Conference, June 10-12, Milwaukee, WI.

Fisher, FT, and PL Peterson (2001). A tool to measure adaptive expertise in biomedical engineering students. Proceedings for the 2001 ASEE Annual Conference, June 24-27, Albuquerque, NM.

Fisher, FT and LC Brinson (2001). Viscoelastic interphases in polymer matrix composites: Theoretical models and finite element analysis. *Composites Science and Technology*, 61: 731-748.